A Generalized Multigroup Cross Section Generation Procedure for High-fidelity Reactor Simulation of Advanced Reactor Designs

by

Byoung-kyu Jeon

A dissertation submitted in partial fulfillment
of the requirements for the degree of
Doctor of Philosophy
(Nuclear Engineering and Radiological Sciences)
in the University of Michigan
2021

Doctoral Committee:

Professor Won Sik Yang, Chair
Professor Michael Atzmon
Professor Thomas J. Downar
Assistant Professor Brendan Matthew Kochunas
Principal Nuclear Engineer Chang-ho Lee, Argonne National Laboratory

Byoung-kyu Jeon

bkjeon@umich.edu

ORCID ID: 0000-0001-5756-9669

Acknowledgements

I would first like to express my deep and sincere gratitude to my advisor Professor Won Sik Yang for giving me the opportunity to do research and his support. I am grateful for his patient and professional guidance that helped me in my research. The encouragement he provided during our weekly discussions helped me surmount challenges that I faced not only in research, but also in life. I look forward to maintaining our relationship with him as my mentor as I start the next chapter in my life.

I would also like to express my gratitude to Dr. Thomas Downar and Dr. Brendan Kochunas, who instilled in me the principles of research project and collaboration as well as a practical perspective on the code development. I feel fortunate to work with Dr. Changho Lee, Dr. Kang Seog Kim, Dr. Yeon Sang Jung and Dr. Hansol Park who gave me irreplaceable experiences and in-depth knowledge that I cannot hardly obtain without their supports. I am extending my thanks to my former and current peers in the NRDSL group of University of Michigan including Connor, Tian, Faisal, Jake, Albert, Gang, Puran, Robby and Mustafa.

I am incredibly grateful to my parents for their love, and I am very much thankful to my wife Sunkyung for her support, understanding and love to complete this thesis.

Table of Contents

List of Tables

List of Figures

Abstract

Motivated by the increased importance of high-fidelity modeling capabilities that can improve the economics and safety of reactor designs, there are active movements to extend the applicability of high-fidelity neutronics codes to advanced reactors. The advanced reactor designs being developed by the industry are significantly diverse in fuel types, geometrical configurations, and neutron spectra. Many designs adopt particulate fuels and increasingly heterogeneous assembly and core geometries. Thermal, epi-thermal, and fast spectrum reactors are considered. This requires significant modifications and improvements in the current multigroup cross section generation methods and procedures, which are developed based on various assumptions and approximations tailored to a specific reactor type of interest. This necessitates it to develop a new generalized multigroup cross section generation procedure for more heterogeneous configurations and a wide range of spectrum.

In this dissertation work, a generalized multigroup cross section generation method is developed for high-fidelity simulation of advanced reactors. In this method, important reactor characteristics over the entire energy range of fission reactors are properly modelled through the following approaches: (1) explicit modeling of resonance and anisotropic scattering of all isotopes by employing the detailed slowing down calculation, (2) proper consideration of spatial self-shielding for all regions, (3) development of an efficient lattice transport calculation method through a generalized condensation scheme, (4) preparation of problem-dependent cross section libraries with respect to background cross section and material temperatures, (5) development of

a double heterogeneity treatment capability for particulate fuel modeling, and (6) generation of accurate gamma cross section library for coupled neutron and gamma heating calculations. The new multigroup cross section generation procedure in this work successfully yields substantially improved results for eigenvalue, reaction rates and heat generation rate for various benchmark problems regardless of reactor energy spectrum. This indicates that the developed procedure can improve the accuracy of high-fidelity neutronic calculations for advanced reactor analysis.

Chapter 1 Introduction

Motivated by the increased importance of high-fidelity modeling capabilities that can improve the economics and safety of reactor designs, there are active movements to extend the applicability of high-fidelity neutronics codes to advanced Gen III+ and Gen-IV reactors, such as next generation light water reactor (LWR) and boiling water reactor (BWR), high temperature gas-cooled reactor (HTGR), very high temperature reactor (VHTR) and fast reactors. The current advanced reactor designs considered by the industry are significantly diverse in fuel types, geometrical configurations, and neutron spectra. Many designs adopt particulate fuels, and the core geometry is generally irregular. Thermal, epi-thermal, and fast spectrum reactors are considered. Most nuclear reactor analyses are performed based on the conventional two- or multi-step procedure in which assembly homogenized broad group (<100 groups, BG) cross sections (XSs) are generated at the first step with the detailed modeling of geometry and slowing down behavior and low order whole core calculations are performed at the second step. The two-step procedure has inherent limitations in accuracy because neutron flux spectra and spatial distribution obtained in the first step could be different from the actual neutron distribution in the core. In addition, inter-assembly spectral transition effect cannot be well captured as the complexity of core geometry increases. As a result, it is not practical to develop the conventional two-step XS generation methods based on homogenization for advanced reactors. For this reason, there have been two major approaches in XS generation methods for the high-fidelity neutronic simulation: continuous energy (CE) Monte Carlo (MC) method and multi group (MG) deterministic method. MC method is often treated as a reference solution because it simulates the behavior of neutrons with

minimized assumptions in treatment of the neutron slowing down, core geometry and spectral coupling. Although the MC based XS generation becomes more practical in a few group XS generation for LWR application as the computing power increases, the inherent stochastic nature of the method, however, limits the applicability of MC based procedure for a wide range of problem. For example, the recent study [1] reveals that the inaccuracy of higher-order scattering moments tally using a MC code introduces a non-negligible bias up to 600 pcm in fast reactor analysis. Due to the large uncertainty of higher moment flux tally in the current MC method, the scalar flux-weighted higher-order scattering moments are inevitable error sources in neutronic analysis.

This necessitates developing a deterministic MG XS library generation procedure of high-fidelity neutronic code for heterogeneous configurations and a wide range of spectrum. Since high-fidelity transport simulations require significant computational time and resources although it is accurate and flexible, the MG XS library was developed to find the best tradeoffs between accuracy and speed. The assumptions and approximations made for specific applications greatly improve the time-to-solution, while it loses their predictive capability outside of its intended scope. Therefore, it is desirable to eliminate or minimize those assumptions and approximations without losing noticeable computational efficiency of the current MG XS generation method. In this introduction chapter, the background theories of the MG XS generation are introduced first, as well as the current limitations of resonance treatment focusing on the fast and thermal spectrum reactor. Then, the research objective and the outline of the dissertation are discussed.

1.1 Multi-group Neutron Transport Theory and Approximations

The steady-state MG neutron transport equation can be written in standard notation as below:

$$\Omega \cdot \nabla \psi_g(r,\Omega) + \sum_i N_i(r)\sigma_{tg}^i(r,\Omega)\psi_g(r,\Omega) = S_{sg}(r,\Omega) + \frac{1}{4\pi} S_{fg}(r) \tag{1.1}$$

where $\psi_g(r,\Omega)$ describes the angular flux of neutrons integrated over energy group g moving in the direction Ω at the position r. N_i and σ_{tg}^i are the number density and microscopic total XS of nuclide i, respectively. S_{sg} and S_{fg} are the scattering and fission neutron given by

$$S_{sg}(r,\Omega) = \sum_i N_i(r) \sum_{l=0}^{L} \sum_{k=-l}^{l} Y_{lk}(\Omega) \sum_{g'} \sigma_{slkgg'}^i(r)\psi_{lkg'}(r) \tag{1.2}$$

$$S_{fg}(r) = \frac{1}{\lambda} \sum_i N_i(r) \sum_{g'} \chi_{gg'}^i \nu\sigma_{fg'}^i(r)\psi_{0g'}(r) \tag{1.3}$$

Here, Y_{lk} is the spherical harmonics, ψ_{lk} is the angular flux moments, $\sigma_{slkgg'}^i$ is the scattering kernel in the form of l-th order Legendre polynomial expansion, σ_{fg}^i is microscopic fission XS, and $\chi_{gg'}^i$ is the fission spectrum from group g' to g. Scalar flux and higher order flux moments are given by

$$\psi_0(r,E) = \int_{4\pi} d\Omega \psi(r,E,\Omega) \tag{1.4}$$

$$\psi_{lk}(r,E) = \int_{4\pi} d\Omega Y_{lk}(\Omega)\psi(r,E,\Omega) \tag{1.5}$$

Grouped quantities, so-called effective MG microscopic XS, are defined as follows

$$\sigma_{tg}^i(r,\Omega) = \frac{1}{\psi_g(r,\Omega)} \int_{E_g}^{E_{g-1}} dE\sigma_t^i(\Omega,E)\psi(r,E,\Omega) \tag{1.6}$$

$$\sigma_{slkg'g}^i(r) = \frac{1}{\psi_{lkg'}(r)} \int_{E_g}^{E_{g-1}} dE \int_{E_{g'}}^{E_{g'-1}} dE'\sigma_{sl}^i(E' \to E)\psi_{lk}(r,E') \tag{1.7}$$

$$\sigma_{fg}^i(r) = \frac{1}{\psi_{0g}(r)} \int_{E_g}^{E_{g-1}} dE\sigma_f^i(E)\psi_0(r,E) \tag{1.8}$$

Since it is not practical to anticipate neutron spectrum in every angular direction with continuous energy in advance, the angular total XS in Eq. (1.6) is approximated using the scalar flux as below:

$$\sigma_{tg}^{i}(r)=\frac{1}{\psi_{0g}(r)}\int_{E_g}^{E_{g-1}}dE\sigma_{t}^{i}(r,E)\psi_{0}(r,E) \tag{1.9}$$

Multigroup approximation and angle discretization in Eqs. (1.1) through (1.9) significantly reduce the number of variables in energy for calculation. In order for the MG deterministic approach to achieve the expected predictive power, the accurate estimation of neutron flux, ψ , is required a priori to obtain the effective XSs. Instead of solving Eq. (1.1) explicitly with very fine energy group (or point-wisely) for the whole problem to obtain ψ , many approximations to energetical, angular and spatial neutron behavior can be applied to the problem of interest. For instance, because a steady-state flux distribution sustained by chain reaction has the similar shape regardless of energy in LWR applications, separation of variables [2] in energy and space given in Eq. (1.10) is a reasonable approximation as well as the angle discretization, which introduces an approximated weighting spectrum , ψ^{w} . Using this energy and space separation, in the early lattice calculation, the energetical self-shielding behavior was calculated in a homogeneous medium first (resonance treatment), and spatial self-shielding was considered later by solving a heterogeneous problem (lattice calculation) with the self-shielded XSs from the resonance treatment stage. In the past decades, the problem domain in the resonance treatment step has been extended from a mixture (0D) to one- or two-dimensions (1D or 2D) to overcome the energy and space non-separability within a pin cell. Due to the smoothness of energetical behavior of neutron in the high and thermal energy range, a key to generating accurate effective XS is the resonance self-shielding treatment for the estimation of scalar flux weighting spectrum, $\psi_0(r,E)$, in the intermediate energy range where numerous resolved and unresolved resonance peaks occur.

$$\psi_{lk}^{w}(r,E) \cong X(r) \cdot \Phi_{lk}(E) \tag{1.10}$$

1.2 Resonance Self-shielding Treatment

The resonance self-shielding treatment is one of the most important, but complicated part in the effective XS generation procedure. Various methods have been developed to estimate the resonance self-shielding behavior for specific reactor designs. In general, there are two major approaches to obtain the resonance self-shielded XSs in the deterministic methods: 1) the detailed slowing down approach and 2) the resonance integral (RI) table method. The first method has generally been selected as a starting methodology for fast reactor analysis, while the RI table methods and its branch methods have been widely used in LWR applications.

1.2.1 Detailed slowing down approach

The most rigorous approach to obtain the weighting spectrum, ψ_{lk}^{w} in Eq. (1.10), is to solve the detailed slowing down equation or transport equation by using millions of data points (pointwise, PW) or very fine group structure (>400,000 groups, hyperfine group). Hyperfine group (HFG) structure represents nuclear data points in nearly PW structure. The RABBLE program [3] was developed to solve the slowing down equation and to compute resonance absorptions in either a homogeneous or cylindrical cell. RABBLE also allows to compute the scattering source based on the assumptions that neutrons are scattered elastically and isotopically in the laboratory system. The RABBLE's algorithm was inherited to the RABANL module in MC^2-2 with an anisotropic scattering treatment [4], and was widely used in most XS generation codes that employ the direct slowing down approach. MC^2-3 [5] was developed at Argonne National Laboratory (ANL) by employing a transport equation with the ultrafine group (>2,000 groups, UFG) structure for fast reactor designs. The self-shielded UFG XSs in MC^2-3 are prepared by a numerical integration

using the PW XSs. In case that the UFG structure is not enough to represents resolved resonance peaks in the epithermal energy range, the HFG slowing down calculation can be invoked to eliminate remaining approximation errors in UFG XSs. Similarly, CENTRM in the SCALE/XSProc module [6] performs the problem dependent PW slowing down calculation to generate MG self-shielded XS data for resolved resonances. Recently, a new UFG (1,597G) XS library was developed to incorporate the detailed slowing down approach in this procedure [7]. However, because of many groups, the MC^2-3 and the CENTRM approaches are computationally inefficient to calculate microscopic XSs for the heterogeneous assembly geometry, and thus were only used for a homogenized assembly or small size problems.

1.2.2 Resonance integral table method

The concept of background XS was introduced by Bondarenko [8]. Bondarenko tabulates microscopic total XS in a homogeneous medium using the background XS [9], which indicates the dilution ratio of target isotope in the medium. The microscopic background XS of isotope *r* is defined as

$$\sigma_b^r = \frac{\sum_i N_i \sigma_{p,i}}{N_r} \tag{1.11}$$

where $\sigma_{p,i}$ is the potential scattering XS of nuclide i, and N_r is the number density of target resonant nuclide. Resonance integral (RI) is defined as the integrated resonance XSs weighted with the flux, which relates a physically measurable quantity, reaction rates, in experiments. In the Bondarenko method, these RIs are stored in a precomputed integral table (RI table), as a function of background XS to compute a self-shielding factor for resonance treatment of each resonant isotope. Using the equivalent theory [9], the RI table method can be applied to the heterogeneous

medium in the same manner as homogenous media by introducing an additional parameter, so-called effective escape XS, (σ_e), as follows:

$$\sigma_b^r = \frac{\sum_i N_i \sigma_{p,i} + \Sigma_e}{N_r} \tag{1.12}$$

In the conventional equivalence theory, the fuel escape probability was estimated using the rational approximations such as Wigner's one-term or Carlvik's two-term approximation [9]. While the detailed slowing down approach has been limited to relatively small problems due to its computational cost, the RI table method has a huge computational advantage against the detailed method in terms of online MG XS generation for practical whole core analysis of power reactors that involve depletion and T/H feedback [10]. It enables the creation of MG XSs for any composition from a single isotope-wise library, which is critical to reduce computing costs during data processing prior to transport calculation.

Since the escape probability is obtained using the one- or two-term rational approximation of a simplified two-region (fuel and moderator) problem (homogeneous model), an inconsistency arises between the RI table preparation and real heterogenous calculation. To provide better consistency between two calculations, the RI table is recently generated by solving the detailed slowing down equation repeatedly for multiple simplified heterogeneous pin cell configurations (heterogeneous model). This imposed equivalence relationship between the heterogeneous model and the real heterogeneous problem is widely used in modern lattice codes that employ the RI table method. For clarification, the RI table in this dissertation indicates the table generated using the heterogeneous model. The RI table method is often based on the narrow resonance infinite mass (NRIM) approximation with the intermediate resonance (IR) factor λ.

$$\sigma_b^r = \frac{\sum_i N_i \lambda_i \sigma_{p,i} + \Sigma_e}{N_r} \tag{1.13}$$

$$\phi(u) = \frac{\lambda \sigma_p + \sigma_b^r}{\sigma_a(u) + \lambda \sigma_s(u) + \sigma_b^r}, \ 0 \le \lambda \le 1 \tag{1.14}$$

where σ_s is the resonance scattering microscopic XS. When $\lambda = 1$, the Eq. (1.14) becomes the narrow resonance (NR) approximation and when $\lambda = 0$ it becomes the NRIM approximation. Since the atomic mass of hydrogen is so near to unity, the intermediate resonance parameter is set to one, which is equivalent to the NR approximation. The intermediate resonance parameter for other isotopes is calculated by a hydrogen-equivalence parameter, which compare the results of several ^{238}U and ^{1}H mixes in which the hydrogen is partially replaced by the other isotopes.

In the last three decades, the subgroup method [11] becomes one of the most noticeable approaches with an alternative concept of precomputed resonance data table and equivalence theory. To deal with unresolved resonances, the subgroup approach is derived from the probability table method [12]. The main idea of the subgroup method is to replace the absorption RI and scalar flux using a quadrature. The lethargy dependence, u, in Eq. (1.14) are replaced by σ_a in the MG formulation as follows [13]:

$$\frac{1}{\Delta u}\int_{\Delta u} f(u)du = \frac{1}{\Delta u}\int_{\Delta u} f(\sigma_a)\frac{du}{d\sigma_a}d\sigma_a = \frac{1}{\Delta u}\int_{\Delta u} f(\sigma_a)p(\sigma_a)d\sigma_a \cong \sum_n \omega_n f(\sigma_{an}) \tag{1.15}$$

where n indicates the discrete level of absorption which is subdivided into σ_{an} and their weight ω_n. Using this the effective XS can be approximated as

$$\sigma_a = \frac{\sum_n \omega_n \sigma_{an} \phi_n}{\sum_n \omega_n \phi_n} = \frac{\sum_n \omega_n \sigma_{an} \frac{\sigma_{bn}}{\sigma_{an} + \sigma_{bn}}}{\sum_n \omega_n \frac{\sigma_{bn}}{\sigma_{an} + \sigma_{bn}}} \tag{1.16}$$

The subgroup technique may more correctly tackle the spatial self-shielding effect caused by local heterogeneity inside an assembly by solving the subgroup fixed source problem, whereas the previous RI table method is confined to a few region cells. Since the subgroup method is not used in this work, the methods to generate subgroup parameters and data are not covered here. The detailed procedure for the subgroup method can be found in [14].

Another variation of RI table approach is the iterative approach, which uses fixed source transport computations to directly estimate the effective resonance XSs for each resonance nuclide. [15]. Oak Ridge National Laboratory (ORNL) developed the embedded self-shielding method (ESSM) [16] which was extended to the spatially dependent ESSM (SDESSM) [17], or ESSM-X [18] to obtain spatially dependent self-shielded resonance XS inside a fuel. ESSM is similar to the subgroup approach. While the subgroup method includes the errors in least squares fitting to create subgroup parameters, ESSM, however, does not have these biases. In addition, the ESSM method can be used in entire energy groups while the subgroup methods are generally used only for resonance groups. To optimize the ESSM method further, the equivalent Dancoff factor cell (EDC) model [19] is recently applied to the ESSM (Cell ESSM, preliminarily named in this work). In this work, the XS library for high-fidelity simulation is generated using ESSM and Cell ESSM. Therefore, the detailed methodology of ESSM and Cell ESSM will be described in Chapter 3 and 4, respectively.

1.3 Limitations of the Current Deterministic Multigroup Cross Section Generation Approach

All the MG XS generation procedures have various degrees of inherent limitations. As mentioned in the previous section, most thermal reactor applications rely on the RI table method, while the fast reactor community uses the detailed slowing down approach. Thus, their limitations

are in common depending on the starting methodology and the approximations made on the selected method. To overcome these limitations, either more rigorous approximations were developed, or other corrections (e.g., resonance interference factor) were introduced to the existing method. However, the approximation fails whenever the fuel composition or problem domain varies significantly. In this section, the inherent causes of bias in each method are demonstrated.

1.3.1 Limitations of the detailed slowing down approach

To account for important physics in high energy region, the XS generation method for fast reactor applications utilizes the detailed slowing down calculation. For example, MC^2-3 performs the detailed slowing down calculation by dividing the entire energy range into UFG (>2,000) with equally spaced lethargy width, approximately equivalent to half of the maximum lethargy increment per collision of ^{238}U to properly model the broad resonances of nuclide with the intermediate weight at fast energy range [13]. However, the MC^2-3 XS generation procedure does not include the XSs in the thermal energy region and uses rather simple models for local heterogeneity while the important physics in high energy region are modeled accurately through detailed slowing-down calculation. Similarly, the ECCO code [20] performs the slowing down calculations with the ultrafine group structure (1,968 groups) using the subgroup method, and the SCALE 6.2 code package recently releases 1,597 group AMPX MG XS library for the fast reactor analysis [7]. However, a preliminary verification of 1,597 group AMPX XS library demonstrates that there is an underlying bias due to the limitations of the RI table methods (e.g., base weighting spectra, scattering transfer matrix, resonance interference effect etc.), despite the increased number of groups. In addition, high fidelity codes usually employ a single problem independent XS library based on the RI table that cannot be used for reactor designs other than PWR.

On the other hand, the MC^2-3 method can handle these limitations by solving the composition dependent problem directly instead of generating the RI table. However, the direct whole core calculation with the MG XS library is in line with the latest paradigm shift in nuclear design from the two-step procedure to the high fidelity calculation. The high-fidelity simulation requires the speed of which the resonance treatment should be applied online XS generation with the different burnup and T/H feedback. Thus, independent of the detailed slowing down approach's accuracy benefits and their partial success on the multistep procedures, it is inevitable to utilizes the RI-table XS library in high-fidelity simulation to reduce the computational time.

1.3.2 Limitations of the RI table method

At first, the rigor in treatment of the slowing down equation is lacking in the RI table method; thus, nontrivial errors are introduced if the target flux spectrum deviates significantly from the original weighting spectrum. For example, the current BG XS libraries for LWR applications are typically prepared based on the reference PWR pin cell slowing-down calculations with various approximations in the energy range above resolved resonance region of ^{238}U. The actual assembly or core configuration could be significantly different from the one calculated using the RI table due to the fact that the RI table was generated using the relatively small problem domain and fixed composition (e.g., a fixed fuel pin geometry, simple UO_2 fuel with water). As a result, its application to BWR, which is more heterogeneous than PWR, introduces non-negligible errors in important neutronics parameters due to the complex geometry and hardened spectrum originated from high void fraction at the top of the core.

In addition, because the RI table method assumes a single resonant isotope in a composition, the resonance interference effect is not well captured in the Bondarenko iteration as the number of resonant nuclides in mixture increases. Though many attempts to correct this bias

using resonance interference factors, this correction approach cannot be the fundamental resolution of the current isotopic RI-table generation procedure. Secondly, in preparation of thermal reactor RI table, the resonance self-shielding focuses on resolved resonances of heavy nuclides with an approximate treatment or neglect of unresolved resonances of heavy nuclides, broad resonances of intermediate mass nuclides, and anisotropic scattering in high energy region. Moreover, these broad resonances cannot be well represented in a coarse group structure. For example, Figure 1.1 shows ^{238}U, ^{16}O and ^{90}Zr total XSs of the highly voided BWR problem. It can be seen from the figure that the broad scattering resonances of ^{90}Zr are overlapped with the resolved and unresolved resonances of ^{238}U and they cannot be treated as constant background XSs for ^{238}U XS self-shielding in a coarse group. Similarly, in the fast reactor analysis, Figure 1.2 shows the total XS of ^{239}Pu, ^{23}Na and ^{56}Fe of the ABTR problem. Comparison between Figure 1.1 and Figure 1.2 suggests that the resonance overlapping effect mainly caused by the broad resonances of structural material becomes more dominant as the spectrum is more hardened and more structure materials are included. Lastly, since the advanced compact reactor designs, such as small modular reactors or micro-reactors, are leaky, the global leakage and the anisotropic scattering higher than P_3 that are often neglected in large thermal reactors becomes important.

For these reasons, the RI table based XS generation procedure for thermal reactor applications needs to be improved for the advanced reactor applications in which resonance overlapping, spatial transition and local heterogeneity effects are important. To cover a wide range of state changes in the high-fidelity calculation, it is essential to develop a problem dependent BG XS library generation procedure for the high-fidelity simulation since a single weighting spectrum and resulting XS library cannot satisfy all important physics addressed in this section.

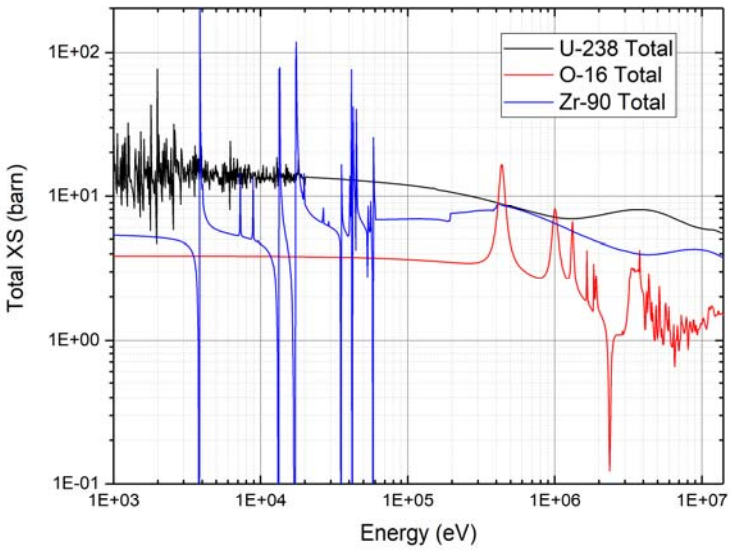

Figure 1.1 Total cross section of ^{238}U, ^{16}O and ^{90}Zr

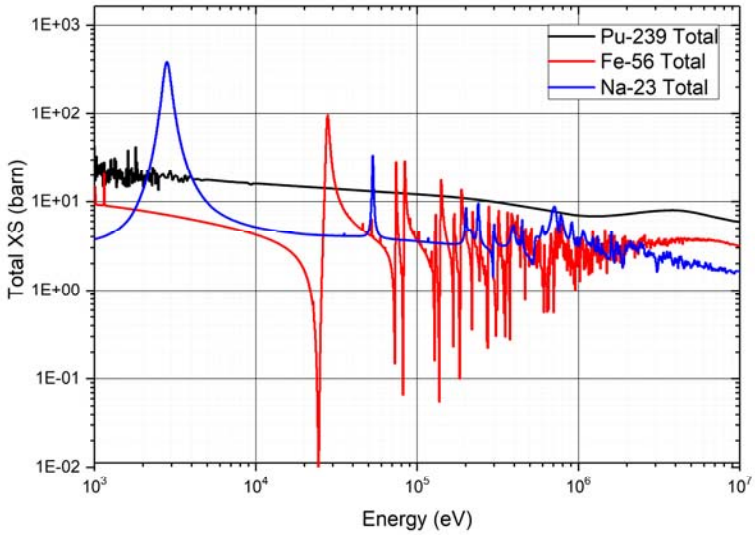

Figure 1.2 Total cross section of ^{239}Pu, ^{56}Fe and ^{23}Na

1.3.3 Complicated fuel design with double heterogeneity

Conventional High Temperature Gas-Cooled Reactors (HTGR) and many of recent pebble bed concepts reactors use TRISO (TRi-structural ISOtropic) fuel grains embedded in a ceramic or

metal matrix. At the same time, the trend of reactor fuel design is shifting from the typical UO_2 fuel to accident tolerant fuel including TRISO particles that can improve the safety of both existing and new nuclear plants. The double heterogeneity of these particulate fuels is due to randomly scattered fuel particles in fuel compacts or pebbles that are heterogeneously distributed in the core. This heterogeneous behavior should be accounted for in generating MG XSs by proper energy and spatial self-shielding of resonances. A simple volume-averaging approach would result in the considerable underestimation of the reactivity due to the disregard of spatial self-shielding in fuel particles. Although there exist attempts to model the double heterogeneous fuel in 1D collision probability method (CPM) [21] and 2D method of characteristics (MOC) [22] transport solvers, none of those extended its usage to the XS library generation, especially for the heterogeneous model discussed in subsection 1.2.2, and the subsequent resonance calculation in the high fidelity simulation. Thus, a proper method to treat the double heterogeneity effect should be developed and implemented consistently in both the RI-table generation procedure and downstream lattice calculation.

1.3.4 Accurate coupled neutron and gamma heating estimation

Any nuclear reactor's design and operation requires an accurate prediction of power or heat distribution. Gamma heating is a key contributor to heating, especially in non-fuel areas, and it is crucial for calculating design limitations on peak temperature, thermal stresses, and other safety design parameters for nuclear materials. In sodium-cooled fast reactors (SFRs), for example, it is known that gamma heating can account for about 90% of the total power in a reflector. Thus, the explicit modeling of gamma transport and accurate gamma data are crucial as well as the neutron heating. For that, most neutronic simulators use combined neutron and gamma heating computations to evaluate an accurate distribution of neutron and gamma heating rates. Monte

Carlo codes provide a coupled neutron and photon transport simulation to account for the effect of gamma heating although delayed gamma component of gamma heating is often approximately treated in the heat deposition model. Recent deterministic codes also have the coupled neutron and gamma library and transport capability. For example, the SCALE code package distributes the coupled neutron and gamma XS libraries with the latest version of the ENDF/B database and provides the transport capability. On the other hand, the coupled neutron and gamma heating calculation method [23] for fast reactors was developed by ANL to calculate the coupled neutron and gamma heating in whole core. In this method, XSs were generated using the MC^2-3, and the neutron and gamma flux distributions were calculated using the DIF3D and GAMSOR codes [24]. Although this gives an improved total heat estimation, the gamma XS library generation procedure of MC^2-3 needs to be improved because a temporary NJOY [25] processed 21-group gamma library of MC^2-3 [26] does not account for the gamma transport and self-shielding effect of KERMA (Kinetic Energy Released in Material) factor. In addition, most codes and libraries do not include the explicit delayed gamma simulation capability and corresponding data. For the accurate total heat estimation, more accurate gamma library and subsequent gamma XS generation procedure should be developed as well as the one of neutron interactions.

1.4 Research Objectives and Thesis outline

This dissertation proposes to develop a generalized MG XS generation method for high-fidelity simulation of advanced reactors, which properly represents all the required physics effects by eliminating the dominant approximations of the current methods. To overcome inherent limitations of two methodologies aforementioned in previous sections, the approach that this research take is akin to the concept of "the detailed slowing down approach" of MC^2-3 for "the RI table based XS library generation" for the high-fidelity neutronic simulation of advanced reactor

designs. This overarching objective is achieved through the following approaches: (1) explicit modeling of resonance and anisotropic scattering of all isotopes by employing the detailed slowing down calculation, (2) proper consideration of spatial self-shielding for all regions, (3) development of an efficient lattice transport calculation method through a generalized condensation scheme, (4) preparation of problem-dependent cross section libraries with respect to background cross section and material temperatures, (5) development of a double heterogeneity treatment capability for particulate fuel modeling, and (6) generation of accurate gamma cross section library for coupled neutron and gamma heating calculations.

The new procedure and library should yield substantially improved results for both eigenvalue, reaction rates and heating estimation, which help to improve the accuracy of high-fidelity neutronic calculations for advanced reactor designs including PWR, BWR, fast-thermal hybrid reactor, HTGR and HTR.

With emphasis on the novel generalized MG XS generation procedure, the dissertation provides the following notable advancements as the first attempt:

- to generate MG XS using a single slowing-down based procedure for a wide range of problems, such as PWR, BWR, fast reactors, fast-thermal hybrid spectrum reactor, HTGR and HTR,
- to quantify anisotropic scattering, local heterogeneity, global transition effects in terms of reactivity change due to reaction rate differences during the group condensation,
- to generate the RI table by solving the heterogeneous lattice explicitly instead of the unit pin cell,

- to provide the user options to choose parameters for tabulating the background XSs and having a multiple scattering matrix according to the background XSs,
- to develop the novel double heterogeneity resonance treatment method for the lattice calculation of high-fidelity simulation.
- to examine the self-shielding effect on KERMA and gamma heating factors as well as the gamma spatial transition effect in the MG gamma XS generation.

Chapter 2 Detailed Ultrafine/Hyperfine Group Transport Calculation

This chapter demonstrates a new self-shielded BG XS generation procedure based on the MC^2-3 method. The goal of this chapter is to produce multiple BG XSs condensed with the UFG slowing down solutions at different compositions (e.g. background XSs) to construct the reactor dependent BG XS library for the high-fidelity calculations in Chapters 3 and 4. Section 2.1 describes how MC^2-3 solves the detailed slowing down equation using the UFG structure for fast reactor studies to shows the accuracy of the current MC^2-3 method at higher and epithermal energy range. The MC^2-3 code cannot be directly used for the XS generation of thermal reactor due to the lack of the thermal data and transport calculation capability. For that, a new thermal library was developed to extend its functionality to thermal reactor analysis, and existing MC^2-3 transport capabilities were modified correspondingly. Combined with the current and extended capabilities, MC^2-3 can generate effective XSs regardless of the reactor's energy spectrum using the UFG slowing down calculation.

One of the important achievements in this dissertation is the generalized condensation scheme described in section 2.2 to yield significant reductions in MC^2-3 execution times by determining the contributions of each approximation made in calculation to properly reduce the number of groups in the assembly calculation without losing its accuracy in the UFG level. Numerical results to show the effectiveness of the detailed slowing down approach with the generalized condensation scheme for various rector designs are presented in section 2.3.

2.1 Generation of Ultrafine Group Cross Sections

MC^2-3 employs the detailed slowing down approach with the UFG structure. Unlike other MG XS processing routines that use the slowing down or RI table methods, MC^2-3 approaches are unique since it was designed specifically for fast reactor designs. Rigorous treatments of UFG XSs allows the MC^2-3 methodologies to be potentially applicable to the wide range of reactor applications. This is the main reason for selecting the MC^2-3 methodologies as a start basis in altering the current MG XS procedure. MC^2-3 uses the 2,082 group UFG structure inherited from the MC^2-2 for multi-dimensional transport calculations. The upper and lower energy bounds are 14.2 MeV and 0.414 eV, respectively. All the energy groups have the same lethargy width of 1/120 as Δu . This lethargy width is corresponding to the average lethargy gain of a neutron from scattering with ^{238}U so that the practical resonance width at high energy groups are much narrower than the average energy loss by scattering. This indicates that the neutrons are likely to have a collision and can escape from within energy group. With this UFG structure, the brief XS generation methodologies, changes and improvements are given in this section.

2.1.1 Resonance treatments and scattering transfer matrix

In the fast reactor XS generation, the narrow resonance (NR) approximation is a good approximation for the estimation of the resonance absorption of heavy nuclide such as the fissile and fertile isotopes in fuel. The NR approximation is valid when the resonance width is much narrower than the average energy loss per neutron scattering, thus it is valid in the most energy range higher than a few hundred eV for heavier isotope. If one assumes that the absorber has an infinite mass, the energy loss due to collisions with the absorber can be ignored. Then, the NR approximation becomes the NRIM (narrow resonance infinite mass) approximation. Since the NR approximation breaks for the self-shielding of the broad scattering resonances of intermediate

weight nuclides, the UFG structure was adopted so that those MG XSs can be treated as smooth XS within the UFG structure. With the NR approximation, the neutron spectrum with the uniform lethargy width Δu is reduced to

$$\phi(u) = \frac{\Sigma_b}{\Sigma_t(u)} = \frac{\Sigma_b}{\Sigma_{tR}(u) + \Sigma_b} \tag{2.1}$$

where Σ_{tR} is the total macroscopic XS of resonance nuclide and Σ_b is the total macroscopic background XS. Using the NR and B_0 approximations, the higher order flux moment is given by

$$\phi^l(u) = \frac{1}{[\Sigma_t(u)]^{l+1}} \tag{2.2}$$

Using the NR approximation, the l-th order Legendre moment of effective microscopic XS at group g can be obtained as

$$\sigma_{xg}^l = \int_{u_g}^{u_{g-1}} \frac{\sigma_x(u)\Sigma_p(u)}{[\Sigma_t(u)]^{l+1}} du \Big/ \int_{u_g}^{u_{g-1}} \frac{\Sigma_p(u)}{[\Sigma_t(u)]^{l+1}} du \tag{2.3}$$

Note that the potential scattering, Σ_p, can be treated as a constant within UFG. It should be noted that the difference between Eq. (2.1) and Eq. (1.14) is the usage of macroscopic XS as a means to incorporate the resonance interference effect in MC^2-3. In resolved resonance energy, the Doppler-broadened XSs are reconstructed in HFG using the resolved resonance parameters or as a PW data from the existing PW output file (PENDF) pre-processed by NJOY. Self-shielded XSs for resolved resonance energy are evaluated using a simple numerical integration as Eq. (2.3). For the unresolved resonance treatment, the unresolved parameter given in the MC^2-3 library are used to calculate infinitely dilute and effective XSs of the materials in the unit geometry. In MC^2-3, the infinitely dilute XSs are obtained in fluctuation integral of the Doppler broadened XS using the unresolved resonance parameters. The self-shielded XSs in the unresolved resonance region can be calculated based on the direct integration using the joint probability distribution of resonance

parameters. To account for the overlaps between resonances the energy grid points are significantly increased from the MC^2-2 library.

MC^2-3 calculates the elastic scattering transfer matrix in three different ways. Each isotope is categorized into three classes, depending on the maximum number of down-scattering group: hydrogen, light and heavy elements. For heavy elements, which scatters up to three ultrafine groups, the Henryson's method [4] is used. The l-th moment multigroup scattering transfer matrix can be written using a Legendre polynomial expansion as

$$\sigma_s^l(g \to g') = \frac{1}{\phi_{l\,\mathrm{g}}} \int_{u_{g'-1}}^{u_{g'}} du' \int_{u_{g-1}}^{u_g} du \, \frac{\phi_l(u)\sigma_s(u)e^{-(u'-u)}P_l[u_s(u,u')]}{(1-\alpha)} \sum_{n=0}^{N} (2n+1) f_n(u) P_n[u_c(u,u')] \quad (2.4)$$

Under the assumptions of constant flux and XS within ultrafine group, Eq. (2.4) can be simplified as

$$\sigma_s^l(g \to g') = \frac{\sigma_{sg}}{(1-\alpha)\Delta u} \sum_{n=0}^{N} (2n+1) \int_{u_{g'-1}}^{u_{g'}} du' \int_{u_{g-1}}^{u_g} du f_n(u) P_l(u_s) P_n(u_c) e^{-(u'-u)} \quad (2.5)$$

where σ_s^l is the l-th moment Legendre expansion coefficient of the scattering transfer matrix from group g to g', and σ_{sg} is the elastic scattering XS of group g. $u_{g'}^*$ and u_{g-1}^* are energetically reachable boundaries, Δu is the lethargy width, $\alpha = (A-1)^2/(A+1)^2$ and A is the atomic mass ratio of scattering nuclide to neutron. Henryson reformulates Eq. (2.5) as

$$\sigma_s^l(g \to g') = \frac{1}{\phi_{\mathrm{lg}}} \sum_{n=0}^{N} < \phi_{\mathrm{l}}(u)\sigma_s(u) f_n(u) >_g \; A_n^l(g \to g') \quad (2.6)$$

$$< \phi_{\mathrm{l}}(u)\sigma_s(u) f_n(u) >_g \approx \frac{\phi_{\mathrm{lg}}}{\Delta u} \sigma_s \overline{f_{ng}} \quad (2.7)$$

where $<>$ is an average over the source group g, $\overline{f_{ng}}$ is the group-averaged Legendre coefficients. $A_n^l(g \to g')$ is given by

$$A_n^l(g \to g') = \frac{2n+1}{1-\alpha} \int_{u_{g-1}}^{u_g} du \int_0^{\ln(1/\alpha)} dU P_l[u_s(u)] P_n[u_c(U)] e^{-(U)} = T_{\ln}^0(\alpha) \Delta u \tag{2.8}$$

where $T_{\ln}^m(\alpha) = \frac{(-1)^m}{m!} \frac{2n+1}{2} \int_0^{-\ln\alpha} dU U^m P_l[u_s(u)] P_n[u_c(U)] \left(-\frac{d\mu_c}{dU} \right)$, so-called the incomplete gamma function.

For light elements, Eq. (2.5) was reformulated to define the scattering probability, $P_l(u \to g')$, as

$$\sigma_s^l(g \to g') = \frac{\sigma_{sg}}{\Delta u} \int_{u_{g-1}}^{u_g} du P_l(u \to g') \tag{2.9}$$

$$P_l(u \to g') = \sum_{n=0}^{N} \frac{(2n+1)}{(1-\alpha)} \int_{u_{g'-1}}^{u_{g'}} du' f_n(u) P_l(u_s) P_n(u_c) e^{-(u'-u)} \tag{2.10}$$

By changing the variable from u' to r, the scattering probability can be represented as

$$P_0(u \to g') = \sum_{n=0}^{N} A_m(u) (r_{g'}^{m+1} - r_{g'-1}^{m+1}) \tag{2.11}$$

where $A_m(u) = \sum_{n=m}^{N} \frac{(-1)^m (n+m)!}{m!(m+1)!(n-m)!} (2n+1) f_n(u)$ and $r = \frac{1-e^{-(u'-u)}}{(1-\alpha)}$. Using the analytic expression in Eq. (2.11), a numerical integration was used by dividing the ultrafine source group (g) and sink group (g') into several subgroups to evaluate the scattering probability. The number of subgroups per ultrafine group is chosen to make the discretization error of numerical integration negligible. For hydrogen, Eq. (2.5) can be simplified as

$$\sigma_s^l(g \to g') = \frac{\sigma_{sg}}{(1-\alpha)\Delta u} \int_{u_{g'-1}}^{u_{g'}^*} du' \int_{u_{g-1}^*}^{u_g} P_l[e^{-(u'-u)/2}] e^{-(u'-u)} \tag{2.12}$$

Inelastic energy transfer matrix is also calculated for elastic scattering matrix using on the secondary energy distribution laws in ENDF/B raw data [27] as well as the (n, 2n) matrix. While the most MG XS library employs fission spectrum vector and average number of fission neutrons

because of the thermal fission assumption, incident energy dependent data are used in MC^2-3 to consider the fission at entire energy range. Detailed MC^2-3 methodologies that are not described here can be found in [5].

In summary, the detailed slowing down approach in MC^2-3 can accurately model:

1) the resolved and unresolved resonance self-shielding behaviors using the NR approximation and the usage of PW data,
2) the resonance overlapping effects by using the total macroscopic XSs of the mixture and the PW XSs in UFG XS generation,
3) the anisotropic effects using the explicit theoretical model as well as the inelastic and (n, 2n) reactions,
4) the self-shielding effect of intermediate weight nuclide, such as iron, chromium, at high energy range.

Even though it would be time consuming when it is directly applied to thermal reactors where local heterogeneity effects are important, MC^2-3 methodologies are chosen to produce the BG XSs for the XS library generation due to the above incomparable advantages over other methodologies. However, a question that arises at this point is whether the MC^2-3 code itself is adequate for outside of fast reactor analyses. For the thermal reactor analysis, the methodologies should be improved with resolving two current limitations that were approximated in fast reactor analyses: the limitations of the NR approximation below a few hundred keV and the lack of the thermal data and transport calculation capability of MC^2-3. To address the first issue, the MC^2-3 adopted the UFG and HFG iteration approach.

2.1.2 Ultrafine/Hyperfine group transport calculation

The NR approximation is not valid under a few hundred eV. One approach to eliminating the UFG XS bias is the so-called "hyperfine group" slowing down method implemented in the RABANL integral transport option of the MC^2-2 code [4]. In this method, a UFG scattering interval is split into numerous evenly spaced hyper-fine groups with a width much smaller than the extent of the resonances under concern. The hyper-fine group width is set to be less than one quarter of the Doppler width. Inelastic and (n,2n) scattering sources, fission sources at energies above the upper limit of the RABANL energy range are treated as external sources. MC^2-3 also uses the same hyperfine group method of RABANL with the increased upper energy limit and anisotropic elastic scattering treatment. The UFG transport calculation is performed in the first step to obtain the fission, inelastic scattering and (n,2n) HFG sources, which are interpolated from the corresponding UFG sources. After the HFG fixed source calculation, the self-shielded UFG XSs are recalculated using the HFG flux distribution. The scattering matrices are also recalculated using the HFG solution to resolve the constant flux approximation in Eq. (2.5). Note that the UFG/HFG iteration is repeated until the UFG XSs converge, even though only one or two iteration is enough for most cases. Note that this HFG calculation is available for all geometries (infinite medium, cylindrical and slab geometry unit cells) in MC^2-3. Recently, to account for the local heterogeneity effect, the 2D UFG MOC solver for rectangular and hexagonal geometry is incorporated into MC^2-3 as well as the HFG MOC solver. Figure 2.1 compares the relative error of self-shielded UFG capture XSs of ^{238}U determined with the UFG only and the UFG/HFG iteration against the reference MCNP6 solution for the homogenized compositions of MOX fuel pin cell problems. It can be seen from Figure 2.1 that the HFG calculation significantly improves the XS accuracy by reducing the errors resulting from the NR approximation.

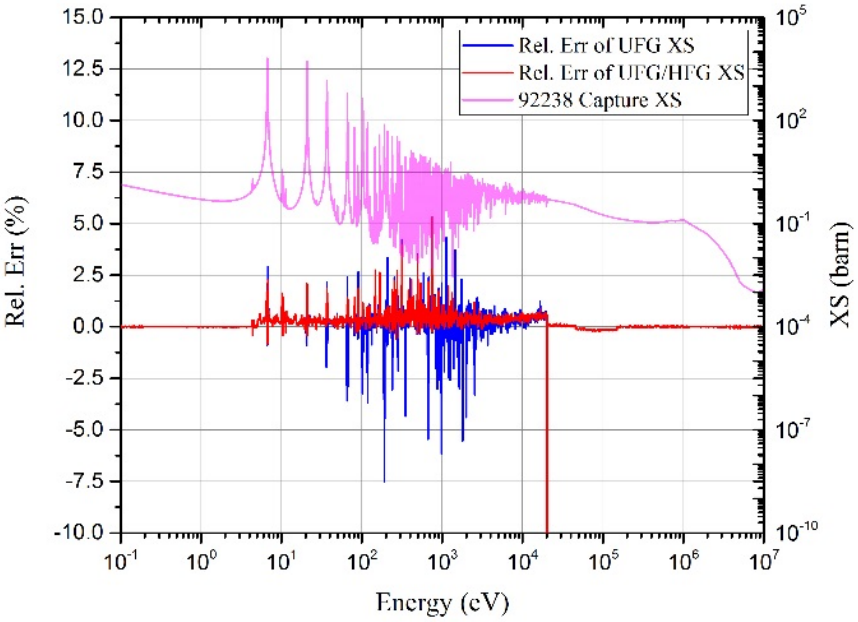

Figure 2.1 Comparison of the UFG capture XS of ^{238}U between MC^2-3 and MCNP6 for homogenized MOX fuel.

2.1.3 Generation of thermal cross section data

For taking the rigors of the detailed slowing down calculation of MC^2-3 to be used for thermal reactor MG XS generation, in particular for those cases where the current lattice calculation with BG XS libraries is not adequate (e.g., BWR assembly with high-void fraction), the MC^2-3 code has been extended to generate the MG XSs in the thermal energy range as well as in the fast energy range. For a detailed thermal spectrum calculation, the lower energy boundary has been extended from 0.4 eV to 10^{-5} eV. Using the NJOY code, 1,700-group basic thermal XS libraries have been generated to cover the energy range from 10^{-5} eV to 5.0 eV. The existing transport equation solvers have also been modified to comply with the new thermal libraries with up-scattering boundary up to 10 eV. The energy range from 0.1 eV to 5.0 eV that includes important thermal resonances was divided into 1,625 groups to represent the thermal resonances

in this energy range almost PW. The energy range from 10^{-5} eV to 0.1 eV, where the XSs vary smoothly, was represented by 75 groups. As a result, the total number of ultrafine groups of MC^2-3 becomes 3,483: 1,783 fast groups from 5.0 eV to 14.2 MeV and 1,700 thermal groups from 10^{-5} eV to 5.0 eV.

The NJOY code was used to generate the thermal scattering matrices and the interaction XS libraries at the infinite dilute condition and target temperatures. Figure 2.2 illustrates the computational procedure. An automated procedure to generate the new thermal XS library for MC^2-3 was established by developing the pre- and post-processing tools for the NJOY code. The automation is especially beneficial for this application in that it can eliminate the cumbersome efforts to prepare the user inputs for individual isotopes required in NJOY run as well as can prevent the potential input errors. For these reasons, two utility codes, PreMCS and GenMCS for MC^2-3 sub-library generation have been developed. The PreMCS code generates NJOY input files for the MG XSs, a batch file to execute the NJOY code and an input file of GenMCS. The thermal scattering matrices and XS libraries are generated using the RECONR, BROADR, THERMR and GROUPR modules of NJOY. The GenMCS converts the output files of NJOY in the formats of the thermal XS libraries of MC^2-3.

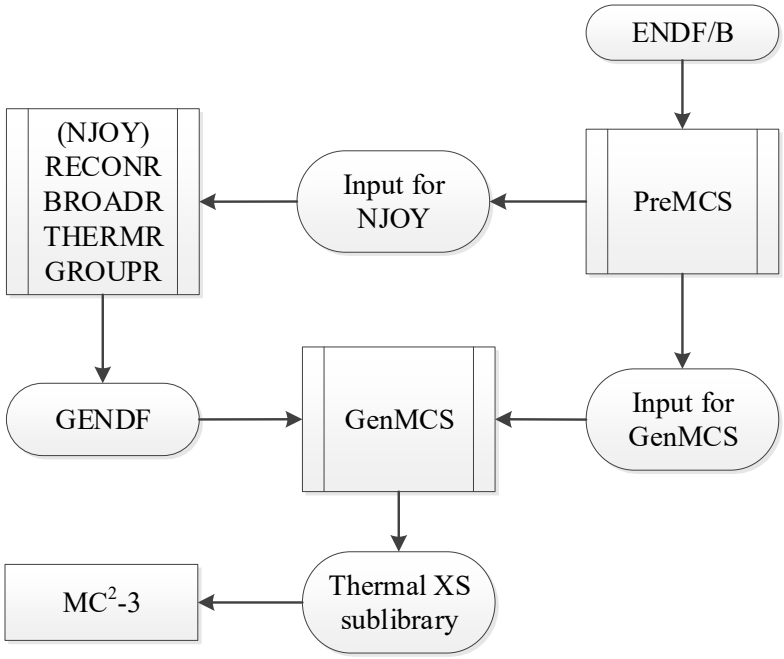

Figure 2.2 Procedure to prepare the thermal libraries of MC^2-3.

Since only the thermal scattering matrices are prepared with the NJOY code, the elastic and inelastic scattering XSs from fast groups to thermal groups are prepared using the MC^2-3 algorithms of section 2.1.1 except for hydrogen. For this, the associated routines of MC^2-3 have been modified to comply with the thermal group structure. As shown in Eq. (2.8), Henryson's method takes advantages of the uniform group structure to use pre-calculated incomplete gamma functions, directly given in the MC^2-3 library. Due to the irregular group structure and absence of incomplete gamma function for thermal energy range, this method is inadequate for the calculation of scattering XSs from fast groups to thermal groups. Thus, the method for the light elements was used to generate scattering XSs from fast groups to thermal groups for both light and heavy elements. The scattering XSs from fast groups to thermal groups for light and heavy elements were evaluated based on the Eq. (2.11). Since the thermal group structure from 0.1 eV to 5.0 eV is almost PW and energetically reachable boundaries is higher than 0.1 eV for most isotopes, only

the source group was divided into several subgroups. The number of subgroups for the light elements is chosen in the same way as ultrafine group scattering matrix, and the number of subgroup for the heavy elements is set to a hundred empirically. For hydrogen, the elastic scattering transfer matrix is analytically obtained as:

$$\sigma_s^l(g \to g') = \frac{\sigma_{sg}}{(1-\alpha)\Delta u} \int_{u_{g'-1}}^{u_{g'}^*} du' \int_{u_{g-1}^*}^{u_g} du P_l[e^{-(u'-u)/2}] e^{-(u'-u)} \tag{2.13}$$

In the 1,783 fast UFGs, only down-scatterings were considered and up-scatterings from 1,700 thermal UFGs were not considered. And the down-scattering XSs were based on the asymptotic kernel in which the thermal agitation of target nuclides is not considered. Since this limitation induced non-negligible errors on spectrum solution and reactivity, the energy cut-off for the thermal scattering treatment increased from 5 eV to 10 eV.

2.2 Generalized Condensation Scheme

The previous section focused primarily on introducing MC^2-3 methodologies and extending the method to the thermal energy range to eliminate the XS bias resulting from the energetic MG formulation. The current section will demonstrate the changes made to the current group condensation scheme in a comprehensive and efficient manner by quantifying important nuclear physics of each reactor configuration such as spatial self-shielding and anisotropic scattering effects in reaction rate contribution to reactivity changes. Up to this point, the UFG XSs are determined using the NR approximation or the UFG/HFG iteration to properly consider the energy self-shielding effect. Even though the UFG slowing down equation can be solved directly for the lattice or tiny core problems, a single heterogeneous assembly computation would take hours or even days, which makes it not practical nor feasible in most cases. To make this practical, the generalized condensation scheme was developed to accelerate the UFG slowing down

calculation by reducing the number of groups in the assembly calculation. The new condensation scheme also resolved the limitations of the current multi-step group condensation approach, which will be discussed in the subsection 2.2.1.

2.2.1 Limitations of the current multi-step sequential group condensation scheme

In the current multi-step group condensation scheme, the UFG or PW XSs are employed in either a heterogeneous pin cell or homogeneous assembly calculation for an intermediate group (< a few hundreds, IG) XS generation in the first stage of the present multistep condensation process. In the second step, the spatial physics calculation models spatial self-shielding effects between pins or assemblies of various compositions, and it collapses IG XSs into BG XSs. For example, in the XSProc module of SCALE [6], a 1D SN or 2D MOC pin cell transport calculations are performed for the resolved resonance (RR) energy region using PW data, while the MG calculations using the Bondarenko method are performed for the above RR and thermal groups assuming the smooth variations of XSs. Then, IG XSs are collapsed into a few group (<10, FG) XSs using the heterogeneous lattice calculation (e.g., NEWT [6]) result. Other modern lattice codes, such as WIMS [28], CASMO [29], and DRAGON[30], also use the similar multistep approaches with varying target problems and design parameters. Figure 2.3 presents a conventional multistep XS generation procedure for the LWR analysis. The multistep condensation is frequently performed without or just partially accounting for the effect of inter assembly or core heterogeneities on the flux spatial distribution. All approaches offer varying degrees of simplification for local heterogeneity and global spatial transition effect, as well as the anisotropic scattering treatment, to obtain the optimal trade-off between accuracy and efficiency. In the LWR analysis, due to the presence of light water, the leakage effect and anisotropic scattering moments higher than P_1 are often treated approximately. For instance, the leakage

effects are taken into account by using a homogeneous leakage model [31] (e.g., consistent B1 approximation) in which the flux can be factorized as

$$\psi^{w}(r,\mathrm{E},\Omega) \cong \psi(r,\mathrm{E},\Omega)e^{iBr} \tag{2.14}$$

where B is the buckling.

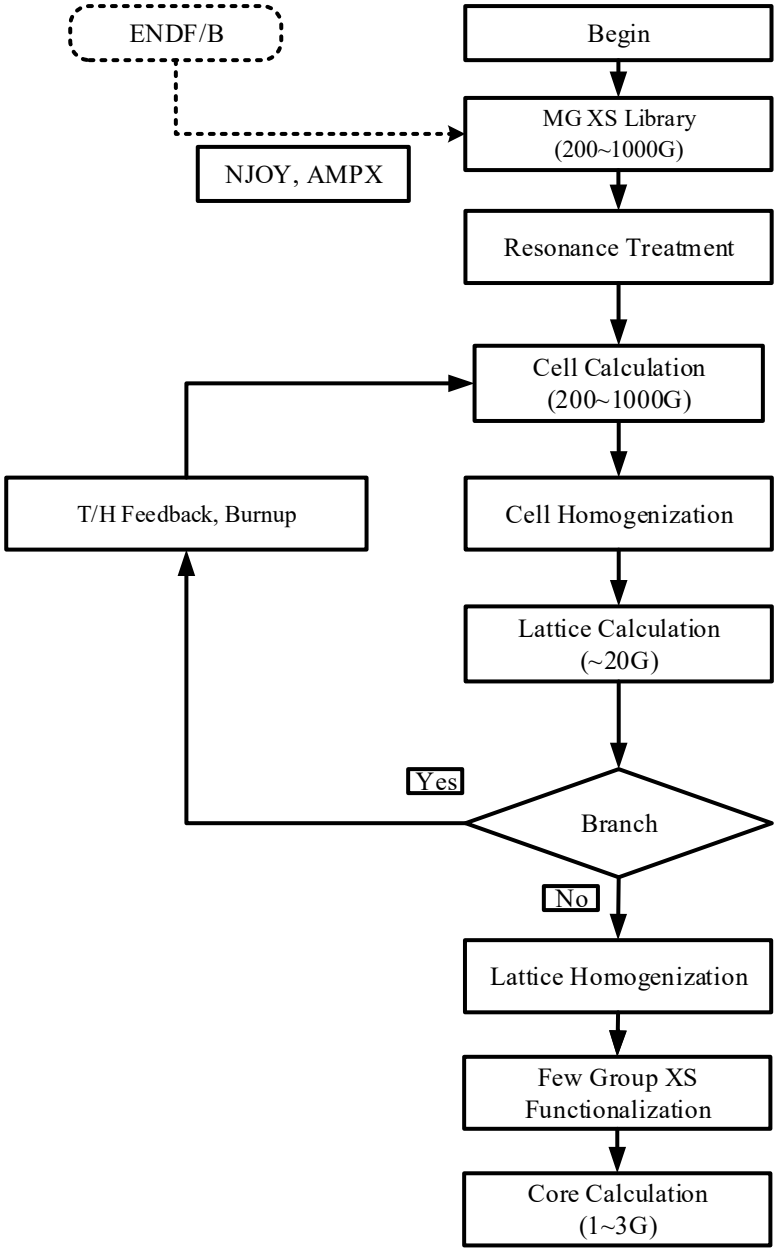

Figure 2.3 Conventional multistep cross section generation procedure for LWR analysis

However, the leakage model lacks a theoretical basis for fuel at the vicinity of strong absorbers that cause strong local depressions on the flux profile, or for the area where the spatial transition effect is dominant. For example, Figure 2.4 shows various UFG flux spectrum for sodium-cooled fast reactor (SFR) MONJU in Japan. Here, the "infinite" and "fundamental" labels indicate the UFG spectrum without and with buckling search (leakage model) to consider the outward leakage of each region (inner core and blanket). "Inhomogeneous" spectrum is the one with the actual leakage correction from the other regions. As shown in Figure 2.4, the leakage spectrum significantly varies compared to the one from the fundamental mode, when the spatial transition effect is dominant at multiregional problems due to the different compositions. Because the leakage model in the radial blanket does not account for an actual neutron behavior in the core, the spatial group condensation (condensation using the spatial flux distribution) is as important as in the local group condensation (condensation using the local slowing down spectrum) process. Additionally, due to the large leakage and hardened spectrum, the anisotropy effect of elastic and inelastic scattering becomes more important, which is treated approximately in the process. It is also reported that the global heterogeneity effects have a non-negligible impact on the UO_2-MOX interface of LWR [32].

For these reasons, special techniques are required in the group condensation process over a large volume for the leakage and anisotropic scattering treatment. In the current sequential condensation scheme, the group condensation of the local heterogeneous problem is performed in very fine group first and the spatial condensation over pins or assemblies is performed later in a coarse group. This may not be valid for the leakage dominant problem. To take the spatial transition effect into account, MC^2-3 performs the UFG slowing down calculation for mixture or the CPM calculation for 1D geometries with transport corrected XSs to represent each assembly,

and then whole core calculation in UFG or IG level is performed using the TWODANT code [33]. Coupling with the TWODANT code provides the accurate modeling of fuel and non-fuel spatial transition effect and anisotropic scattering effect on the weighting spectrum estimation for condensation. Figure 2.5 shows this MC^2-3 procedure for the fast reactor analysis. Again, this scheme, however, also loses its generality by using a rather simple method to treat local heterogeneity effects. With all these reasons, this dissertation suggests more general condensation method than the current multistep approach.

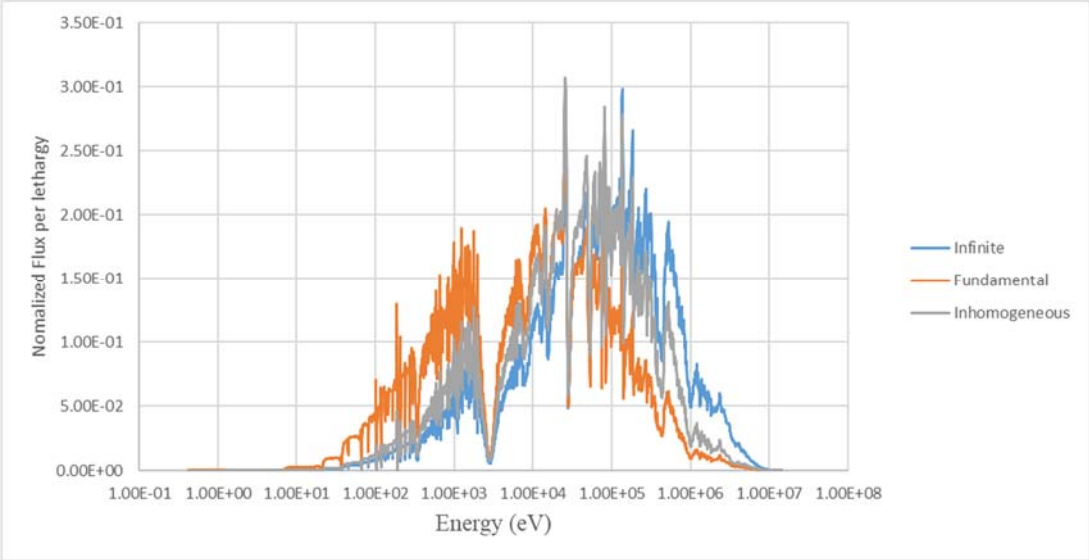

Figure 2.4 Comparison of UFG infinite, fundamental and inhomogeneous spectrum of the radial blanket for sodium-cooled reactor

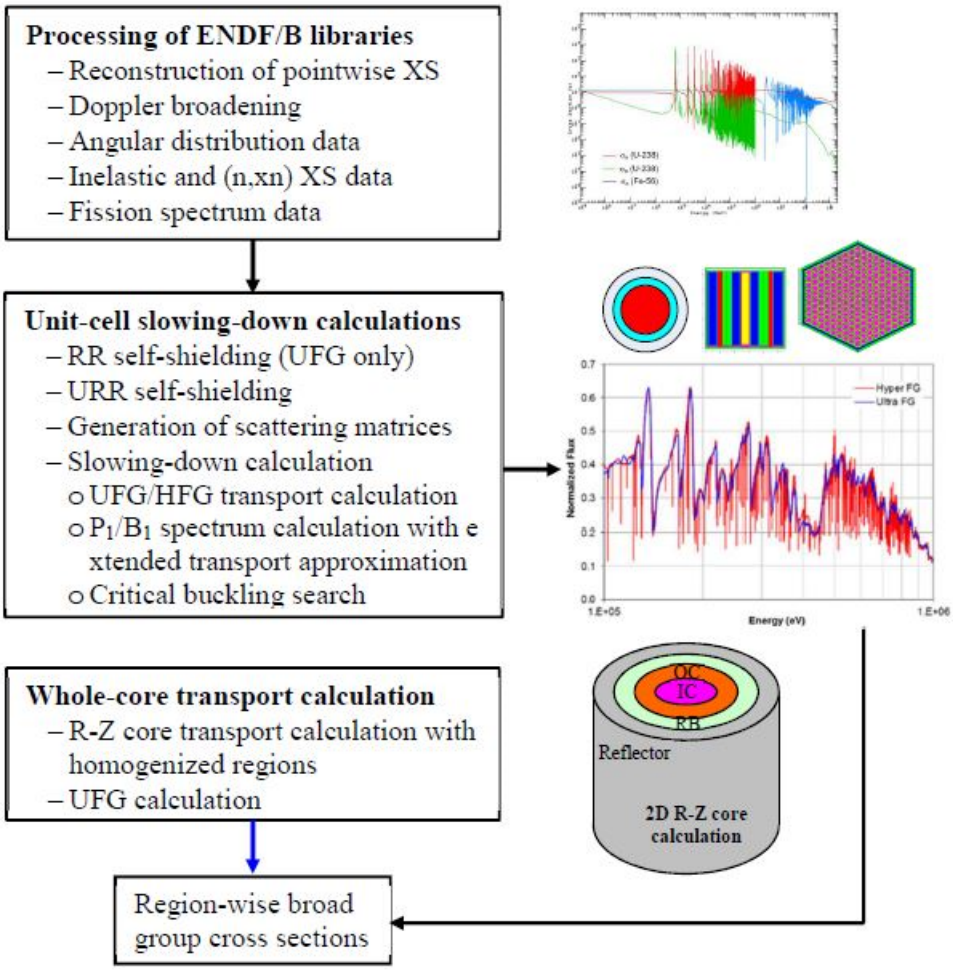

Figure 2.5 Multigroup cross section generation procedure of MC^2-3 for fast reactor analysis taken from NERS 590 Lecture note [34]

2.2.2 Previous research on spatial self-shielding correction

While no approach has been proposed to address the limitation of the current sequential condensation scheme in the XS generation procedure, there exist several theoretical models with different benefits and detriments to account for the spatial effect in the XS homogenization procedure. The spatial self-shielding effect is a problematic issue in the XS homogenization area for the use in low-order calculation, as well as in the weighting spectrum calculation of the XS generation procedure. To develop a new method that can properly accounts for the local

heterogeneity, leakage and anisotropic scattering effects, the generalized condensation scheme was developed on top of the existing spatial homogenization methods. This subsection described the spatial homogenization methods most widely used in the recent neutronic simulations.

Typically, 1D or 2D heterogeneous higher-order simulations are used in local pin cell calculation since they make few approximations despite the significant computational time, whereas the low-order methods, such as a diffusion method, are used for the homogenized lattice calculation. It is feasible to establish a consistent lower order formulation if the pin cell or assembly can be homogenized consistently in the solution process, preserving the averaged characteristics of the heterogeneous solution. This reduced lower order formulation is significantly easier to solve, and its solution, like the CMFD formulation in many transport computations [35], may be utilized to accelerate the original higher order solution. Recently, a mix of local and global higher-order transport calculations have been commonly employed to consider both local heterogeneity and global spatial transition effects as computational power increases.

To generate the homogenized XS by considering the spatial transition effect, the most delicate part is to define a Reference Homogenization Problem (RHP) [36]. RHP typically corresponds to an assembly calculation, whose solution is used as weighting function for cross-section homogenization. In terms of averaged attributes, the homogenized problem has the same outcome as the original heterogeneous problem when the weighting function is determined from the whole problem domain. When applying, however, these variables must be determined prior to each archetypal portion (RHP) of the whole geometry. For this reason, there always exist errors associated with homogenization. The success of the homogenized XS generation depends on how the solution of the RHP must then be representative of the actual core conditions to minimize the

error. As an effort to remove the errors associated with the homogenization and the difference between RHP and the real core, diverse approaches have been proposed.

The most widely used approach in the XS homogenization field is the adjustment factor method, known as the flux discontinuity factor [37], assembly discontinuity factor [38], or the super-homogenization (SPH) factor [39] to correct the homogenized XS error by multiplying correction factors directly. These adjustment factors are to preserve the reaction rates between the RHP calculation and the MG XS generation calculations as well as the interface currents. Once RHP is defined, the adjustment factors are generated using the iterative procedure of the main transport calculation and balance relationship for each equivalent region and group in conjunction with the leakage model [40]. While the RHP with the adjustment factor provides the reasonable solutions for fuel assemblies, it raises a question of how to define an adequate RHP for reflector or absorber assembly homogenization. A reflector requires a different homogenization approach as no fission occurs, and a vacuum boundary condition is imposed on at least one boundary. Many studies have been performed to improve and extend the adjustment factors for numerous scenarios with different assembly configurations and boundary conditions.

One of the most straightforward approaches is the use of a larger spatial domain for the homogenization of XSs by directly modeling a subset (supercell) of a fuel pin cell at the assembly level [41]. While the single reference pin cell with the leakage model has difficulties in treating problems with substantial flux gradients next to an absorber assembly or outer boundary, the supercell RHP aims to capture the environmental impacts on peripheral cells or assemblies by explicitly simulating the surrounding geometry. This partial solution enables the production of more precise correction factors, as evidenced by several studies demonstrating its successful use for the LWR, as well as partially successful for VHTR and TREAT [42]. Using higher-order

transport solvers and supercell or multi assembly [43,44], work has recently been done to develop new concepts of correction factor for fast reactor analysis.

Although these adjustments have been effectively applied to certain reactor evaluations, they are difficult to apply to other applications as these adjustment variables are problem dependent with a certain leakage model or RHP. In a leaky core, for example, using a single set of correction factors leads to substantial errors owing to strong spectral coupling effects over the whole core. While differences in assembly configuration are not significant in PWRs, the long mean free path of neutron in fast reactors may limit the adoption of traditional correction factor procedures. Moreover, it is reported that the SPH method can have an infinite number of the SPH factor sets depending on its normalization and boundary conditions [40]. Even if the supercell technique mitigated this problem, it would be impossible to calculate the supercell for each heterogeneous pin anytime the surrounding configuration changes. Thus, it is unclear if a generalizable scheme based upon the traditional methods can be established for advanced reactor analysis.

There are different approaches which utilize the iterative assembly homogenization technique, referred as the dynamic homogenization method [45]. To do this, each kind of assembly is homogenized using a fine MG transport computation with an enforced eigenvalue and currents that take into account the real macroscopic core exchanges across assemblies. Fine MG interface angular fluxes entering an assembly are obtained from fine multigroup angular fluxes exiting neighboring assemblies properly normalized to preserve core macro group currents [36]. The approach corrects the bias caused by the infinite lattice computations and leakage model assumption, resulting in fine multigroup assembly. Assembly homogenization process is done iteratively alongside the external core eigenvalue iterations to update the core eigenvalue and

interface currents. This distinguishes the iterative method from other correction approaches, which relies on the leakage model or the tabulation of precalculated adjustment factors. This requires the multiple homogenization and transport calculations iteratively to converge the solution which is time-consuming to be used in the XS weighting spectrum calculation.

Recently, the spatial rehomogenization method [46] was proposed to correct nodal XSs. Later, this method was extended to the spectral homogenization part, in which the environmental spectrum in each group g can be written as [32]

$$\phi_{\mathrm{env,g}}(u) = \bar{\Phi}_g \phi_{\infty,g}(u) + \delta\phi_g(u) \tag{2.15}$$

where the subscript ∞ denotes the reference unity quantity obtained from the infinite lattice condition, and δ indicates variations in the real environment. $\bar{\Phi}$ is the group averaged flux. The environmental spectrum is formulated as the sum of two terms. $\delta\phi_g(u)$ was determined by a modal-expansion approach [32], by solving the transport equation using a homogenized node. The environmental spectrum is recreated using the results of the nodal and lattice calculations, and the rehomogenization method reflects the spectral effects on the homogenized nodal XSs. While this technique presents a unique mathematical definition of homogeneity defects [47], this method does not explain the anisotropic scattering effect on the global leakage since the procedure is confined to the nodal diffusion calculation. Moreover, a combined spatial and spectral effects was not considered.

2.2.3 generalized condensation scheme

Upon the progress made in this area, a new generalized group condensation scheme is proposed to accelerate the UFG slowing down calculation without losing its accuracy on weighting spectrum estimation. Since the condensation procedure also requires the weighting spectrum

which properly represents the local and global flux distributions, the new method was developed by combing the idea of above dynamic homogenization and rehomogenization methods. The new method quantifies several approximation effects in a separate term (from the rehomogenization method) in a single condensation step by combining the multiple transport solutions (from the dynamic homogenization method) with different problem domain and calculation options. While in prior techniques, the only environmental spectrum played a role as a correction in heterogeneous flux and nodal XS, the new method aims to represent all energy and spatial self-shielding effects, anisotropic scattering, and assembly heterogeneity concurrently. Because sequential multistep approaches suffer from approximations used to treat neutron leakage and spatial heterogeneities such as neutron reflectors, this method aims to build on previous work by investigating the possibility of directly computing the UFG weighting spectrum, which accounts for self-shielding effects in a fine spatial mesh. In the generalized scheme, the weighting spectrum in Eq. (1.10) is redefined with the general concept of infinite pin cell/lattice solution (ψ_{lk}^{local}) and the environmental effect (ψ_{lk}^{env}) from the rehomogenization method as

$$\psi_{lk}^{w}(r,\mathrm{E}) \;\cong\; \mathrm{C}\cdot\psi_{lk}^{\text{local}}(r,E)+(1-\mathrm{C})\cdot\psi_{lk}^{\text{env}}(r,E)+\delta\psi_{lk}^{\text{cross}}(r,E) \tag{2.16}$$

Since the local and global solutions cannot be decoupled from the real heterogeneous solution, $\delta\psi_{lk}^{\text{cross}}$ represents the contributions of mixed local and leakage term. Here, *C* is the normalization coefficient to minimize the weighting spectrum reconstruction error. Again, because we do not know the actual heterogeneous solution, it is important to choose the appropriate RHP to determine $\delta\psi_{lk}^{\text{cross}}$ and the weighting coefficient *C*. Based on the discussion that the leakage rate in a fuel assembly is dominated by scattering anisotropy and inter cell neutron exchange [31], three RHPs were selected: 1) 2D local pin cell with low-order anisotropic scattering, 2) 2D assembly geometry with homogenized pin cells and higher order anisotropic scattering treatment and 3) mixture in an

infinite medium, instead of the real solution, as a measure of aptness of the two RHPs. Since the first RHP calculation solve the 2D pin cell problem with the explicit modeling and the transport corrected XSs (TCP0), this offers the local heterogeneity effect, compared to the third mixture calculation. Similarly, the second RHP solves the assembly problem with the higher-order anisotropic scattering treatment, this measures the spatial transition as well as the anisotropic scattering effect on leakage. Then, the weighting spectrum is approximated as a linear combination of pin and assembly spectrum and the weighting factor is determined from the reactivity contribution discussed in the next section. Based on the experience in this work, we hypothesize that the adaptation of pin-homogenized assembly solution, instead of the local leakage term, diminishes the severity of the error introduced by approximation of inherent local-global flux non-separability as the pin-homogenization was performed using the first RHP solution. Thus, it is acceptable to ignore the weighting spectrum reconstruction error of Eq. (2.16). The reconstructed flux spectrum should preserve the reaction rate from the heterogeneous 2D problem over the same domain to satisfy reaction rate conservation. Typically, a standard scalar flux is used in the group condensation because it preserves the reaction rates. Above hypothesis results in the following MG formulation for the weighting spectrum reconstruction:

$$\psi_{0,g}^{w}(r) \cong \mathrm{C}\cdot\psi_{\mathrm{TCP0,\,g}}^{\mathrm{het}}(r)+(1-\mathrm{C})\cdot\psi_{\mathrm{P_N},g}^{\mathrm{hom}}(r) \tag{2.17}$$

The higher flux moments can be directly obtained from the second RHP calculation with C=0.

2.2.4 Reaction rate analysis and the determination of coefficients

The generalized condensation procedure in Eq. (2.17) needs the coefficients to determine the ratio of multiple transport solutions. A more detailed analysis is required to quantitatively evaluate the contribution of each calculation. To determine the coefficient for the scalar flux reconstruction among multiple reaction rates of many nuclides, absorption and production reaction rate

differences are converted to the degree of error contribution of the observed reactivity difference between the target and mixture calculations results. Here, target calculation indicates either the first or second RHP calculation. In the generalized condensation scheme, the absorption and fission reactivity differences deduced from reaction rates difference indicate the magnitude of the physic effects between two RHP calculations. The reaction rate difference between the target and mixture calculations and its contribution to the reactivity difference were estimated for each nuclide and energy group as follows:

1) Perform the mixture calculation and get the MG scalar fluxes, isotopic capture and fission reaction rates, and average number of neutrons released per fission (υ) in addition to eigenvalue. Note that the capture notation here includes all neutron disappearance reactions, like (n,p) reaction in high energy groups.
2) Perform the target calculation to obtain the parameters at the step 1).
3) Calculate the contribution to the reactivity difference of the reaction rate difference (i.e., XS and flux errors) for each nuclide, reaction type, and energy group using the following formula and scalar flux ϕ:

$$\Delta\rho_{c,g',i'}^{k'} = \frac{N_{i'}^{k'}(\sigma_{c,g',i'}^{k'}\phi_{g',i'} - \hat{\sigma}_{c,g',i'}^{k'}\hat{\phi}_{g',i'})V_{i'}}{\sum_i\sum_k\sum_g N_i^k \upsilon_{g,i}^k \sigma_{fis,g,i}^k \phi_{g,i} V_i} \tag{2.18}$$

$$\begin{aligned}\Delta\rho_{fis,g',i'}^{k'} = \frac{1}{k_\infty} &- \frac{\sum_i\sum_k\sum_g N_i^k(\sigma_{a,g,i}^k - \sigma_{\mathrm{n,2n},g,i}^k - 2\sigma_{\mathrm{n,3n},g,i}^k)\phi_{g,i}V_i}{\sum_i\sum_k\sum_g N_i^k \upsilon_{g,i}^k \sigma_{fis,g,i}^k \phi_{g,i} V_i - N_{i'}^{k'}\upsilon_{g',i'}^{k'}(\sigma_{fis,g',i'}^{k'}\phi_{g',i'} - \hat{\sigma}_{fis,g',i'}^{k'}\hat{\phi}_{g',i'})V_{i'}} \\ &+ \frac{N_{i'}^{k'}\upsilon_{g',i'}^{k'}(\sigma_{fis,g',i'}^{k'}\phi_{g',i'} - \hat{\sigma}_{fis,g',i'}^{k'}\hat{\phi}_{g',i'})V_{i'}}{\sum_i\sum_k\sum_g N_i^k \upsilon_{g,i}^k \sigma_{fis,g,i}^k \phi_{g,i} V_i - N_{i'}^{k'}\upsilon_{g',i'}^{k'}(\sigma_{fis,g',i'}^{k'}\phi_{g',i'} - \hat{\sigma}_{fis,g',i'}^{k'}\hat{\phi}_{g',i'})V_{i'}}\end{aligned} \tag{2.19}$$

where $\Delta\rho_{x',g',i'}^{k'}$ is the reactivity differences due to the difference in the fission or absorption reaction rate of nuclide k' at group g', and region i'. N_i^k and V_i are the atomic number

density of nuclide k and volume at region i, respectively. A quantity with caret (^) symbol indicates the XS or flux from the target calculation, while the other quantities are from the reference calculation. Multiplication factor (k_∞) in Eq. (2.19) can be estimated by using the following equation:

$$k_\infty = \frac{\sum_i \sum_k \sum_g N_i^k \upsilon_{g,i}^k \sigma_{fis,g,i}^k \phi_{g,i} V_i}{\sum_i \sum_k \sum_g N_i^k (\sigma_{a,g,i}^k - \sigma_{\mathrm{n,2n},g,i}^k - 2\sigma_{\mathrm{n,3n},g,i}^k)\phi_{g,i} V_i} \tag{2.20}$$

4) The direct effects of XS errors (i.e., without considering the flux errors resulting from XS errors) were also investigated using the reference flux in Eqs. (2.18) and (2.19) as

$$\Delta\rho_{c,g',i'}^{k'} = \frac{N_{i'}^{k'} (\sigma_{c,g',i'}^{k'} \phi_{g',i'} - \hat{\sigma}_{c,g',i'}^{k'} \phi_{g',i'}) V_{i'}}{\sum_i \sum_k \sum_g N_i^k \upsilon_{g,i}^k \sigma_{fis,g,i}^k \phi_{g,i} V_i} \tag{2.21}$$

$$\begin{aligned} \Delta\rho_{fis,g',i'}^{k'} = \frac{1}{k_\infty} &- \frac{\sum_i \sum_k \sum_g N_i^k (\sigma_{a,g,i}^k - \sigma_{\mathrm{n,2n},g,i}^k - 2\sigma_{\mathrm{n,3n},g,i}^k)\phi_{g,i} V_i}{\sum_i \sum_k \sum_g N_i^k \upsilon_{g,i}^k \sigma_{fis,g,i}^k \phi_{g,i} V_i - N_{i'}^{k'} \upsilon_{g',i'}^{k'} (\sigma_{fis,g',i'}^{k'} \phi_{g',i'} - \hat{\sigma}_{fis,g',i'}^{k'} \phi_{g',i'}) V_{i'}} \\ &+ \frac{N_{i'}^{k'} \upsilon_{g',i'}^{k'} (\sigma_{fis,g',i'}^{k'} \phi_{g',i'} - \hat{\sigma}_{fis,g',i'}^{k'} \phi_{g',i'}) V_{i'}}{\sum_i \sum_k \sum_g N_i^k \upsilon_{g,i}^k \sigma_{fis,g,i}^k \phi_{g,i} V_i - N_{i'}^{k'} \upsilon_{g',i'}^{k'} (\sigma_{fis,g',i'}^{k'} \phi_{g',i'} - \hat{\sigma}_{fis,g',i'}^{k'} \phi_{g',i'}) V_{i'}} \end{aligned} \tag{2.22}$$

For example, $\Delta\rho_{fis,g,i}^k$ obtained from the first (2D UFG pin cell calculation) and third RHP calculations (0D UFG mixture slowing down) provides the magnitude of local heterogeneity effect and the transport correction (TCP0) in fission reaction rate of nuclide k at group g, and region i. Similarly, $\Delta\rho_{fis,g,i}^k$ obtained from the second (2D UFG pin-homogenized assembly calculation) and third RHP calculations represents the spectral transition effect between neighboring pins and higher order anisotropic scattering effect. Then, the MG reactivity contribution, τ_g, in each RHP calculation can be obtained as the sum of the absolute reactivity differences to avoid an unexpected error cancellation between reactions, nuclides and regions, which is defined as

$$\tau_{\mathrm{g}} = \sum_{x} \sum_{i} \sum_{k} \left| \Delta \rho_{x,g,i}^{k} \right| \tag{2.23}$$

The term $\tau_{\mathrm{g}}^{\mathrm{local}}$ is defined as the sum of the absolute reactivity differences between the first and third calculation which represents the absolute magnitude of local heterogeneity effect in group g and $\tau_{\mathrm{g}}^{\mathrm{global}}$ represents the global spatial transition effect and higher order anisotropic scattering effect in group g. Smaller $1/\tau_{\mathrm{g}}$ demonstrates that the corresponding solution has higher impact on the real solution. Inverse distance weighting [48] is the simplest spatial interpolation method that assumes each input point having a local influence that diminishes with distance:

$$u(x) = \frac{\sum_{i} w_i(x) u_i}{\sum_{i} w_i(x)} \tag{2.24}$$

$$w_i(x) = \frac{1}{d(x, x_i)^p} \tag{2.25}$$

where u_i is the i-th sample input, x_i is the interpolated point and d is a given distance. The weights in Eq. (2.25) are a decreasing function of distance. Therefore, the coefficients in Eq. (2.17) are determined using the inverse distance weighting interpolation as

$$\tilde{\phi}_{g}^{\mathrm{het}} = \frac{\tau_{\mathrm{g}}^{\mathrm{global}}}{\tau_{\mathrm{g}}^{\mathrm{local}} + \tau_{g}^{\mathrm{global}}} \phi_{\mathrm{global,g}}^{\mathrm{hom}} + \frac{\tau_{\mathrm{g}}^{\mathrm{local}}}{\tau_{\mathrm{g}}^{\mathrm{local}} + \tau_{\mathrm{g}}^{\mathrm{global}}} \phi_{\mathrm{local,g}}^{\mathrm{het}} \tag{2.26}$$

The first and second RHP calculations were performed using the 2D MOC solver in MC^2-3 and external DIF3D/VARIANT [49] solvers, respectively. It should be noted that the UFG XSs set for the second RHP calculation are spatially homogenized using the first RHP solution to isolate the spectral transition and anisotropic effects. Obtained reconstructed flux spectrum is used to generate the IG XSs, then the IG lattice calculation are performed to generate the final BG XSs. Figure 2.8

shows this MG XS section generation procedure of MC^2-3 with the extened thermal capability, the UFG/HFG iteration and the generalized condensation scheme.

To examine the validity of the generalized condensation scheme, a simple 3 by 3 LWR pin-cell problem is solved using a typical 6.5 wt.% UO_2 fuel with minor simplifications. A large water hole is located at the center to investigate the environmental effect in the weighting spectrum. Figure 2.6 shows the configuration of the 3 by 3 LWR pin-cell problem. Figure 2.7 illustrates the flux solutions of three RHP calculations and the one of reference heterogeneous UFG calculation. Due to the presence of large waterhole, the pin cell solution has a noticeable deviation at the thermal peak point, compared to the reference solution. Pin-homogenized assembly solution can catch the environmental effect relatively well compared to the pin cell solution. The coefficient *C* in the figure demonstrates the flux weighting ratio between two RHP solutions. As shown in the figure, the assembly solutions are more weighted than the pin cell solution with the smaller *C* value at the thermal and high energy range, whereas the two solutions have similar importance (~0.5) in the epithermal energy range. For the resolved and unresolved resonances, it can be clearly seen from the figure that the coefficient becomes larger, which indicates the higher importance of the local solution. As a result, the reconstructed flux spectrum provides more realistic spectrum, compared to the pin cell solution. Although there are remaining differences in the reconstructed UFG flux solution, these differences in the UFG level result in rather smaller errors in the IG XSs. The subsequent IG heterogeneous lattice calculation further eliminates the remaining discrepancies in the IG weighting spectrum. This comparison demonstrates that the generalized condensation scheme provides an accurate estimate, or at least a partial resolution of the spectral bias between the weighting spectrum and real solution, with the significant improvement of computing time in the IG lattice calculation.

Figure 2.8 presents the overall computational flow of the generalized MG XS section generation procedure of the modified MC^2-3. As described in the Section 2.1.3, for the calculation of thermal spectrum, the 2D MOC transport solver as well as the homogeneous and 1D CPM solvers have been extended to comply with the thermal XS library and to perform the upscattering iterations in the thermal energy range. The Gauss-Seidel method is used for the upscattering iteration. After the mixture UFG calculation with the HFG iteration, the first RHP calculation is performed with the self-shielded UFG XSs. The reactivity differences due to the local heterogeneity effect are estimated after the first calculation. The UFG XSs are spatially homogenized over each pin for the second and third RHP calculations. Then, the reactivity differences due to the spatial transition and anisotropic scattering effects are estimated using the two calculation results. The reconstructed fluxes are determined using Eq. (2.26) and the UFG XSs are collapsed into the IG XSs using the reconstructed fluxes for the next heterogenous assembly calculation.

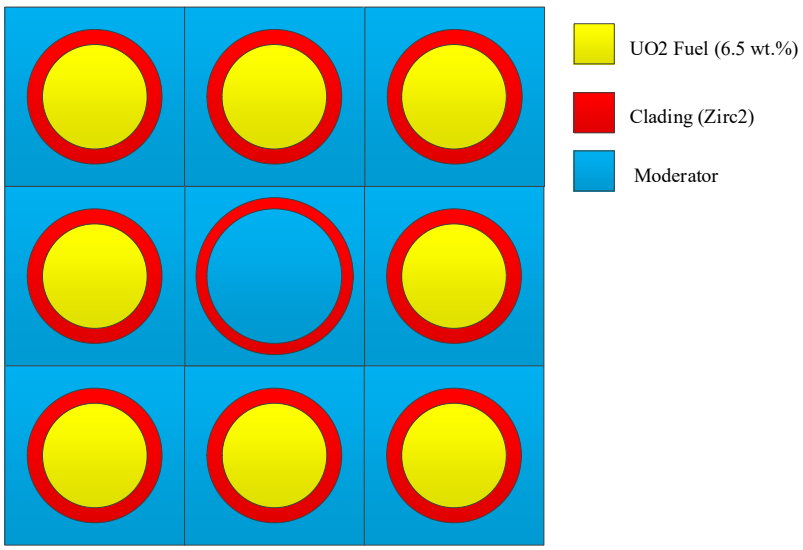

Figure 2.6 Configuration of the 3 by 3 LWR pin-cell problem

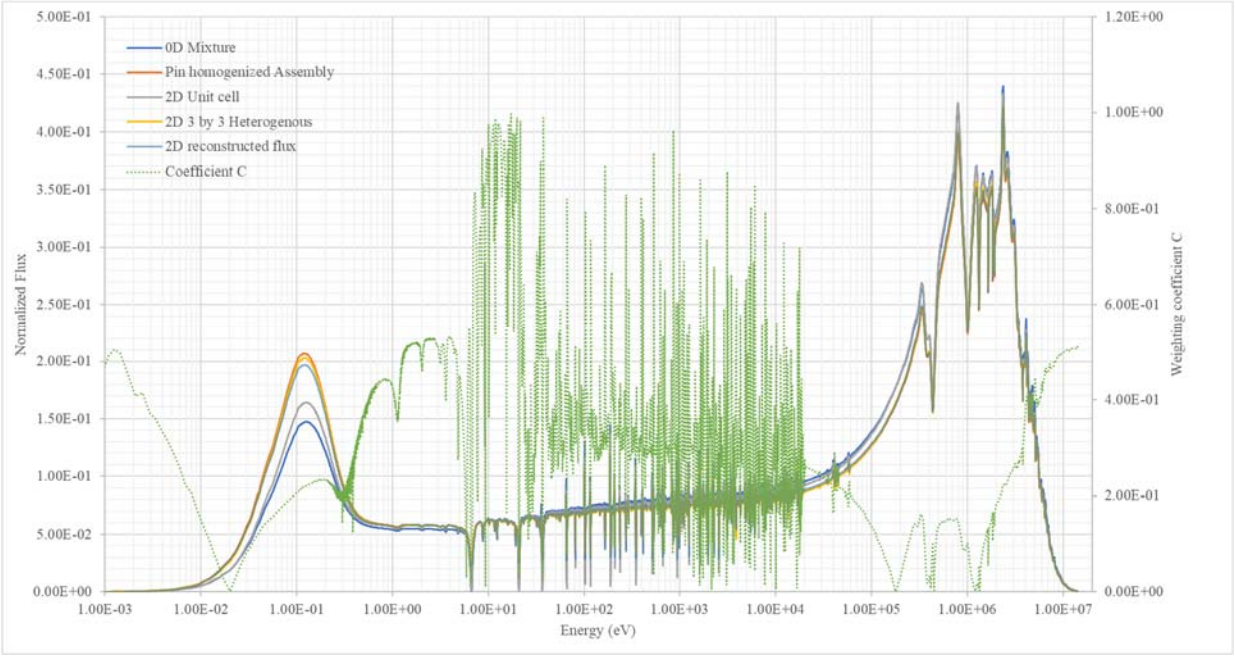

Figure 2.7 Comaprison of three RHP, reconstructed and refenrence flux distributions (left-axis) and the obtained coefficients (right-axis) using the generalized condensation scheme

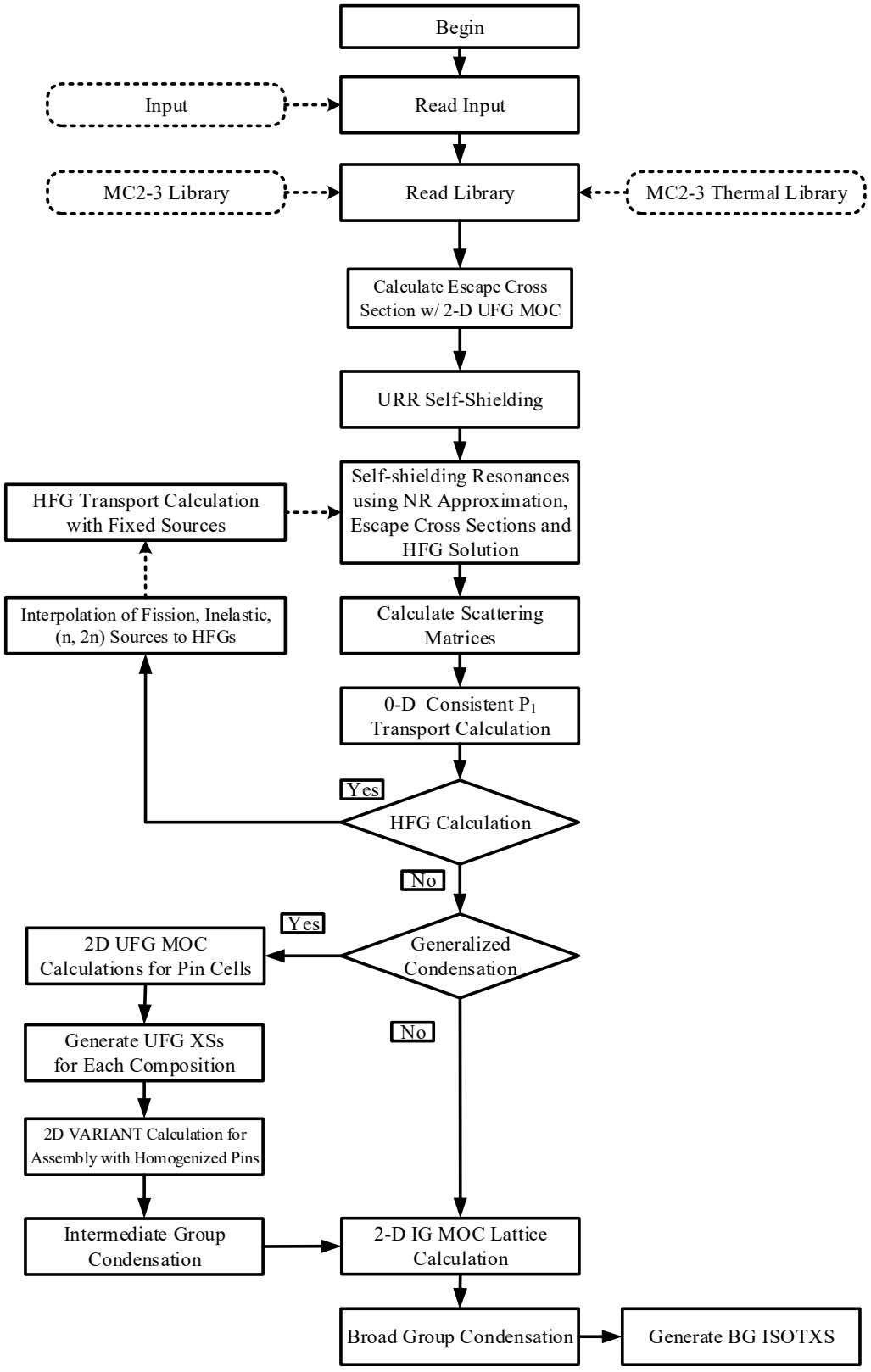

Figure 2.8 Generalized MG XS section generation procedure of MC^2-3

2.3 Numerical Tests with New Cross Section Generation Procedure

2.3.1 Pin cell benchmark results

As an initial verification test of the detailed slowing down capability of MC^2-3, ten benchmark problems representing various conventional and advanced reactors were solved, including a PWR UO_2 fuel pin with four different temperatures in hot zero power (HZP) condition at the beginning of cycle (BOC) of the VERA benchmark problems, a typical BWR UO_2 fuel pin with three different void fractions, a simplified advanced burner test reactor (ABTR) fuel pin, a high temperature gas-cooled reactors (HTGR) homogenized fuel compact and a homogenized molten salt reactor (MSR) fuel. Table 2.1 provides the brief description of benchmark problems and the isotopic compositions of the problems are shown Table 2.2. More detailed information can be found in [50] for the PWR and in [51] for the BWR problems, in [52] for ABTR, and in [53] for MSR. For homogenized HTGR, a simplified fuel compact problem was developed based on the TRISO particle data of the NGNP design [54] that uses 10.36 wt.% UCO fuel with 37.8% packing fraction. The TRISO particles are simply volume-averaged with a graphite matrix to form the homogenized fuel compact. In Chapter 4, we show how to tackle this problem using the double heterogeneity capability. All the benchmark problems were simulated using a square pin cell geometry of MCNP6. Each MCNP simulation was performed with 1,000 active cycles and 100,000 histories per cycle. It should be noted that the HTGR problem was calculated by Serpent-2. The Serpent-2 calculation option is the same as the one of MCNP calculation. The 2D MOC calculation in MC^2-3 was performed with a ray spacing of 0.05 cm, 16 azimuthal angles, 4 polar angles (for π) and P_2 anisotropic scattering treatment.

Table 2.1 Pin cell benchmark problems

Fuel	Case	^{235}U w/o	Temperature (K)			Remark
			Fuel	Clad	Moderator	
PWR	P1	3.1	565	565	565	VERA P1A
	P2		600	600	600	VERA P1B
	P3		900	600	600	VERA P1C
	P4		1200	600	600	VERA P1D
BWR	B1	6.5	900	600	600	Void fraction (40%)
	B2		900	600	600	Void fraction (70%)
	B3		900	600	600	Void fraction (90%)
ABTR	A1	-	300	300	300	Cylindrical geometry
HTGR	H1	-	300	300	300	Homogenized compact
MSR	M1	-	300	300	300	Homogenized cylinder

Table 2.2 Isotopic composition for ABTR, HTGR and MSR

ABTR			Homogenized HTGR			Homogenized MSR	
Region	Nuclide	Number density	Region	Nuclide	Number density	Nuclide	Number density
Fuel	^{235}U	3.2247E-05	Fuel	^{235}U	8.7900E-05	^{235}U	3.1000E-05
	^{238}U	2.0222E-02		^{238}U	7.5100E-04	^{238}U	4.2750E-03
	^{239}Pu	3.4991E-03		^{16}O	1.2600E-03	^{239}Pu	4.0400E-04
	^{240}Pu	3.7398E-04		C-nat	6.2100E-02	^{240}Pu	5.4000E-05
	^{90}Zr	3.7526E-03	He	^{4}He	4.4800E-04	^{241}Pu	2.7000E-05
Bond	^{23}Na	2.2272E-02	Matrix	C-nat	8.7300E-02	^{242}Pu	5.4000E-05
Cladding	^{54}Fe	4.0824E-03				^{23}Na	5.3830E-03
	^{56}Fe	6.4085E-02				^{35}Cl	1.5010E-02
Coolant	^{23}Na	2.2272E-02					

The benchmark results in Table 2.3 show that the MC^2-3 multiplication factors obtained with the 3,483 UFG group library are generally consistent with the MCNP results. The maximum difference in reactivity between MCNP6 and MC^2-3 results is -132 pcm for BWR with zero void fraction. There remains a possibility that the good multiplication factor results might be due to error cancellations, and accordingly more detailed analysis is needed to quantitatively evaluate the quality of the MG XSs. As introduced in the section 2.2.2, the reaction rate analysis is useful to identify the main error sources and the degree of error cancellation of the observed eigenvalue

difference between two calculations. By replacing the target and the mixture calculations in Eqs. (2.18) through (2.22) with the MG deterministic and the CE MC calculations respectively, the reaction rate analysis can be used for the MG XS verification against the reference MC solution.

Table 2.3 Comparison of eigenvalue for various pin cell problems

Case	MCNP	MC^2-3	$\Delta\rho$ (pcm)
P1	1.18655 (6)	1.18551	-74
P2	1.18184 (6)	1.18041	-103
P3	1.17170 (6)	1.17018	-111
P4	1.16327 (6)	1.16156	-127
B1	1.39488 (6)	1.39232	-132
B2	1.32518 (6)	1.32351	-95
B3	1.24258 (6)	1.24462	-131
A1	1.60150 (4)	1.60042	-42
H1[a)]	1.31602 (7)	1.13412	110
M1	1.13923 (1)	1.13945	17
a) calculated by Serpent-2			

Since the accuracy of MC^2-3 were already verified against many fast reactor benchmark results, Table 2.4 provides the reaction rate analysis results only for three thermal reactor cases: P2, B3 and H1. Resulting spectra of three cases are presented in Figure 2.9. It is noted that the typical PWR spectrum; (thermal peak, the asymptotic 1/E spectrum and fission spectrum) is not attained in the highly voided cases B3 and H1. The values in the column "Code" represent the reactivity difference and its standard deviation determined from the eigenvalue results of MC^2-3 and MCNP The column "RR" indicates the reactivity difference determined from two eigenvalues deduced from reaction rates using Eq. (2.20). RR_{cap} and RR_{fis} give the reactivity differences due to the capture and fission XS differences and the flux differences obtained using Eqs. (2.18) and (2.19). As shown in the table, the reactivity deviations of MC^2-3 from MCNP for the PWR pin cell problem, P2, are mostly resulted from the errors in ^{235}U capture and fission and ^{238}U capture

reaction rates. The effects on reactivity of the capture and fission reaction rates of ^{235}U have opposite signs, and thus they are partly cancelled out. The 90% voided BWR case shows a similar trend, but the net effect of ^{235}U fission and ^{238}U capture reactions becomes larger than the one of PWR due to hardened spectrum. In the HTGR result, there are less error cancellations between the ^{238}U capture and ^{235}U fission reactions. Since it is still possible that the good agreements of isotopic reactivity bias are caused by error cancellation among energy groups, the group-wise differences of reaction rates were also examined in Figure 2.10 to Figure 2.15. All figures have three graphs: relative XS errors, the reactivity differences due to the differences in XS and flux and the reactivity differences due to the XS difference only. The second graph differs greatly from the third figures when the scattering matrices as well as principal XSs are error sources of reactivity. Figures show that only a few groups have the XS errors larger than 5%. Note that sharp peaks of ^{238}U XS errors around 20 keV are due to the inconsistency of self-shielding method between unresolved and resolved resonance energy ranges at the boundary. These errors do not degrade the overall calculation results as shown in the middle and bottom figures, which indicate the reactivity differences due to the XS difference. It is confirmed that those errors are less than 1% in the BGs. The reactivity errors due to the XS error are also negligible. The maximum error is 30 pcm of ^{238}U for the H1 case at the vicinity of thermal resonances. The figures clarify that there are no noticeable group-wise errors coming from XS and flux errors larger than 100 pcm in thermal. However, all thermal problems have non-negligible group-wise reactivity errors at the thermal peaks. Comparison between the middle and bottom figures shows that the thermal errors are due to the inaccurate thermal scattering matrix of moderator. Indeed, there is a major assumption that is not fully addressed in the current MG XS generation procedure. That is, it is assumed the temperature independent scattering kernel of light-weight isotopes is used, the current thermal up-scattering

boundary is limited up to 10 eV. It was recently reported that the neglect of temperature dependency of hydrogen scattering kernel even above typical thermal cut-off energy has a significant impact on neutron thermalization [55]. Since the current thermal XS library of MC^2-3 was generated by NJOY using the asymptotic kernel assumption in which the thermal agitation of target nuclides is not considered, this may induce a significant bias in thermal energy range. Thermal scattering XSs are generated using NJOY for energy up to 10 eV by using either the free-gas kernel or the S(α,β) law, depending on the isotope. The THERMR module of NJOY restricts both the source and sink energy bins to 10 eV, therefore up-scattering XSs from energy below 10 eV to energy above 10 eV are disregarded. As a result, scattering transfer XSs with a sink energy greater than 10 eV are normalized in the post-processing code to retain the overall scattering XSs.

As a result, any XS to energy higher than 10 eV is rejected, and the remainder kernel is evenly increased by the discarded probability. However, the effect of the thermal agitation of target nuclides is not negligible even for energy above 10 eV not only for the heavier nuclides, but also for the hydrogen or any light-weight nuclide with the high temperature. Initially, MC^2-3 thermal XSs are developed to consider the thermal up-scattering up to 5eV and recently has been extended up to 10 eV [56]. Table 2.5 shows this up-scattering boundary effect in terms of reactivity difference, which mostly lies on the thermal energy range as shown in Figure 2.10. However, MCNP considers the temperature-dependent scattering kernel with a constant XS approximation up to 400 k_BT by default [57]. This indicates inconsistency between MCNP and MC^2-3, in particular for hydrogen or the intermediate weight isotope with the higher temperature for which 400 k_BT is greater than 10 eV. Therefore, either the fundamental resolution of NJOY or the post processing in MC^2-3 is needed to resolve remaining errors at thermal energy range. Despite of the above up-scattering issue, it can be concluded from the reaction rate analysis results that the MC^2-

3 results are consistent with the MCNP results regardless of its energy spectrum or composition in general. This indicates that the detailed slowing down approach in MC^2-3 provides reasonably good solution for a wide range of reactor problems.

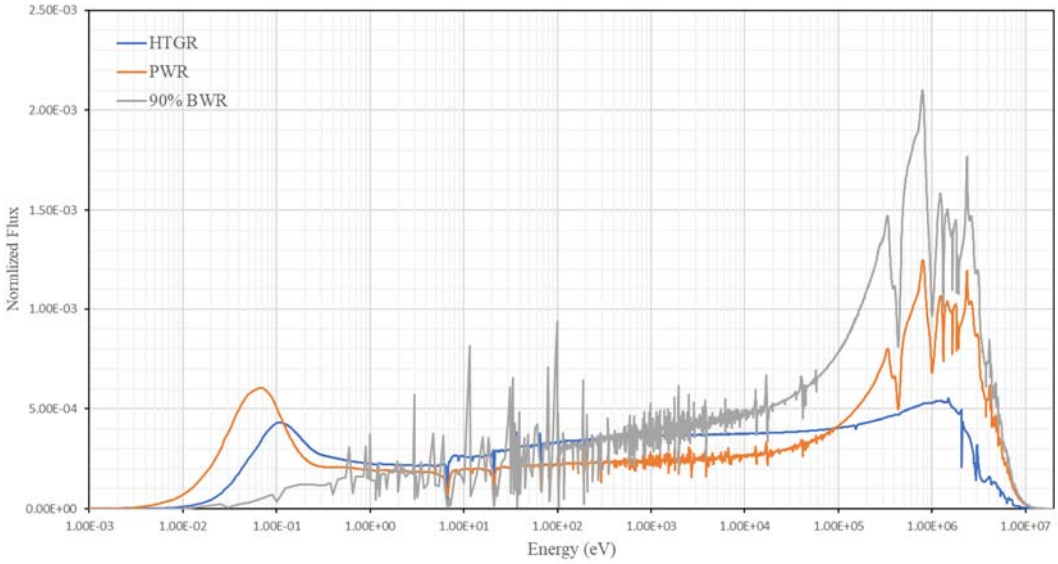

Figure 2.9 Comparison of UFG fluxes for PWR, 90% voided BWR and HTGR

Table 2.4 Reaction rate analysis results for major actinides

Case	$\Delta\rho$ [pcm]		Nuclide	XS/Flux effect [pcm]		
	Code	RR		RR_{cap}	RR_{fis}	SUM
P2	-103	-102	92235	123	-201	-78
			92238	-32	-	-32
B3	-131	-122	92235	72	-220	-147
			92238	-53	73	22
H1	110	108	92235	-52	93	41
			92238	59	-5	54

Table 2.5 Comparison of different thermal up-scattering boundary effect

Case	Thermal up-scattering boundary	Nuclide	XS/Flux effect [pcm]		
			RR_{cap}	RR_{fis}	SUM
P2	5 eV	92235	214	-321	107
		92238	-24	-	-24
	10 eV	92235	123	-201	-78
		92238	-32	-	-32

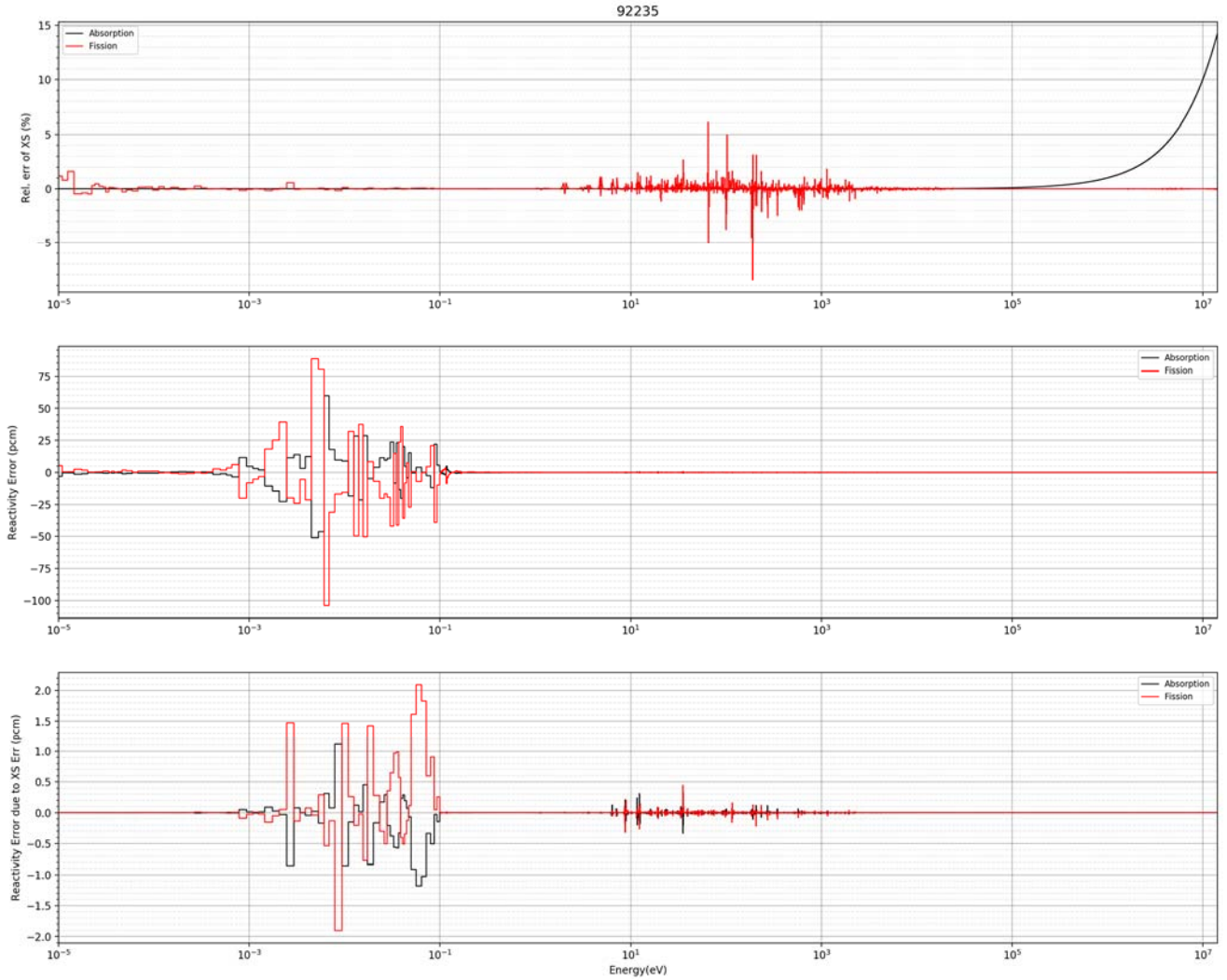

Figure 2.10 Relative cross section error (top), reactivity differences due to the cross section and flux errors (middle) and reactivity differences due to the cross section error (bottom) of ^{235}U for P2

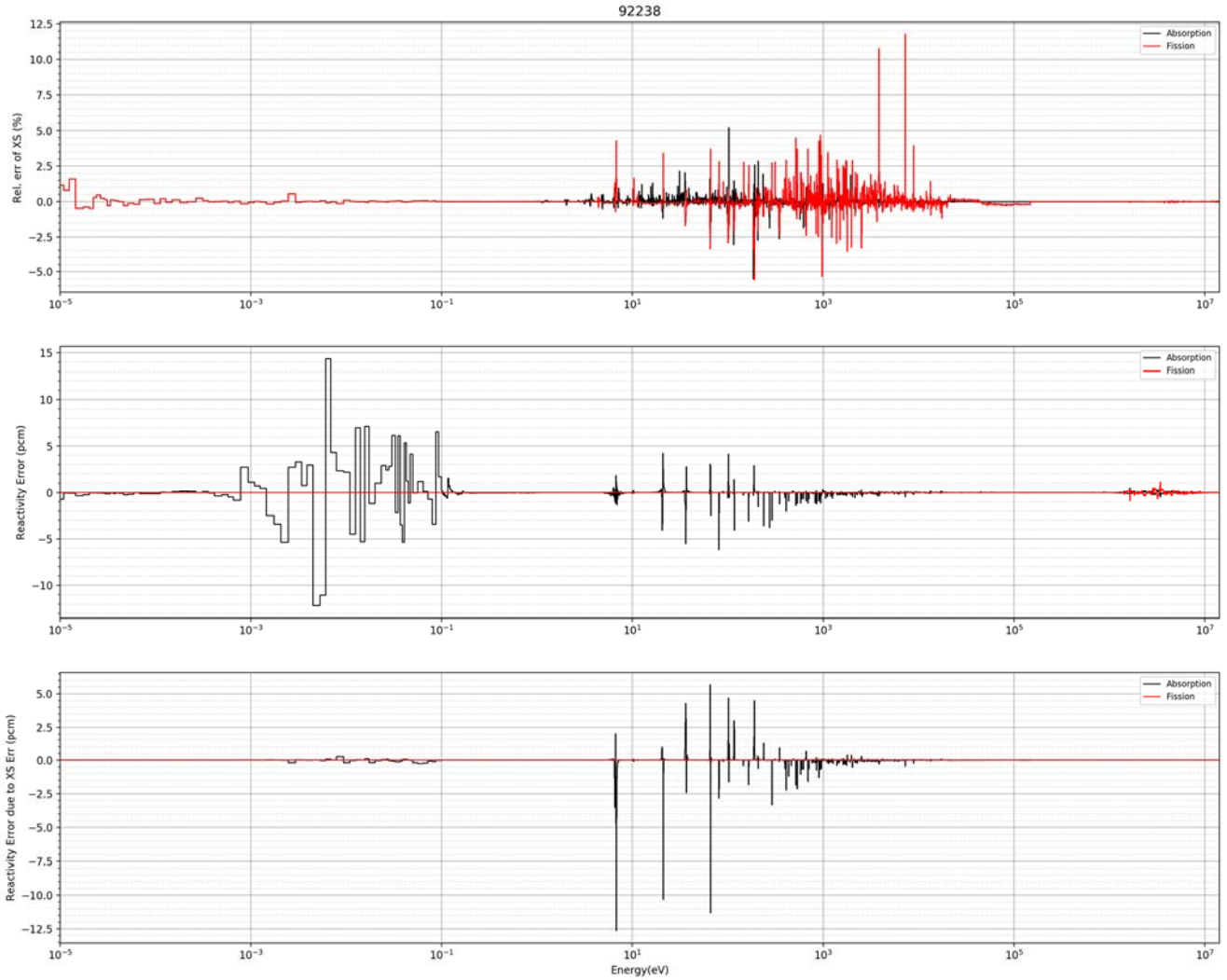

Figure 2.11 Relative cross section error (top), reactivity differences due to the cross section and flux errors (middle) and reactivity differences due to the cross section errors (bottom) of ^{238}U for P2

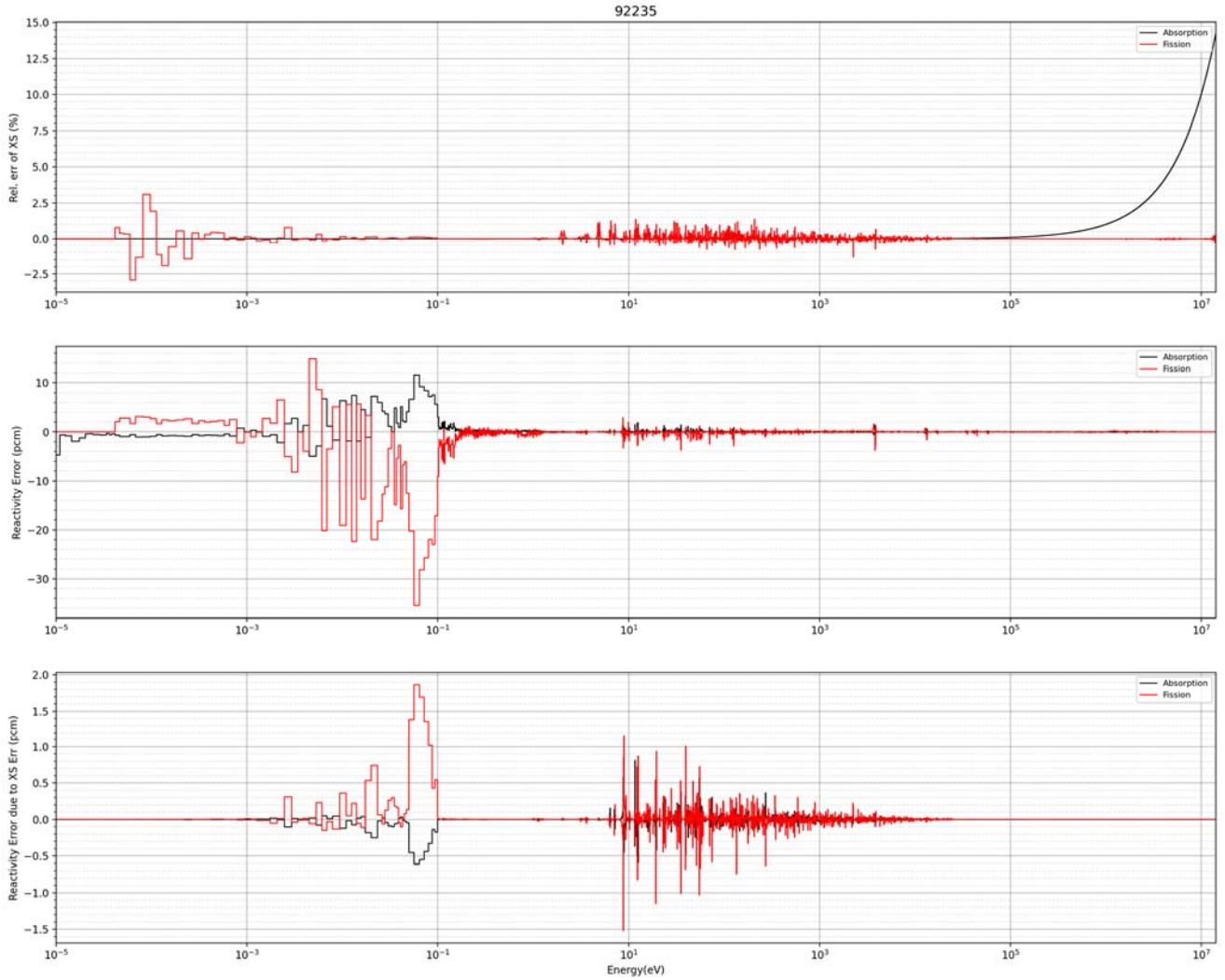

Figure 2.12 Relative cross section errors (top), reactivity differences due to the cross section and flux errors (middle) and reactivity differences due to the cross section error (bottom) of ^{235}U for B3

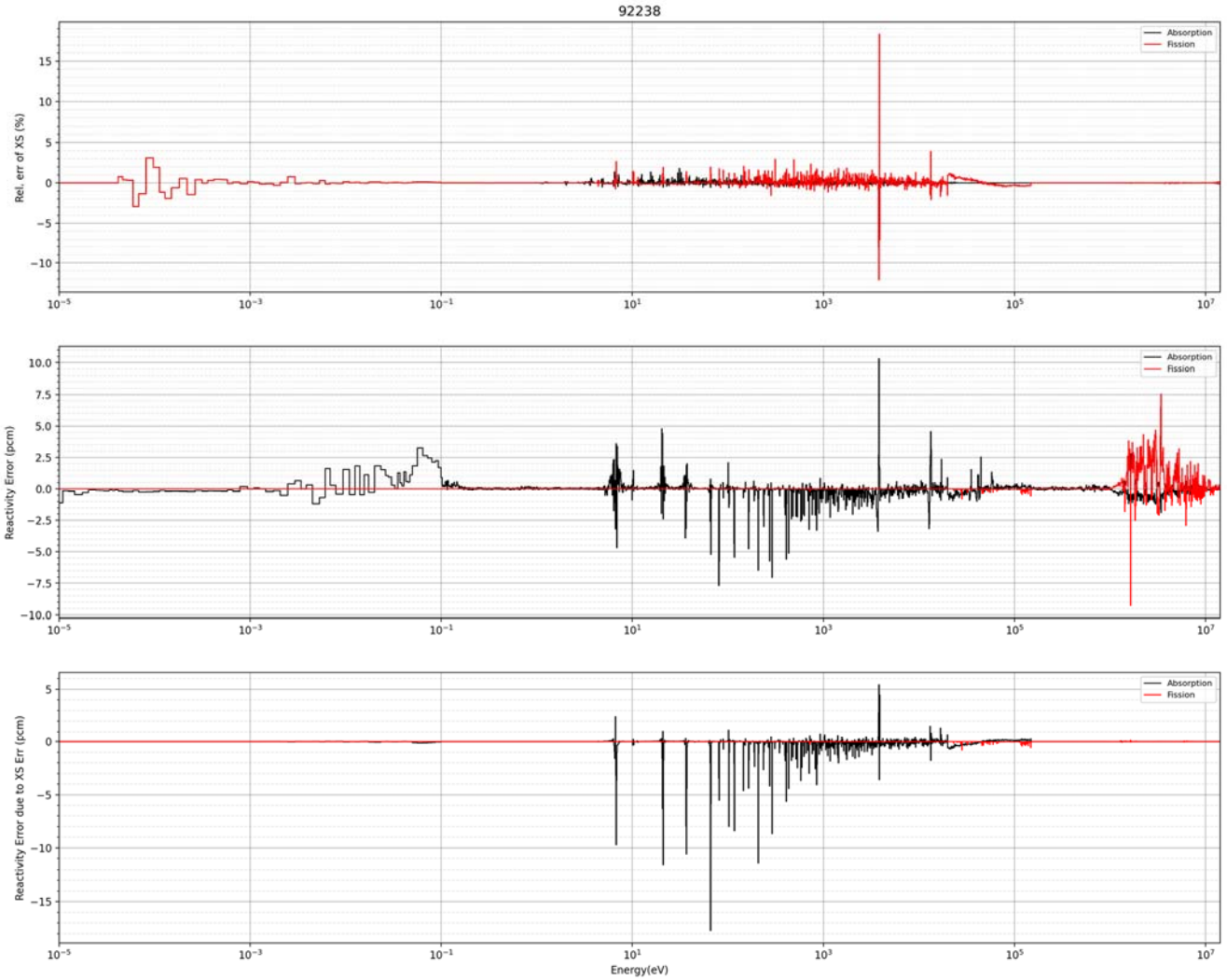

Figure 2.13 Relative cross section errors (top), reactivity differences due to the cross section and flux errors (middle) and reactivity differences due to the cross section errors (bottom) of ^{238}U for B3

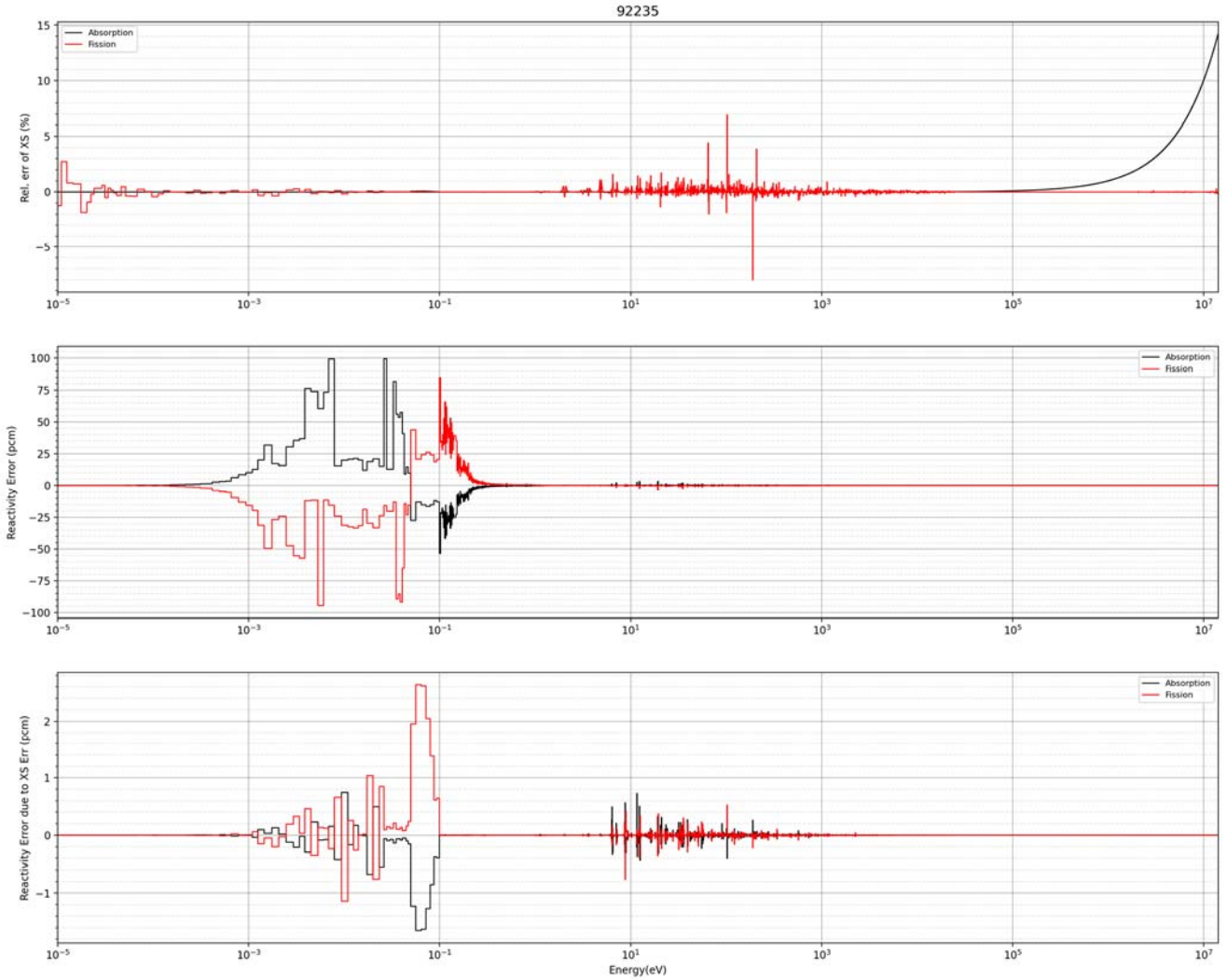

Figure 2.14 Relative cross section errors (top), reactivity differences due to the cross section and flux errors (middle) and reactivity differences due to the cross section errors (bottom) of ^{235}U for H1

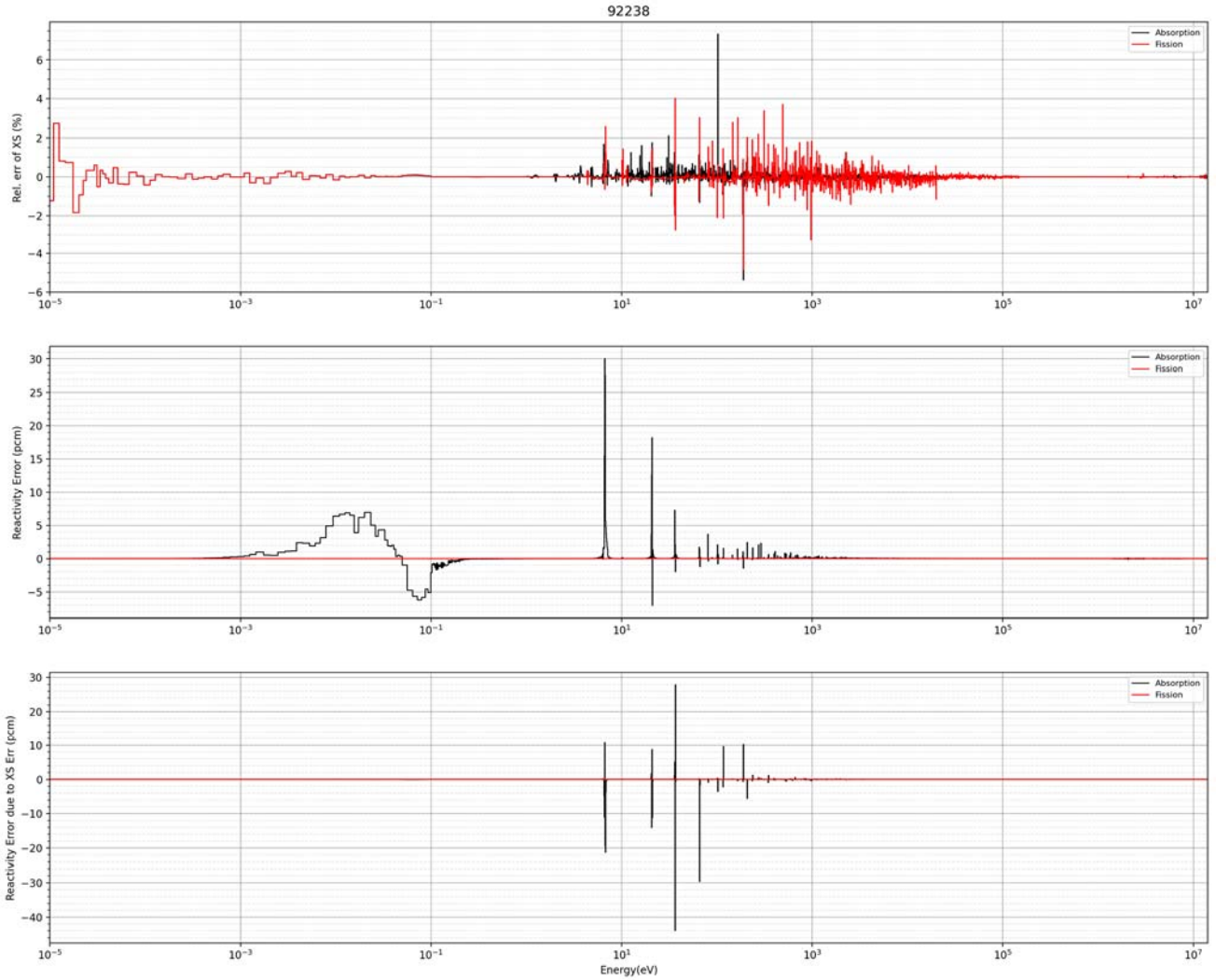

Figure 2.15 Relative cross section errors (top), reactivity differences due to the cross section and flux errors (middle) and reactivity differences due to the cross section errors (bottom) of ^{238}U for H1

2.3.2 Assembly benchmark results

The new procedure for multigroup XS generation was tested for four PWR fuel lattice problems, a BWR lattice problem with three different void fractions and one moderated target assembly design in LEU-fueled Break-even Fast Reactor (LEUBFR) [58,59]. The PWR problems are characterized by 17 x 17 PWR VERA fuel assemblies including several guide tubes and control rods. The layout of PWR lattice problem is presented in Figure 2.16, and detailed specifications can be found in [50]. The BWR test problem is a 9 by 9 BWR fuel assembly design based on [51], which has five different types of fuel rods with different ^{235}U enrichments from 3.0 wt. % to 6.3 wt. %. The isotopic composition and geometrical configuration of this BWR fuel assembly are presented in Table 2.6 and Figure 2.17, respectively. Note that the two large water rods at the assembly center were described as seven small water rods with the same volume fractions and the assembly box and the water gaps between assemblies were not modeled for simplicity.

The advanced fast test reactor designs that the moderated target assembly is loaded in the periphery of fast reactor core have recently been proposed to enhance the natural resource utilization and reducing the nuclear waste. The main purpose of the proposed target assembly is to transmute the recovered minor actinides from discharged fuels by utilizing neutrons leaking from the active core. In addition, hybrid reactors that aim to achieve high levels of fast and thermal neutron fluxes are being studied to meet the irradiation needs. Due to the limitation of the current deterministic MG XS generation procedure, which cannot process thermal and fast MG XSs at the same time with detailed physics, those analysis are limited to the MC based approach. The new generalized MG XS generation procedure, however, can handle those hybrid spectrum system. To verify this, the moderated minor actinide target assembly of LEUBFR design is solved using Serpent-2 and the hexagonal geometry solver of MC^2-3. Figure 2.18 shows the configuration of

moderated target assembly. Detailed compositions and geometry of the moderator assembly in the LEUBFR design can be found in [58].

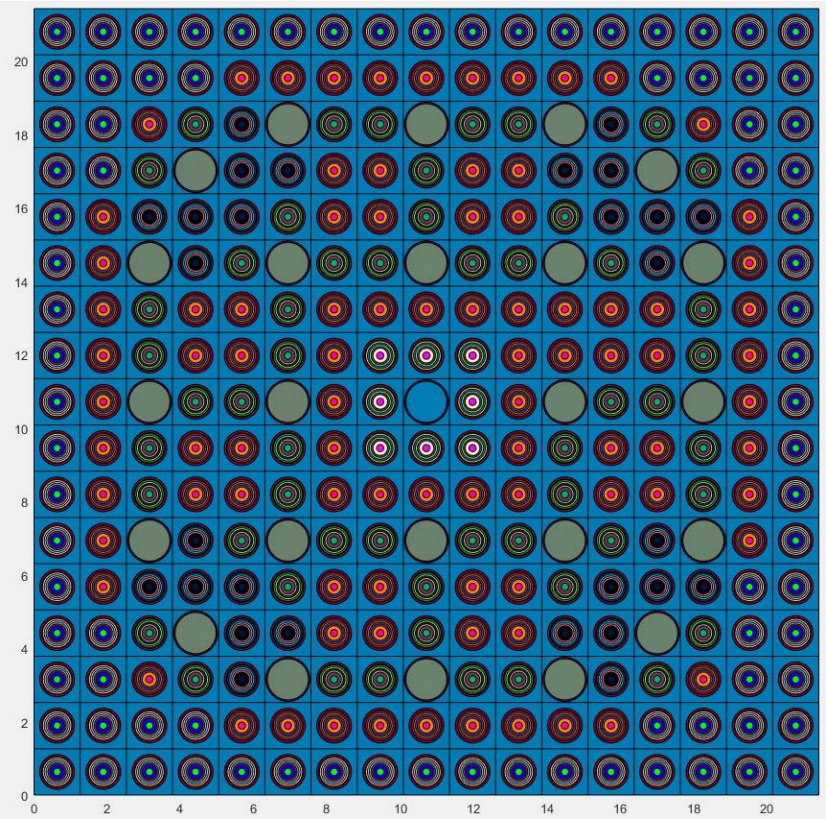

Figure 2.16 Lattice layout (P2H) for VERA benchmark problems

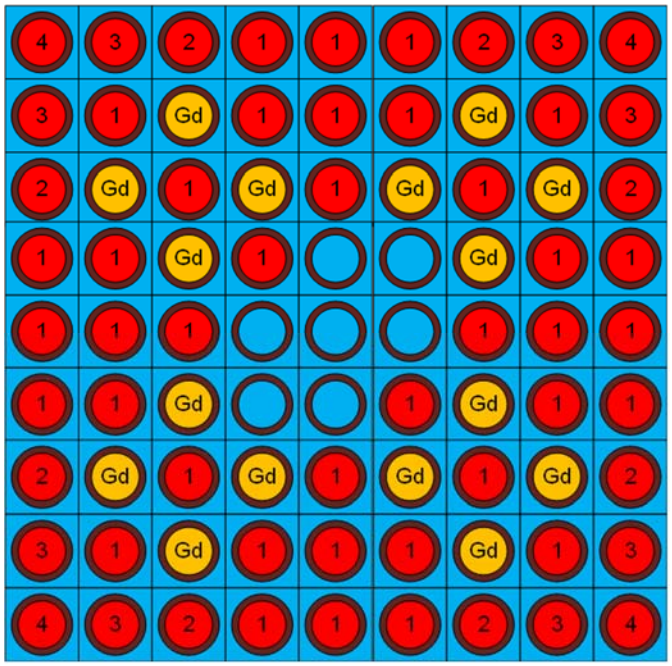

Figure 2.17 Lattice layout for BWR benchmark problems

Table 2.6 Isotopic compositions of BWR fuel assembly

Type	Fuel 1	Fuel 2	Fuel 3	Fuel 4	Fuel Gd
Nuclide	Number density				
92235	1.432E-03	1.137E-03	9.094E-04	6.820E-04	1.039E-03
92238	2.103E-02	2.132E-02	2.155E-02	2.177E-02	1.949E-03
8016	4.493E-02	4.492E-02	4.492E-02	4.491E-02	4.399E-03
Zr-nat	4.311E-02	4.311E-02	4.311E-02	4.311E-02	4.311E-02
64154	-				4.186E-05
64155					2.874E-04
64156					3.995E-04
64157					3.060E-04
64158					4.854E-04
64160					4.309E-04

The 2D MOC calculation in MC^2-3 was performed with a ray spacing of 0.05 cm, 16 azimuthal angles, 4 polar angles (for π) and P_2 anisotropic scattering treatment. The UFG XS sets including the scattering matrices need to be stored during the computation, which requires

substantial memory. In this work, the region-dependencies of UFG XSs for fuel pins were approximately considered by grouping them into multiple sets. For examples, the PWR P2H problem consists of eight UFG XSs sets for fuel: the fuel rods adjacent to the guide tube, center water hole, control rods, inter-assembly gap and the remaining ones depending on their positions as shown in the Figure 2.16. The BWR problems also have five UFG XS sets with different fuel compositions and the LEUBFR problem has a single UFG XS set as shown in the Figure 2.17 and Figure 2.18, respectively. For the annular regions of a fuel pin that have the same radial location and the XS group, a single set of escape XSs was obtained by averaging their variations. The fission energy of each pin cell was calculated using the F7 tally function of MCNP6. It is noted that the current MC^2-3 does not support the automatic generalized condensation scheme for the hexagonal geometry. As a result, multiple independent MC^2-3 runs are invoked to perform the generalized condensation scheme manually for the moderated target problem.

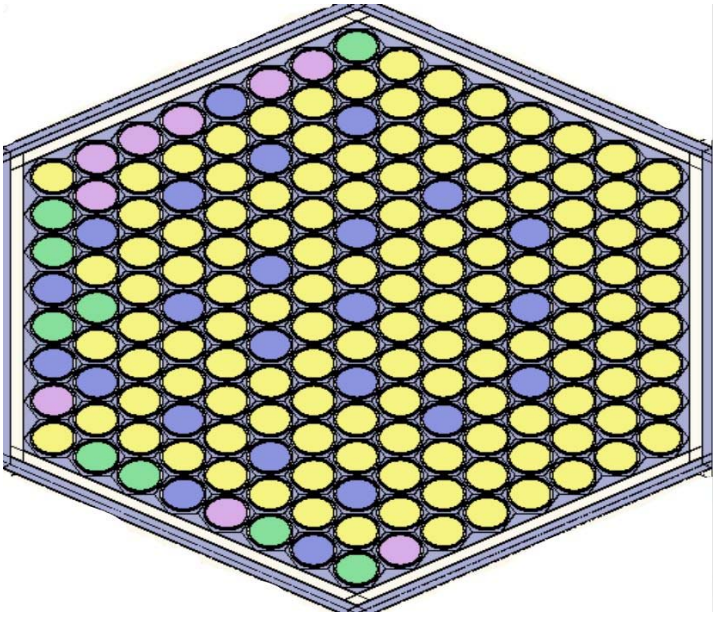

Figure 2.18 Hexagonal layout of moderated target assembly

Table 2.7 presents the k-infinity values, RMS and maximum pin-by-pin fission power errors of MC^2-3 against MCNP6 solution for the lattice problems. Here, the UFG calculation indicates the 3,483-group heterogeneous lattice calculation. The IG calculation were performed with the condensed IG XSs using the generalized group condensation schemes. In general, the MC^2-3 code successfully reproduces the reference k-infinity results of MCNP6 for various lattice problems except for the P2H case. The maximum difference in k-infinity between MCNP6 and MC^2-3 results is 291 pcm for PWR problems (P2H), -140 pcm for BWR problems (40% voided case) and 209 pcm for LEUBFR problem. The maximum error of P2H case is mainly due to the flux errors in thermal, which was caused by the temperature dependency in hydrogen kernel. Note that the P2H case includes the multiple B4C control rods, and thus the error cancellation between capture and fission breaks due to the presence of thermal absorbers in the assembly. Similarly, the BWR problem with 40 % void fraction shows larger reactivity difference than the one with higher void fraction because of the presence of gadolinium and softened spectrum. The MC^2-3 power distributions appear to agree well with the MCNP6 solutions. The maximum and RMS errors of pin-by-pin fission power are 1.21% and 0.58% for PWR fuel assemblies, and 1.08% and 0.54% for BWR fuel assemblies, respectively. The maximum pin power errors are observed in the vicinity of control rods and gadolinium bearing fuel. Table 2.7 also demonstrates the IG results which are condensed using the generalized condensation scheme. It was also observed that the eigenvalues and power distributions of IG calculation generally agree well with the corresponding UFG results. The IG results tend to slightly underestimate the eigenvalue result up to 50 pcm, especially for the PWR problems, while there is no noticeable difference in fission power errors. A recent study showed that the angle dependency of resonance XSs introduces the reactivity bias up to -300 pcm [60]. The neglect of angle approximation goes very wrong in the resonance energy range, where

XS within an energy group changes significantly. Since the angular flux varies over direction in a heterogeneous geometry especially at regions near high absorbers, the approximation can yield significant errors. This trend can be easily found in the P2H and 40% voided cases compared to other solutions. The widely used resolutions of the approximation is either applying angle correction factor [60] or impose the SPH factor obtained from MC solution to correct XS directly. However, this loses the generality of the generalized MG XS procedure by tuning the XS into the certain solution. Further investigation is needed to develop the fundamental process to resolve the angle dependency issue.

The efficiency improvements of the generalized condensation procedure were accessed in the PWR P2A problem. Both calculations with the UFG and the IG calculation were performed using twenty 3.0 GHz Intel Xeon Gold 6154 cores in Great Lakes cluster of University of Michigan. Using the generalized scheme with 51G IG structure reduces the computation time from about 40 hours to 3 hours as the number of groups decreased by factor of 70, from 3,483 to 51. An eight pin cell calculations (color set shown in Figure 2.16) take a half hour and 2D pin-homogenized lattice calculation takes an hour. Fixed source calculation to estimate the escape XS takes an hour and the remaining lattice calculation as well as the UFG XS preparation take a half hour.

Table 2.7 . Eigenvalues and fission power errors of MC^2-3 against MCNP6 solutions for lattice problems

Fuel	Remark	k-infinity & Power								
		MCNP k_{eff}	UFG calculation				IG calculation			
			k_{eff}	Diff (pcm)	RMS (%)	Max (%)	Group[a)]	Diff (pcm)	RMS (%)	Max (%)
PWR	P2A	1.18194 (10)	1.18156	-38	0.43	0.94	574	-54	0.43	0.94
							252	-57	0.43	0.94
							51	-60	0.43	0.95
	P2B	1.18282 (10)	1.18241	-41	0.38	0.72	574	-72	0.38	0.72
							252	-75	0.38	0.73
							51	-72	0.38	0.73
	P2C	1.17352 (10)	1.17296	-56	0.39	0.73	574	-75	0.39	0.73
							252	-74	0.39	0.74
							51	-75	0.39	0.74
	P2H	0.78254 (10)	0.78545	291	0.58	1.21	574	242	0.58	1.23
							252	242	0.58	1.23
							51	232	0.59	1.24
BWR	40% void fraction	0.95299 (10)	0.95159	-140	0.54	1.08	574	-171	0.54	1.08
							252	-172	0.54	1.09
							51	-176	0.54	1.10
	90% void fraction	0.87850 (7)	0.87794	-56	0.48	0.85	574	-74	0.48	0.84
							252	-74	0.48	0.85
							51	-74	0.48	0.87
	99% void fraction	0.86764 (5)	0.86721	-43	0.49	0.64	574	-51	0.49	0.64
							252	-51	0.49	0.63
							51	-51	0.49	0.65
LEUFBR	Moderated Assembly	0.24463 (10)[b)]	0.24672[c)]	209	0.42	0.82	574	210	0.44	0.82

a) 51 and 252G intermediate group structures are directly from MPACT, while the 574 G structure is newly developed by merging the existing ANL 619G (above 5eV) and MPACT 252G (below 5 eV) group structure

b) Calculated by Serpent-2 with the same option of MCNP6 calculation

Chapter 3 Generation of the Problem Dependent Cross Section Library for High-Fidelity Neutronic Simulation

The main goal of the high-fidelity neutronic simulation is to perform a whole core transport calculation with explicit geometry modeling. Individual MG XS generation is needed for each material such as fuel, cladding and coolant. T/H feedback and depletion scenario require the repeated MG XS generation calculations at each state point or time step. The parametrized RI table based XS library should be used as an inevitable resolution of the computation burden for the high-fidelity simulation, instead of the online XS generation using the UFG slowing down approach.

As aforementioned in the Chapter 2, the existing limitations of the RI table methods were not observed in the UFG slowing down approach, and thus the UFG solutions can be used to form the RI table. This indicates that the new XS library including the problem-dependent RI table can be applicable to any problem that the UFG slowing down approach can solve. Indeed, if the background XSs in downstream code are calculated in a consistent way as the one in MG XS generation code for the similar problem, the equivalence theory promises the satisfactory downstream code results as accurate as the one from the detailed slowing down calculation. In addition, the intra-pin flux distribution inside the fuel area, which was not represented in XS library generation procedure due to the limited number of branch calculations, can be partially modeled in the subsequent resonance calculation by calculating the background XS for fine XS meshes. Thus, this chapter presents the method to generate the XS library, the consistent connection between the XS library and the downstream calculation, and the improvement in the resonance calculation of the high-fidelity simulation.

In general, generating the XS library requires huge resources and time. Even if it is generated successfully, through validation and verification should be performed to check the validity of the library. For that, an existing XS library is adjusted to minimize these efforts for verification of the newly proposed approaches in this work. The MPACT [61] neutronics core simulator and its XS library are selected as a verification tool of a new XS library generation test. For the inclusion of the data into a MG library, an in-house XS manipulation code is developed to convert the MC^2-3 slowing down results into the MPACT XS library. To have the consistent background XSs, the same fixed source problem of MPACT was solved by MC^2-3. Although the preparation of problem dependent RI table using the detailed slowing down approach is more time consuming than the existing RI table-based procedure, it is needed only once prior to actual direct core calculations. Therefore, it is the crucial advantage that the new XS library generation procedure does not require significant computational time burden for the actual transport calculations while taking the rigor of the problem dependent RI tables.

Even though the new XS library are well prepared using the UFG slowing down calculation with the explicit geometry and generalized condensation scheme, methodologies in the downstream high-fidelity calculation still assume that the heterogeneity effect is generally considered to be weak in a normal LWR configuration. As a result, azimuthal dependency of macroscopic XSs inside of fuel, which is important for the advanced LWR designs, are ignored. For example, in a BWR, a void fraction can be highly different from region to region. This leads to different isotopic XSs and burnup rates along the azimuthal sectors which cannot be modeled with the current XS generation scheme. For this reason, the MPACT code has modified to explicitly consider the azimuthal region-dependent XSs and isotopic depletions along with the new XS library. In this chapter, the MPACT resonance self-shielding method is introduced first. Then,

the improvements of XS library generation and resonance calculation are given as well as the benchmark results.

3.1 MPACT Cross Section Library Generation

Figure 3.1 shows the conventional flow based on the RI table method to generate the XS library for the direct whole core neutronic codes although each simulator has their unique feature of their XS library generation procedure. The calculation starts with 1) reading the ENDF/B libraries to prepare the isotopic data libraries using the processing codes. The resonance XSs and scattering matrices are prepared using the specific weighting spectrum. 2) The Bondarenko method is applied to all materials by changing the compositions of problem to produce the data at different dilutions and isotopic temperature. 3) To overcome the limitation of Bondarenko method, the heterogeneous unit-cell slowing down calculation is often performed for the specified geometry and compositions with the PW of UFG data. The self-shielded MG XSs from the Bondarenko method are summed up with the resulting XSs from the slowing down calculation. 4) Those reference solutions are then used to form the RI table as a function of background XS. Since the RI table was precomputed before the direct whole core calculation, a simple fixed source lattice calculation to obtain the equivalent parameter is only needed in the real calculation, which saves the computational resources a lot. To generate the MPACT XS library, the AMPX, BONAMI and CENTRM modules of SCALE code packages are used for the above procedures form 1) to 3), respectively. In the MPACT XS library generation procedure, several programs are invoked externally to provide the data other than the RI table and principle XSs. Those data include the followings: IR parameter, subgroup data, SPH factors, transient data, transport corrected XS for hydrogen and atomic information as well as miscellaneous data. Since this chapter is mainly focusing on altering the resonance data and principle XSs of the current MPACT XS library, the

external procedures are not described in this dissertation. Detailed demonstration can be found in [62].

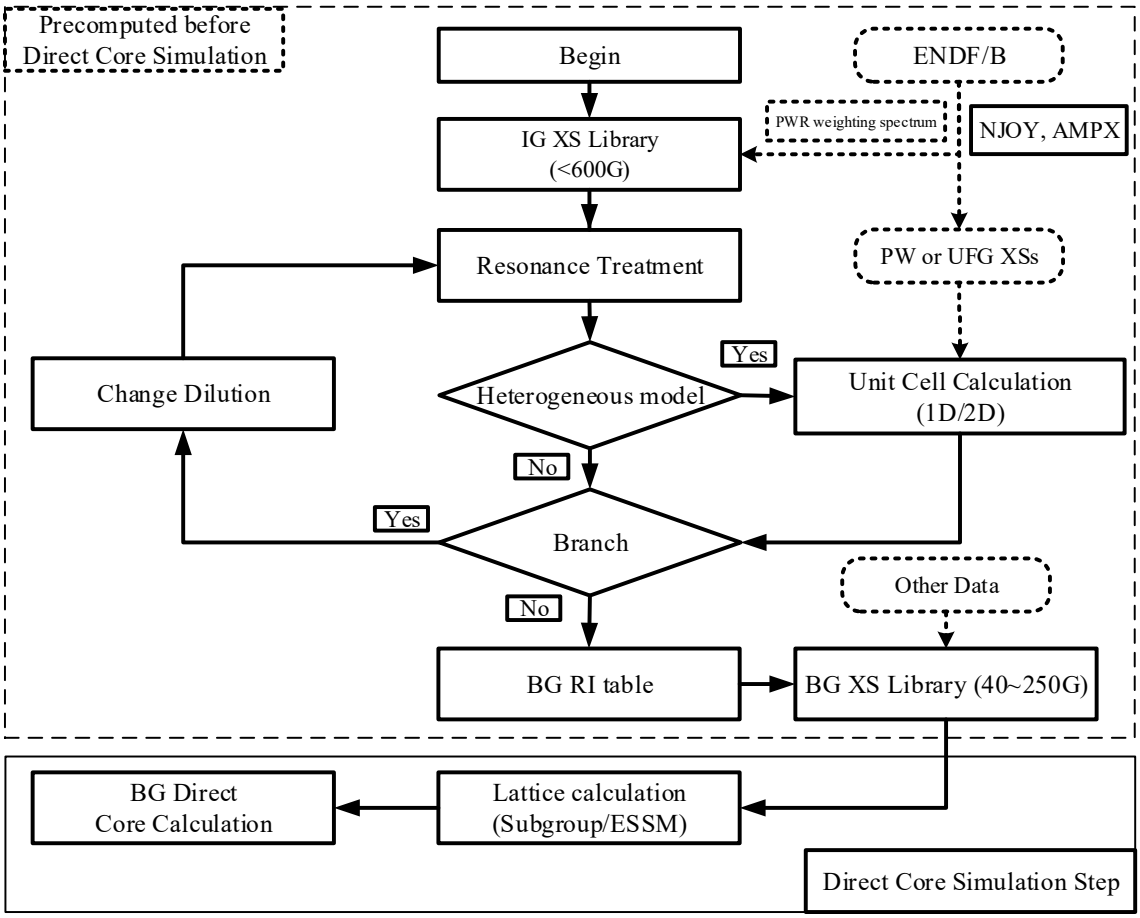

Figure 3.1 Conventional cross section library generation scheme for high-fidelity neutronic simulation

3.1.1 Embedded self-shielding method

The MPACT code employs the ESSM and subgroup method to prepare resonance self-shielded XSs. Although the subgroup method is good in estimating spatially dependent resonance self-shielded XSs in the lattice calculation stage, there are errors due to the least squares fitting that sometimes cause non-physical subgroup data. Therefore, the subgroup data may not be

generally applied to all nuclides and all energy groups. The ESSM is another variation of the Bondarenko method, which uses a precomputed RI table that is tabulated as a function of background XS and temperature. The main difference between the standard Bondarenko method and the ESSM is how the background XS is calculated [16]. In the ESSM, the escape XS is iteratively determined by interpolating effective XS and solving a fixed-source transport problem for the geometry and composition of interest, typically a 2D plane of the core and reflector. Usually, the absorption XSs at fuel and cladding are iteratively determined by solving the following equation [62]:

$$\hat{\Omega}\cdot\nabla\psi_g(r,\Omega)+\sum_j(\Sigma_{j,a,g}+\lambda_{j,g}\Sigma_{j,p})\psi_g(r,\Omega)=\sum_j\lambda_{j,g}\Sigma_{j,p} \tag{3.1}$$

where λ is the IR parameter in Eq. (1.14) for nuclide j. Then, the corresponding microscopic background XSs can be obtained using the scalar flux solution of Eq. (3.1) as

$$\sigma_{j,b,g}=\frac{\Sigma_{j,a,g}\phi_g}{1-\phi_g}\frac{1}{N_j} \tag{3.2}$$

This iteration scheme is described in Figure 3.2.

Fixed source calculation (ESSM)

```
! Purpose) Obtain converged background cross section
for each ESSM iteration
  for each cell in lattice
    for each material region in cell
      calculate XSs using background XS
    endfor
  endfor
  perform the FSP calculation
  for each cell in lattice
    for each material region in cell
      calculate escape XS using the FSP solution
    endfor
  endfor
endfor
save background XS for the heterogeneous MOC lattice calculation
```

Figure 3.2 Pseudo code for the fixed source calculation in ESSM

One of the major limitations of ESSM, originated from the one of the Bondarenko method, is the neglect of spatial self-shielding effect within fuel pin subdivision. Recently, ORNL developed a spatially dependent ESSM (SDESSM), within the framework of the Bondarenko method, for non-uniform temperature distribution inside fuel pellet, and SDESSM is successfully incorporated into MPACT.

3.1.2 Current cross section library assessment and new library generation procedure

Chapter 1 described the limited applicability of the current RI table method other than LWR. Since the current XS library was generated using the LWR heterogeneous model, the bias becomes noticeable when the geometric and isotopic composition of target problem changes greatly from the reference model. Prior to generating the new XS library, it is worthwhile to investigate the drawbacks of the current MPACT MG library for a wide range of advanced LWR problems. However, a direct assessment of the current MPACT library cannot be performed because all necessary programs to generate the MPACT library are not available outside of ORNL. Moreover, the latest MPACT libraries are generated using the SPH factor, which corrects the absorption cross section of ^{238}U by preserving the reaction rates of reference MC solutions to eliminate possible error sources (e.g., angle dependency of total XS and higher-order scattering matrix errors). To isolate the bias coming from to the limitations of the current RI table generation procedure from the SPH correction, thick pin BWR problems were solved by nTRACER [63] with the two 47G XS libraries generated with a typical PWR heterogeneous model and a thick pin BWR model. The libraries were generated using an in-house code without any additional correction. Table 3.1 shows the reactivity difference due to the XS errors for the BWR fuel pin, in which the pin cell size increased by 1.5 times to model thicker pin geometry of Peach Bottom BWR. Detailed composition is the same as the P2 case in section 2.3.1. Note that the resonance self-shielding

method used here is the subgroup method. It can be seen from the table that the use of the XS library prepared with the BWR pin model reduces the reactivity error from 85 pcm to 34 pcm in epithermal energy range where the RI table produces the resonance self-shielded XSs.

Table 3.1 Reaction rate comparison of two cross section model in the library generation

Case	Heterogeneous model	Reactivity difference[b] [pcm]		
		Fast	Epithermal	Thermal
P2[a]	Typical PWR	23	85	52
	Thick pin BWR	23	34	27

a) Pin cell size was increased by 1.5 times
b) Calculated using Eq. (2.21) and (2.22)

Another limitation of the current XS generation procedure is that the NR or IR approximation in the course group is not applicable to broad scattering resonances of intermediate weight nuclides. In addition, the broad scattering resonances cannot be well represented by constant background XSs in the current 51- and 252-group structure of MPACT library. Figure 3.3 shows the XS errors of oxygen resulting from the broad resonances in high energy range for the thick pin BWR problem with the 99% void fraction. Due to the hardened spectrum as shown in Figure 3.4, the smooth XS with the constant background XSs assumptions yield the noticeable XS and reactivity discrepancies for fast spectrum problems. In addition, the scattering moment matrices are compared with those tallied from the reference MC solution, McCARD [64]. A side-by-side comparison between the scattering matrix for PWR and that for 90% voided case of BWR fuel pins are presented in Figure 3.5 to facilitate a qualitative comparison. The relative errors are presented in color according to the color scale from -40% to 40%. The incoming groups are located on the x-axis and outgoing groups on the y-axis. Down-scattering is represented by the elements below the diagonal which connects the top left and lower right corners; up-scattering is above this

diagonal. When comparing the two error matrices here, the highly voided BWR case loses the accuracy in within-group and down scattering ratios.

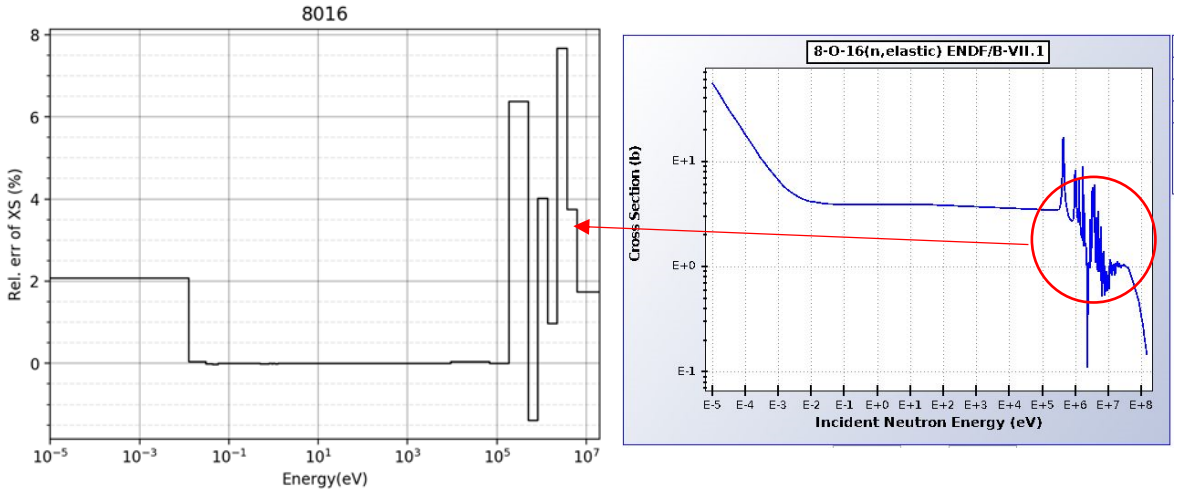

Figure 3.3 Relative error of total cross section of ^{16}O at high energy range

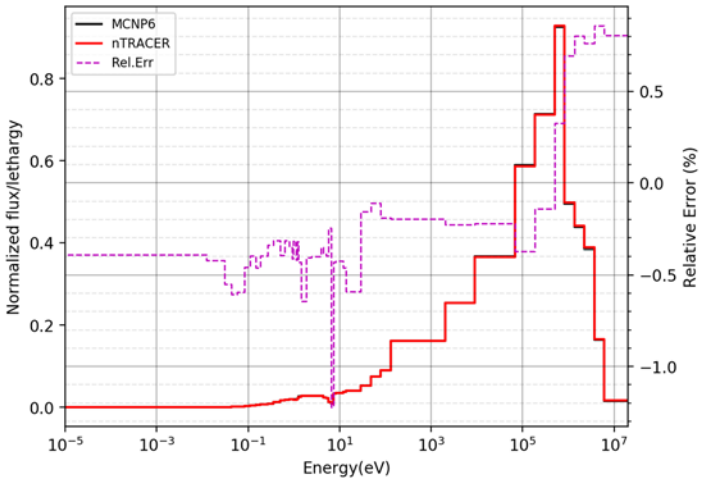

Figure 3.4 Comparison of 47G flux spectrum between MCNP6 and nTracer for BWR fuel pin

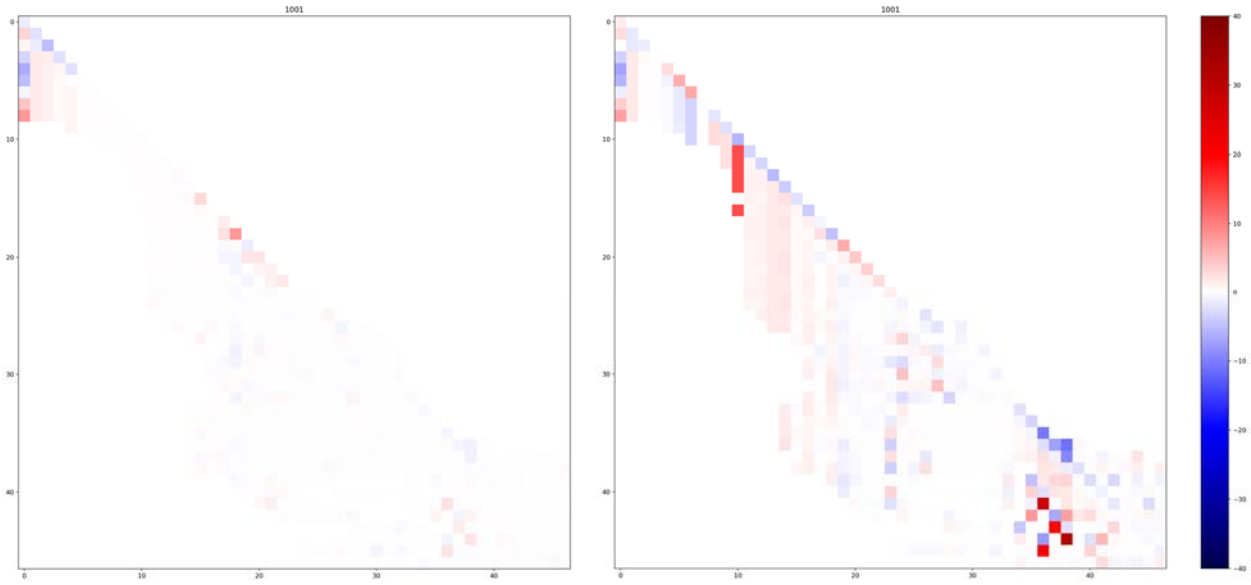

Figure 3.5 Relative errors (-40 to 40% color scale) of hydrogen scattering matrix for PWR (left) and 90% BWR (right)

As verified in the chapter 2, the new MG XS library generation procedure based on the detailed slowing down can successfully eliminate the resonance and scattering cross section errors. However, the current MPACT MG XS library format is not intended to directly incorporate with the newly generated self-shielded XSs and scattering matrices. A new cross-section library called the simplified AMPX XS library and processing procedure has recently been developed and implemented in MPACT to resolve the reported drawbacks of the MPACT MG library [65]. The simplified AMPX library includes resonance data for all nuclides and energy groups, and one noticeable change from the previous MPACT XS library is that the self-shielded XS itself is stored in the table rather that the RI. This simplified AMPX XS library of MPACT was used to test the newly developed detailed resonance treatment approach. To avoid confusion between two library formats, we use the term, AMPX XS library (the simplified AMPX-format MPACT XS library), hereafter. The AMPX XS library does not include a temperature and spectrum dependent elastic

scattering matrix; this results in noticeable bias in within-group and down scattering ratios for light-weight nuclides. As a remedy for the temperature effect, the AMPX library has a within-group XS for elastic scattering as a form of resonance table to adjust the ratio between total and within-group elastic scattering at certain temperature, while the spectrum effect is still not considered.

To consider the spectrum dependency as addressed in Figure 3.5, the AMPX XS library format is modified to store scattering matrices at different temperature and background XSs in this work. If the background XS is determined by the ESSM, the corresponding scattering matrix can be obtained through interpolation. Since the new library includes the temperature dependent scattering matrix, the within-group elastic scatterings are deleted. To minimize additional efforts to generate a new XS library, the resonance XSs and scattering matrices of existing XS library are replaced using the BG solution of MC^2-3. The following is a procedure to obtain the self-shielded XS table:

1) Prepare the UFG (~3,500G) XSs by solving UFG/HFG slowing down equation for each pin cell problem
2) Condense UFG self-shielded XSs into IG XSs for the absorption and fission reactions and scattering matrices using the generalized condensation scheme, then condense IG XSs to BG XSs using the subsequent IG lattice calculation.
3) Solve Eq. (3.1) with the absorption and potential XSs for the lattice problem to obtain the scalar flux and corresponding background XSs. It is noted that the IR parameters in Eq. (3.1) are directly obtained from the existing simplified AMPX library.
4) Obtain multiple self-shielded XSs and background XS sets by changing the fuel configuration that user specified in the input. Currently, an automatic procedure was

developed to change the fuel radius, moderator density and uranium enrichment. In this chapter, moderator density was only chosen to tabulate the background XS for thermal reactor analysis of MPACT.

Figure 3.6 shows the above procedure to generate a new AMPX XS library for the MPACT simulation. A detailed MC^2-3 procedure other than the XS library generation can be found in the subsection 2.2.2.

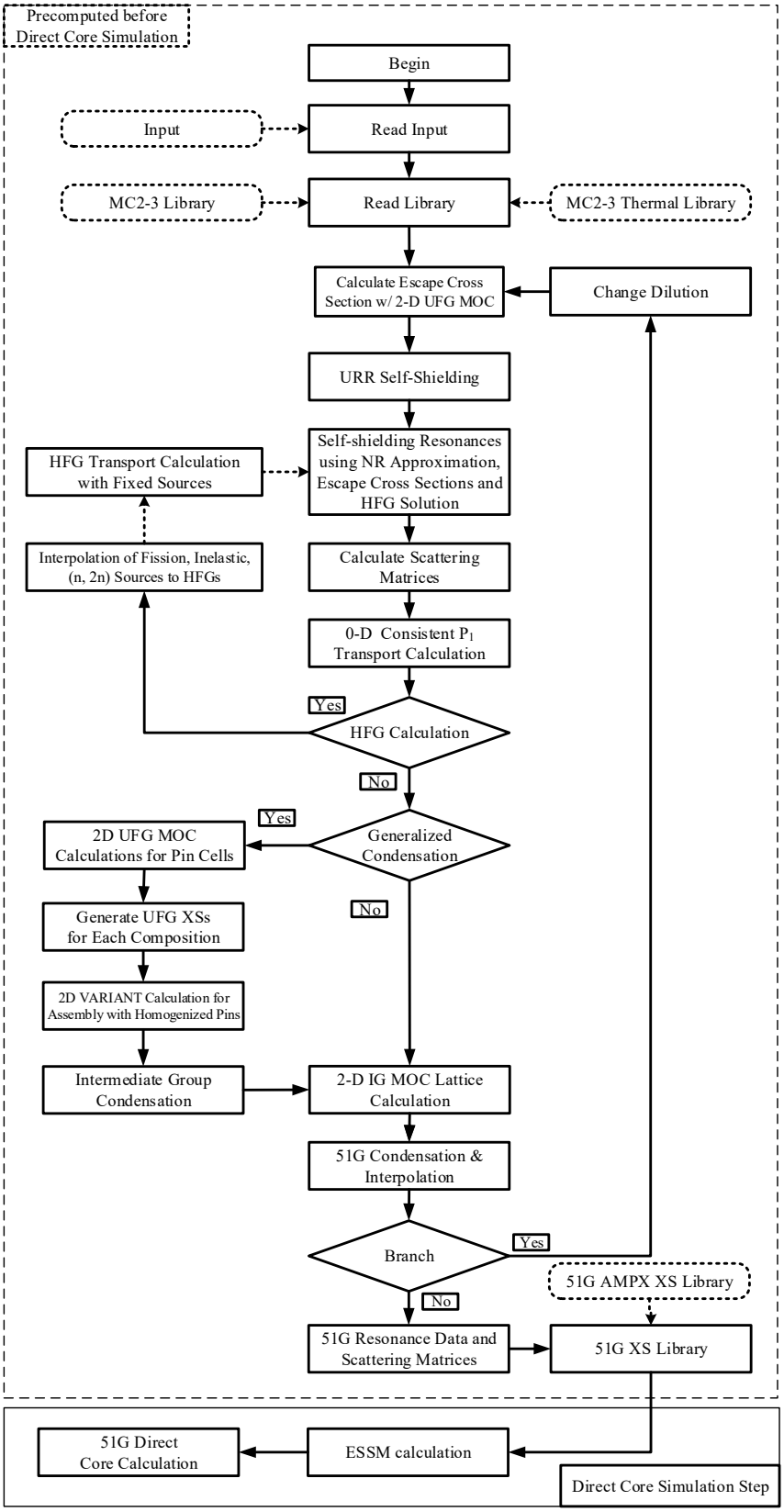

Figure 3.6 New cross section library generation scheme for high-fidelity neutronic simulation

3.2 Azimuthally Dependent Cross Section Generation

In a BWR, a void fraction can be highly different from region to region. For high voided cases, the void fractions inside an inter-assembly gap and a water hole are still zero, while those in fuel pin cells are highly voided. In this case, more neutrons are moderated in those sectors near an inter-assembly gap and a water hole than in the sectors near fuel pins. Accordingly, there are significant differences in neutron spectra along the azimuthal sectors. In addition, the local void fraction is not uniformly distributed since pin-powers are significantly different at gadolinia pins. This leads to different isotopic burnup rates along with the azimuthal sectors that cannot be modeled with the current depletion scheme of MPACT that depletes isotopes uniformly in each annular region. It was reported that the azimuthal-division of the Gadolinia-bearing fuel rods has impacts on the reactivity by 0.15% Δk/k during a burnup cycle [66]. As the accurate estimation of the gadolinia depletion is crucial for BWR analyses, the azimuthal region-dependent XSs and isotopic depletions scheme are implemented in MPACT.

Current MPACT code differentiates the mesh for sources and fluxes and the mesh for XSs. The former is called the MOC mesh and the latter is called the XS mesh. Fluxes and sources are calculated for each MOC mesh that has eight azimuthal sectors by default and XSs are evaluated for each XS mesh. These meshes are different as shown in Figure 3.7. The left one is the MOC mesh which uses eight azimuthal sectors as independent regions for source and flux, and the right one is the XS mesh that does not distinguish azimuthal sectors. The burnup region belongs to the XS mesh for which the isotopic depletion is calculated. This work matched the XS mesh to the MOC mesh and examined the effect on the results of the steady state and burnup calculations. To calculate the escape XSs in the resonance self-shielding calculation, the fixed source problems in Eq. (3.1) are solved for each resonant isotope. When the XS mesh of the right figure in Figure 3.7

was used, fluxes were homogenized for each fuel ring and escape XSs were calculated using the homogenized fluxes. In the new scheme, the escape XS for each azimuthal sector is calculated by using the flux for the region without any homogenization. For the burnup calculation, by matching the XS mesh to the MOC mesh in the MPACT code, the isotopic depletion calculation is performed for each azimuthal sector. This new scheme is designated as the azimuthal discretization scheme in the remaining part of this chapter.

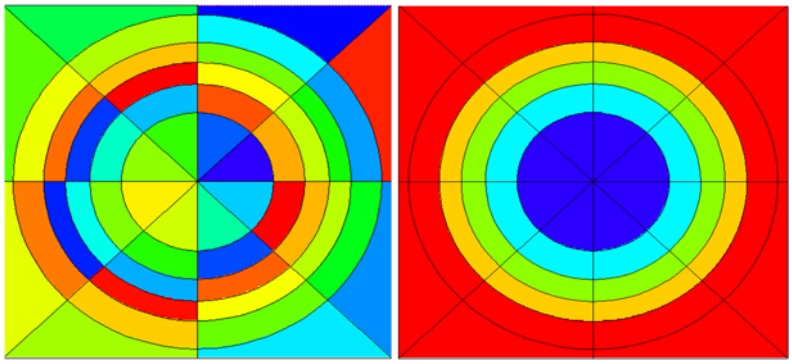

Figure 3.7 The MOC mesh (left) and the XS mesh (right) in MPACT

3.3 Numerical Tests

3.3.1 Impact of azimuthally dependent cross section generation and burnup

The newly developed azimuthal discretization scheme was tested by solving 3 by 3 and 10 by 10 BWR fuel assembly benchmark problems which are based on the GE-12 BWR design. To examine the efficacy of the developed feature for different void fractions, the benchmark problems were modified by varying void fractions. Table 3.2 provides a brief description of the six benchmark problems solved. Two 3 by 3 pin-cell problems were derived from the 10 by 10 GE-12 assembly problem with minor simplifications to examine the water hole effect on XSs at

adjacent pin-cells. Figure 3.8 and Figure 3.9 show configurations of the two problems, respectively. To simplify the problem, the inter-assembly gap and the channel box were neglected for the 3 by 3 problem. To examine the variation of XSs at different azimuthal sectors of the pin-cell adjacent to the water hole at the center for different void fractions, two calculations were performed by assigning different void fractions outside of the water hole in the center pin-cell and in the moderator regions of the surrounding pin-cells. The calculation for case 1 was performed with 3.5% and 35% for the two regions, respectively, and the calculation for case 2 was performed with 35% and 90% for the two regions, respectively. Inside the water hole, 0% void fraction was used for both problems. With these two problems, XSs and transport solutions of MPACT with and without the azimuthal discretization scheme were compared with those of MCNP6. The current MPACT MG XS library was used for calculations. Table 3.3 presents the k-infinity values of MPACT for cases 1 and 2. The results show that the azimuthal discretization scheme has little effect on eigenvalue for a steady-state problem. Figure 3.10 shows the relative errors of 23rd group ^{238}U absorption XSs at eight azimuthal sectors of the outermost ring among the three equi-volumetric rings in the fuel region with respect to those obtained from MCNP6. The 23rd group includes the 6.67 eV resonance of ^{238}U. The black ones are for the calculation without the azimuthal discretization scheme and the red ones are for the calculation with the azimuthal discretization scheme. Note that there exists a negative bias up to -20% ~ -25% on ^{238}U absorption XS mainly originated from the current XS library bias and the adjustment of ^{238}U absorption XS using the SPH factor to reduce the condensation error [67]. The XS errors at the two azimuthal sectors facing the water hole were reduced by 3% and those at the opposite sectors slightly increased by less than 1%. Though the azimuthally dependent XS effect is not noticeable on eigenvalue in this problem, it could be larger when the intra pin flux distribution is varying significantly. This may lead to the

significant bias of estimating the amount of highly absorbing material, such as gadolinium, during burnup because of variation of intra pin flux yielding different absorption rate for each azimuthal sector as shown in the Figure 3.10.

Table 3.2 Brief Description of Three Benchmark Problems

Case	Configuration	Void fraction [%]	Enrichment of fuel [wt.%] (Enrichment of gadolinium)	Temperature [K] (Fuel/Clad/Mod)
1	3 × 3	35, 3.5[a)]	2.0	900/600/600
2	3 × 3	90, 35[a)]		
3	10 × 10	35	3.4	
4	10 × 10	90		
5	10 × 10	35	2.0, 2.8, 3.6, 3.95, 4.4, 4.9, 3.95 (4.0), 4.3 (4.0), 4.3 (5.0)	
6	10 × 10	90		
a) Void fraction near large waterholes				

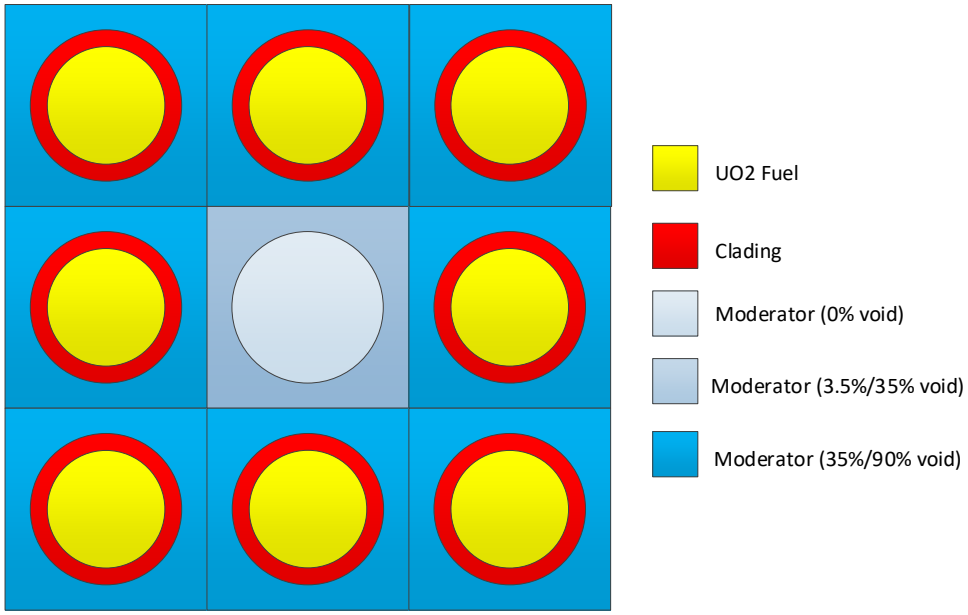

Figure 3.8 Configuration of simlified 3 by 3 pin-cell problem

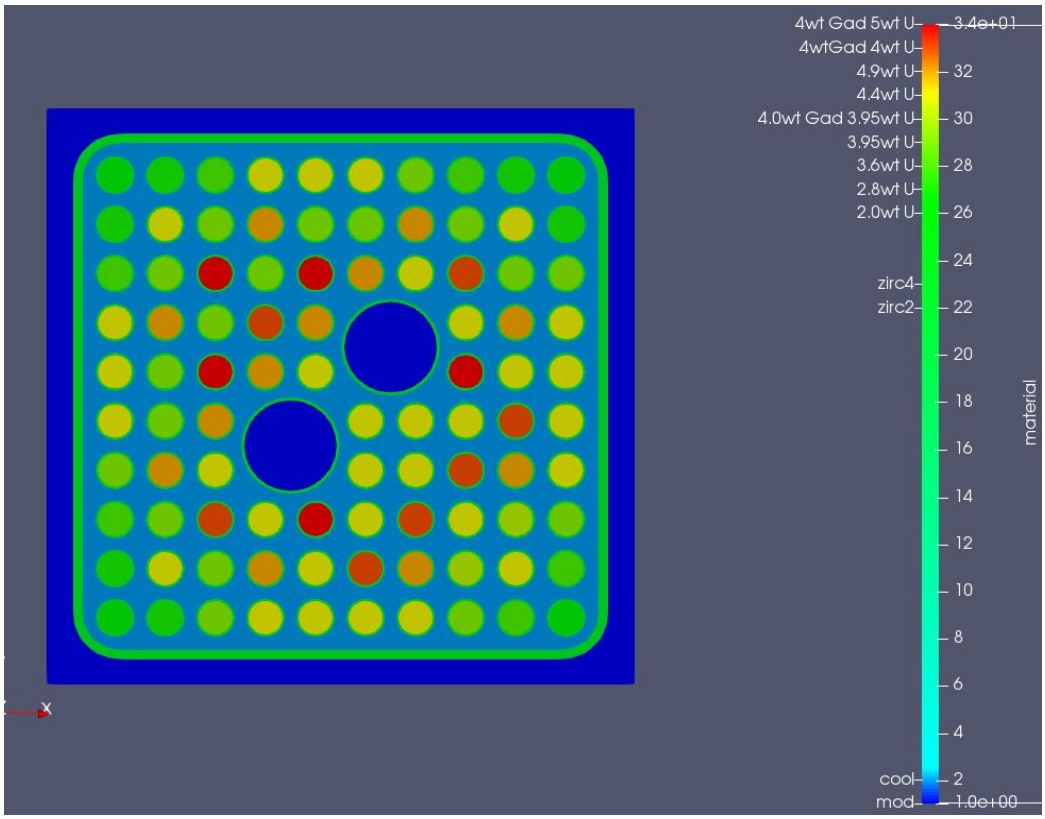

Figure 3.9 Configuration of 10 by 10 GE-12 assembly problem

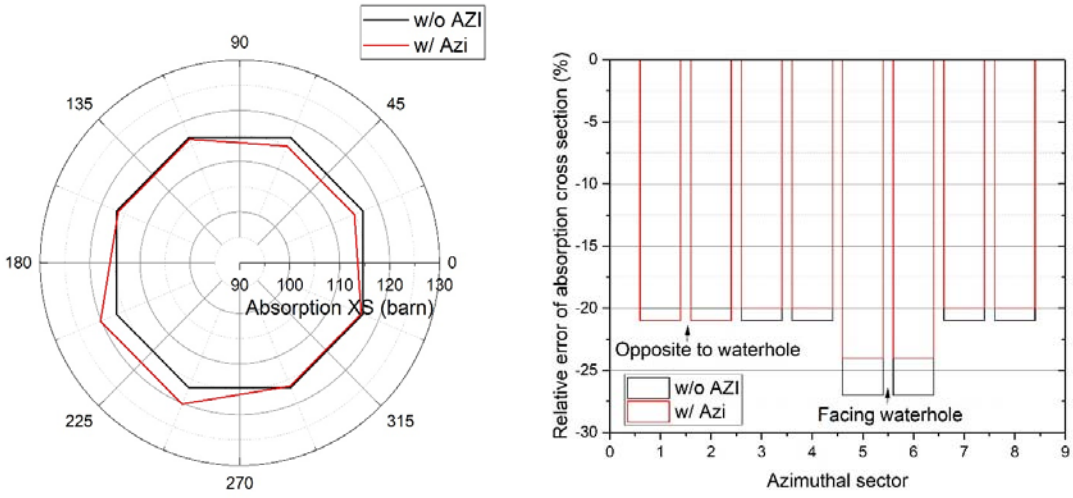

Figure 3.10 23-th group ^{238}U absorption cross sections at eight azimuthal sectors of the outermost fuel ring calculated with and without the azimuthal discretization scheme (left), their relative errors with respect to those of MCNP6 for case 1 (Right)

Table 3.3 Eigenvalue comparison of MPACT and MCNP-6 for GE-12 3 by 3 problems

Case	k_{inf}			Diff [pcm]
	MCNP	MPACT		
1	1.16575 (4)	w/o azi[a]	1.16433	-142
		w/ azi	1.16433	-142
2	0.85684 (4)	w/o azi	0.85555	-129
		w/ azi	0.85554	-130
a: the azimuthal discretization scheme				

The impact of the azimuthal discretization scheme on depletion calculations was examined with a realistic 10 × 10 GE-12 BWR fuel assembly. Table 3.4 compares the eigenvalue results of MPACT calculations without the azimuthal discretization scheme to those with the scheme for cases 3 to 6. Larger differences observed in the cases 5 and 6, compared to the cases 3 and 4, can be attributed to the more heterogeneous assembly configuration and asymmetry effect in gadolinium depletion. As the void fraction increases, the eigenvalue difference between the two schemes increases. At high-voided pins near an inter-assembly gap and a water hole, the neutron spectra in different azimuthal sectors vary significantly due to large difference in neutron moderation. If the sectors near an inter-assembly gap and a water hole, more neutrons are moderated than in the opposite sectors, and thus, the thermal flux is larger. This causes fissile isotopes in the sectors near an inter-assembly gap and a water hole to burn faster than in the opposite sectors. However, without the azimuthal discretization scheme, the average flux along the sectors at the same radial ring is used to calculate the burnup of the same annular region. This uniform burnup of each annular region induces higher difference for higher void cases than the non-uniform burnup for each azimuthal sector.

Table 3.4 Eigenvalue comparison of MPACT and MCNP-6 for GE-12 assembly problems

Case	k-eff (MPACT) at BOC		Diff at BOC, Min[a], Max[b] (GWD/MTHM) [pcm]
3	w/o azi	1.36471	20, 20 (at BOC[c]), 25 (at 60.1[c])
	w/ azi	1.36451	
4	w/o azi	1.29020	63, 54 (at 60.1), 63 (at BOC)
	w/ azi	1.28957	
5	w/o azi	1.06420	11, -67(at 4.1), 156 (at 10.1)
	w/ azi	1.06409	
6	w/o azi	1.01769	49, -48 (at 4.1), 227 (at 10.1)
	w/ azi	1.01720	

a) smallest value of the difference and the burnup time at which the value occurs
b) largest value of the difference and the burnup time at which the value occurs
c) beginning and end of cycle

Upon the presence of gadolinia, the uniform burnup of each annular region induces a larger difference because the gadolinia burnup drives the initial reactivity change. During initial depletion time steps, the burnup speed of gadolinium isotopes is faster when the azimuthal discretization scheme is used, while the opposite is true from the burnup time step at which most gadolinium isotopes near an inter-assembly gap or a water hole burned out. The overall neutron flux is higher in the sectors near an inter-assembly gap and a water hole than in the opposite sectors. On top of that, in the resonance energy groups, the effective XSs of gadolinium isotopes in the sectors near an inter-assembly gap and a water hole are also higher than in the opposite sectors because of larger background XSs. Since the average capture XS of an annular region calculated in the original scheme is not obtained by the flux volume-weighting, but by the average background XS obtained from the average flux of the annular region of the fixed source problem, the sum of capture reaction rates per gadolinium isotope in all sectors of the annular region is not preserved. It turned out that the sum of capture reaction rates per gadolinium isotope in all sectors of the annular region is smaller in the original scheme than in the azimuthal discretization scheme. This difference in the resonance capture rate in a gadolinia pin is not negligible at all because the

resonance capture rate is as large as the thermal capture rate. This is described in Figure 3.11 in which the energy group-wise capture reaction rates of ^{155}Gd and ^{157}Gd at 4.1 GWD/MTHM of the case 6 are shown. The thermal flux below 0.1 eV is almost zero, and accordingly, the resonance capture rate is as large as the thermal capture rate. Smaller resonance capture rate per gadolinium isotope in the original scheme leads to a slower burnup of gadolinium isotopes at the initial phase of depletion. This results in an overall over-estimation of gadolinium inventory at the initial burnup steps. Figure 3.12 shows the number density changes of ^{155}Gd, ^{156}Gd and ^{157}Gd with burnup, and absolute differences of the number densities obtained by the original scheme from those obtained by the azimuthal discretization scheme in a log scale. Note that, before around 4.6 GWD/MTHM, the number density of ^{155}Gd is higher and those of ^{156}Gd and ^{157}Gd are smaller in the original scheme. Although all gadolinium isotopes burn slower in the original scheme than in the azimuthal discretization scheme as explained above at initial burnup steps, the production rate of ^{156}Gd from the capture reaction of ^{155}Gd and that of ^{157}Gd from the capture reaction of ^{156}Gd are also smaller. Since the total capture rate of ^{155}Gd is much higher than that of ^{156}Gd due to much higher capture XSs of ^{155}Gd than those of ^{156}Gd, the under-estimated production rate of ^{156}Gd dominates the under-estimated capture rate of ^{156}Gd. Therefore, the resulting number density of ^{156}Gd is kept underestimated while ^{155}Gd burns slower up to 4.6 GWD/MTHM. For the same reason, as the number density of ^{156}Gd is smaller in the original scheme and ^{156}Gd inventory itself is the largest, the under-estimated production rate of ^{157}Gd dominates the under-estimated capture rate of ^{157}Gd. The resulting number density of ^{157}Gd is also kept underestimated before 4.6 GWD/MTHM.

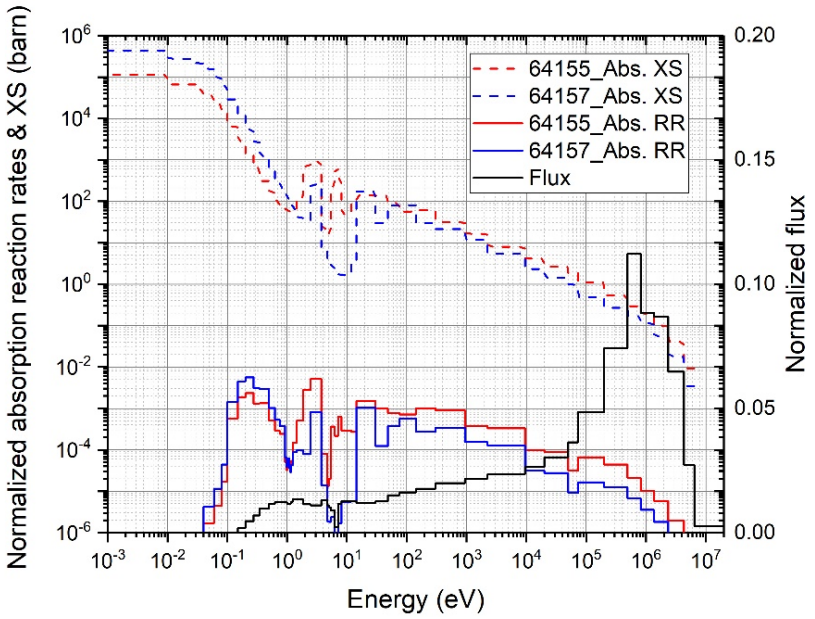

Figure 3.11 Comparison of absorption cross sections and reaction rates of Gd-155 and Gd-157 at 4.1 GWD/MTHM for case 6.

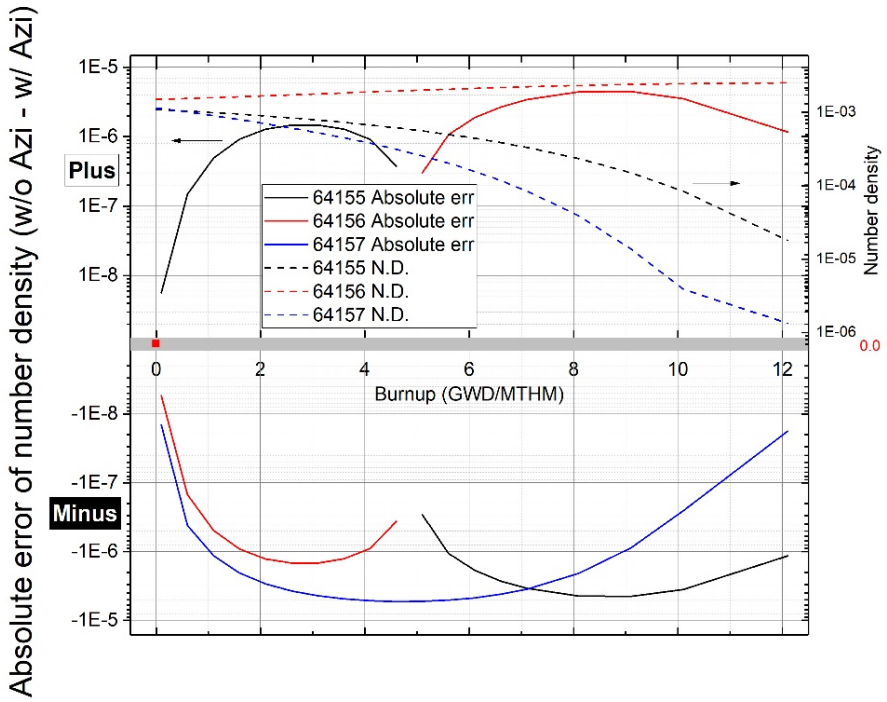

Figure 3.12 Comparison of number densities of gadolinium isotopes obtained from the MPACT burnup calculation without the azimuthal discretization scheme to that with the scheme

At the 4.1 GWD/MTHM burnup point, the burnup rate of ^{155}Gd in the original scheme exceeds that of ^{155}Gd in the azimuthal discretization scheme. Once ^{155}Gd is almost burned out in the sectors near an inter-assembly gap and a water hole in the azimuthal discretization scheme, the majority of ^{155}Gd isotopes remains at the opposite sectors where the thermal flux is relatively smaller. Meanwhile, ^{155}Gd burns uniformly at an annular region in the original scheme, and thus, some portion of ^{155}Gd isotopes are always exposed to higher thermal flux in the original scheme. This is illustrated in Figure 3.13 in which the ^{157}Gd inventory distribution is shown as blue colors. Greener colors indicate higher ^{157}Gd inventory. In the azimuthal discretization scheme, ^{157}Gd inventory is more skewed to the sectors at the opposite side to an inter-assembly gap and a water hole. However, in the original scheme, some portion of them is forced to move to sectors near an inter-assembly gap and a water hole and is exposed to a higher flux. Thus, the burnup rate of ^{155}Gd becomes faster in the original scheme. Note that, as shown in Figure 3.12, the rate of number density change of ^{155}Gd is more negative in the original scheme from near 3 GWD/MTHM. After the number density of ^{155}Gd becomes smaller in the original scheme than in the azimuthal discretization scheme, some portion of ^{155}Gd isotopes are always exposed to higher thermal flux, and thus, the number density of ^{155}Gd is kept under-estimated in the original scheme. As the total capture rate of ^{155}Gd is higher, the production rate of ^{156}Gd is higher, and thus, the number density of ^{156}Gd becomes higher in the original scheme than in the azimuthal discretization scheme. As the number density of ^{156}Gd becomes higher, the capture rate of ^{156}Gd becomes also higher. Even though the capture rate of ^{157}Gd is also higher in the original scheme than in the azimuthal discretization scheme, the absolute number density of ^{156}Gd is higher than that of ^{157}Gd, and thus, the production rate of ^{157}Gd dominates the capture rate of ^{157}Gd. This is the reason for the relatively

faster increase of ^{157}Gd in the original scheme than in the azimuthal discretization scheme after 4.6 GWD/MTHM.

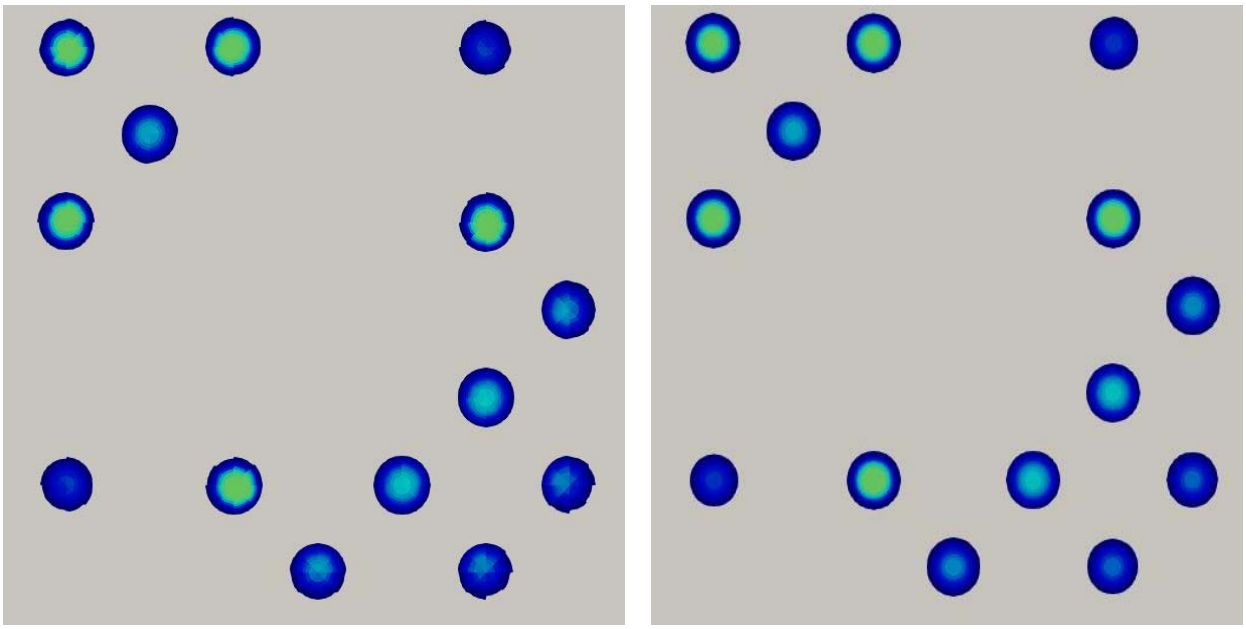

Figure 3.13 ^{157}Gd inventory distribution obtained with the azimuthal discretization scheme (left) and with the original scheme (right) at 4.1 GWd/HTU for Case 6.

This analysis on the difference in the gadolinia burnup rate between the original scheme and the azimuthal discretization scheme well explains the eigenvalue difference shown in Figure 3.14. Before 4.1 GWD/MTHM, the over-estimated ^{155}Gd inventory results in a slightly negative reactivity error in the original scheme. Even though the number density of the other major thermal absorber ^{157}Gd is under-estimated, the reaction rate comparison in Figure 3.11 indicates that the total capture rate of ^{155}Gd is slightly higher than that of ^{157}Gd due to higher resonance capture XSs of ^{155}Gd. After 4.1 GWD/MTHM, the number densities of both ^{155}Gd and ^{157}Gd are under-estimated, and thus, a large positive eigenvalue error is observed in the original scheme. Note that, even though the number density of ^{156}Gd is over-estimated, its capture XS is small, and thus, its

impact on reactivity is much smaller than that of the capture reactions from ^{155}Gd and ^{157}Gd. When gadolinium isotopes burn out completely, the eigenvalue errors almost vanish.

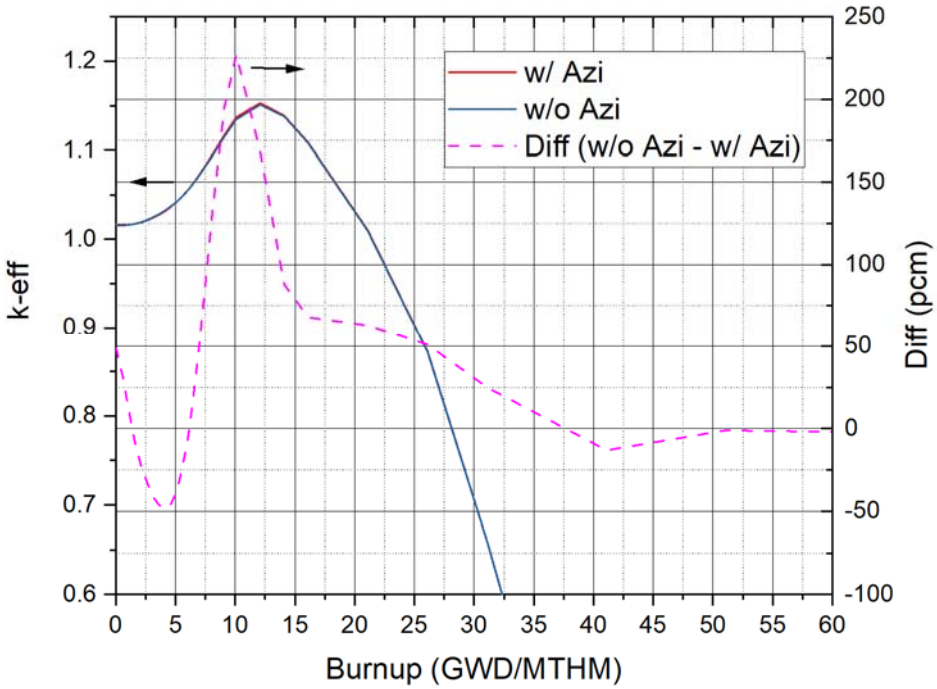

Figure 3.14 Comparison of the multiplication factor obtained from the MPACT burnup calculation without the azimuthal discretization scheme to that with the scheme for Problem

3.3.2 Verification of new cross section library

The new XS library was tested using the PWR case P2C in section 2.3.2 and GE-14 problems with 40% and 80% void fractions in the subsection 3.3.1. In order to study the accuracy of the new XS library generation procedure, the same calculations were performed with a library generated using the current pin cell heterogeneous model. Thus, the difference between old and new procedure are 1) heterogeneous pin cell vs. assembly model for the UFG slowing down calculation, 2) direct group condensation from UFG vs. multistep group condensation using the generalized condensation scheme, and 3) a single scattering matrix vs. multiple scattering matrices

with respect to the background cross XSs. To calculate the background XSs for each heterogeneous model, geometric and composition variations in the pin cell are obtained from [62], while only moderator densities are changed in the assembly model. Note that the self-shielded XSs are obtained by averaging multiple UFG XS sets in the assembly configuration. Table 3.5 and Table 3.6 provide those variations for each model. The reference pin cell model at case 5 is identical to the PWR problem P2. Azimuthal discretization scheme is applied to all calculations. Table 3.7 shows the eigenvalues and fission power errors of MPACT against MCNP6 solutions for assembly problems using two libraries. For the PWR problem, the eigenvalue discrepancies with the new scheme are at the similar level with those with the current scheme. On the other hand, noticeable improvements are observed in the eigenvalue and fission power results of GE-14 problem. In particular, for the pin power distributions of the 80% voided case, RMS and maximum errors are reduced from 0.49% and 1.52% to 0.42% and 0.91%. The maximum pin peak errors occur in the pins between the Gd-bearing fuels and inter-assembly gap, due to the neighboring spectral transition effect. These improved results in pin power demonstrate that the new XS library generation procedure successfully reduces the bias originated from the current pin cell based XS library generation procedure.

Table 3.5 Variations to generate resonance cross section table for heterogeneous unitcell model

Case		1	2	3	4	5	6	7	8	9	10	11	12	13	14	15	16
Vol	fuel	1.0	1.0	1.0	1.0	1.0	1.0	1.0	1.0	1.0	1.0	1.0	1.0	1.0	1.0	1.0	1.0
	clad	1.0	1.0	1.0	1.0	1.0	1.0	1.0	1.0	1.0	1.0	1.0	1.0	1.0	1.0	1.0	1.0
	mod	1.0	1.0	1.0	1.0	1.0	2.0	5.0	5.0	5.0	5.0	5.0	5.0	5.0	5.0	5.0	5.0
Fuel	^{235}U	1.0	1.0	1.0	1.0	1.0	1.0	1.0	0.5	0.25	0.125	0.0625	0.03125	0.01	0.01	0.01	0.01
	^{238}U	1.0	1.0	1.0	1.0	1.0	1.0	1.0	0.5	0.25	0.125	0.0625	0.03125	0.01	0.001	1.0E-6	1.0E-7
	^{16}O	1.0	1.0	1.0	1.0	1.0	1.0	1.0	0.5	0.25	0.125	0.0625	0.03125	0.01	0.01	0.01	0.01
Mod	^{1}H	0.0025	0.2	0.5	0.75	1.0	1.0	1.0	1.0	1.0	1.0	1.0	1.0	1.0	1.0	1.0	1.0
	^{16}O	0.0025	0.2	0.5	0.75	1.0	1.0	1.0	1.0	1.0	1.0	1.0	1.0	1.0	1.0	1.0	1.0

Table 3.6 Variations to generate resonance cross section table for heterogeneous assembly model

Case		1	2	3	4	5	6	7
Mod	^{1}H	0.001	0.01	0.1	0.25	0.5	0.75	1.0
	^{16}O	0.001	0.01	0.1	0.25	0.5	0.75	1.0

Table 3.7 Eigenvalues and fission power errors of MPACT against MCNP6 solutions for assembly problems

Fuel	Remark	k_{eff} & Power								
		MCNP	MPACT with the current procedure				MPACT with the new procedure			
		k_{eff}	k_{eff}	Diff (pcm)	RMS (%)	Max (%)	k_{eff}	Diff (pcm)	RMS (%)	Max (%)
PWR	P2C	1.17352 (10)	1.17304	-48	0.37	0.86	1.17297	-55	0.36	0.70
BWR	40% VF	0.97138 (4)	0.97451	313	0.42	0.85	0.97381	243	0.42	0.81
GE-14	80% VF	0.94739 (4)	0.95110	371	0.49	1.52	0.95012	273	0.42	0.91

Chapter 4 Development of Double Heterogeneous Modelling Capability

Conventional HTGR and many of advanced rectors use TRISO (TRi-structural ISOtropic) fuel grains embedded in a ceramic or metal matrix. Many high-fidelity codes are being developed to accommodate double heterogeneity (DH) as interest in using particulate fuels in advanced reactors grows. These particulate fuels are characterized by the DH effect caused by randomly dispersed fuel particles in fuel compacts which are heterogeneously arranged in the core. Due to the disregard of spatial self-shielding in fuel particles, a simple volume-averaging would result in a considerable underestimation of the multiplication factor of thermal reactors. This DH effect should be accounted for in generating MG XSs by proper energy and spatial self-shielding of resonances. As a result, the high-fidelity modeling requires the development of a novel resonant self-shielding approach for processing the DH effect of particle fuels. SCALE-Polaris [6] is being developed by Oak Ridge National Laboratory (ORNL) as a new module of SCALE 6.2 to provide high-fidelity lattice physics analysis capability for LWR application. Polaris also employs the ESSM and SDESSM, which were implemented in MPACT. To accelerate the ESSM, the equivalent Dancoff factor cell (EDC) model [19] is being applied to the ESSM, which is called the cell Dancoff based embedded self-shielding method (Cell ESSM). With increased interests on advance reactors, one of SCALE-Polaris' next goals is to use the NRC core simulator PARCS [68] for prismatic HTGR analysis with the accurately processed self-shielded XS of double heterogeneous fuels.

This chapter aims to introduce a new XS library generation procedure for a double heterogenous fuel and to develop a consistent double heterogenous self-shielding capability in the

high-fidelity simulation. To obtain flux solutions and resulting effective XSs of the double heterogeneous fuel compact, the Hebert CPM method [69] is implemented in conjunction with the Cell ESSM of Polaris. The routines to calculate the collision probabilities in each layer of particles and a matrix are implemented in Polaris by referring the recent MC^2-3 updates [70] on the DH treatments. As a result, MC^2-3 and Polaris calculate the self-shielded and background XSs consistently.

In Section 4.1, the detailed methodologies and procedures of the double heterogeneous capability and Cell ESSM are given. Since the current simplified AMPX library of Polaris is generated using a heterogenous LWR pin cell, and accordingly is not adequate for the analysis of graphite moderated system, a new library generation procedure is discussed. New resonance tables for actinides and scattering matrices for graphite and light-weight materials were generated using MC^2-3 solution, which was successful in estimating the self-shielding effect of double heterogeneous fuel. The Polaris results with the new library and resonance treatment are compared with Serpent-2 reference solutions for prismatic-type HTGR fuel compact and HTR-10 single pebble problems in Section 4.2.

4.1 Cell-based Dancoff Equivalent Embedded Self-Shielding Method with Doubly Heterogeneous Fuel

4.1.1 Hebert CPM

This section describes the Hebert CPM method [69], which is implemented in MC^2-3. Hebert method directly performs the 1D fuel compact calculation with the XS of each layer of fuel particle and those of matrix in a fuel compact. To determine fluxes at each layer (hereafter, micro region) in a particle, collision probabilities in spherical geometry should be calculated as well as the one in surrounding cylindrical or spherical structure, such as matrix, moderator, and coolant

(hereafter, macro region). The Hebert CPM differs from the conventional CPM in terms of calculating homogenized XSs for the stochastic region and calculating collision probability between multiple micro and macro regions. The derivation of Hebert CPM starts from calculating the micro-region-to-micro-region within-particle collision probabilities, $P^{p}_{n,j\to n,i}$ using the conventional spherical CPM solver. It is noted that the following derivations and figures are taken from the reference [56] to describe the standard spherical CPM and Hebert CPM. Figure 4.1 illustrates the cross-sectional view of a 1D spherical shell geometry with a white boundary conditions.

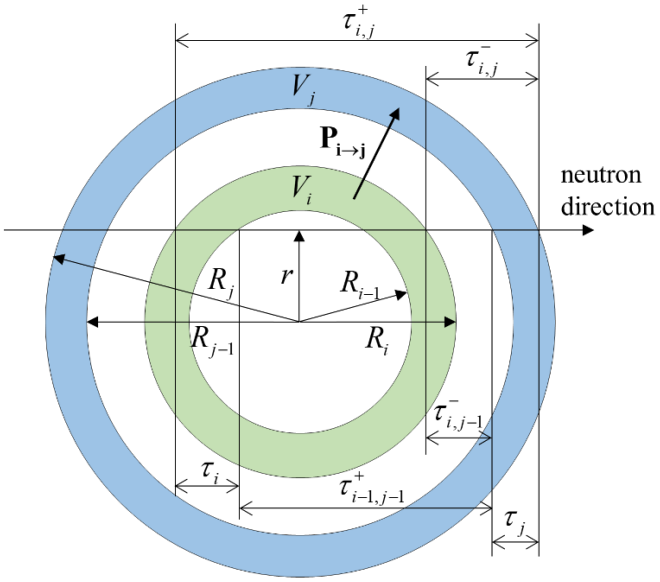

Figure 4.1 Cross sectional view of a spherical shell geometry taken from [56]

A shell-to-shell first flight collision probability can be calculated by counting the probabilities for mono-directed source neutrons in a hemisphere. According to the notation in Figure 4.1, the first flight probability can be calculated as

$$P_{i\to j}=\int_0^{R_i}\frac{1}{\Sigma_{t,i}V_i}\left(1-Exp\left(-\tau_i(r)\right)\right)Exp\left(-\tau^{+}_{i-1,j-1}(r)\right)\left(1-Exp\left(-\tau_j(r)\right)\right)2\pi r dr$$
$$+\int_0^{R_i}\frac{1}{\Sigma_{t,i}V_i}\left(1-Exp\left(-\tau_i(r)\right)\right)Exp\left(-\tau^{-}_{i,j-1}(r)\right)\left(1-Exp\left(-\tau_j(r)\right)\right)2\pi r dr, \tag{4.1}$$

where $\tau_i(r)$, $\tau_j(r)$, $\tau^{+}_{i-1,j-1}(r)$ and $\tau^{-}_{i,j-1}(r)$ are optical lengths shown in Eq. (4.1), which can be calculated as

$$\tau_k(r)=\begin{cases}\Sigma_{t,k}\left(\sqrt{R_k^2-r^2}-\sqrt{R_{k-1}^2-r^2}\right) & \text{for } r\le R_{k-1}\\ \Sigma_{t,k}\sqrt{R_k^2-r^2} & \text{for } R_{k-1}<r\le R_k\\ 0 & \text{for } R_k<r\end{cases}, \tag{4.2}$$

$$\tau^{-}_{i,j}(r)=\begin{cases}\sum_{k=i+1}^{j}\tau_k(r) & \text{for } i<j\\ 0 & \text{for } i\ge j\end{cases}, \tag{4.3}$$

$$\tau^{+}_{i,j}(r)=2\sum_{k=1}^{i}\tau_k(r)+\tau^{-}_{i,j}(r). \tag{4.4}$$

$$\begin{aligned}
&\tau^{+}_{i,j}(r)=\tau_i(r)+\tau^{+}_{i-1,j-1}(r)+\tau_j(r),\\
&\tau^{+}_{i,j-1}(r)=\tau_i(r)+\tau^{+}_{i-1,j-1}(r),\\
&\tau^{+}_{i-1,j}(r)=\tau^{+}_{i-1,j-1}(r)+\tau_j(r),\\
&\tau^{-}_{i-1,j}(r)=\tau_i(r)+\tau^{-}_{i,j-1}(r)+\tau_j(r),\\
&\tau^{-}_{i-1,j-1}(r)=\tau_i(r)+\tau^{-}_{i,j-1}(r),\\
&\tau^{-}_{i,j}(r)=\tau^{-}_{i,j-1}(r)+\tau_j(r).
\end{aligned} \tag{4.5}$$

where $[R_{k-1},R_k]$ is the subdivided integration range of the integration range $[0,R_i]$. The number of subdivisions is set to the number of intervals for a shell k by default, and can be increased by a user input.

Similarly, the first flight self-collision probability $P_{i\to i}$ is calculated as

$$P_{i\to i} = \int_0^{R_i} \frac{1}{\Sigma_{t,i} V_i} \left(1 - Exp\left(-\tau_i(r)\right)\right) Exp\left(-\tau^+_{i-1,i-1}(r)\right) \left(1 - Exp\left(-\tau_i(r)\right)\right) 2\pi r dr + \int_0^{R_i} \frac{2}{\Sigma_{t,i} V_i} \left(\tau_i(r) + Exp\left(-\tau_i(r)\right) - 1\right) 2\pi r dr, \tag{4.6}$$

Using the subdivided integration range $[R_{k-1}, R_k]$, the integration of Eq. (4.1) and (4.6) can be rewritten as

$$P_{i\to j} = \frac{1}{\Sigma_{t,i} V_i} \sum_{k=1}^{i} \int_{R_{k-1}}^{R_k} \left(\tilde{S}_{i,j}(r) + \tilde{S}_{i-1,j-1}(r) - \tilde{S}_{i-1,j}(r) - \tilde{S}_{i,j-1}(r)\right) dr, \tag{4.7}$$

where $\tilde{S}_{i,j}(r) = 2\pi r \left(Exp\left(-\tau^+_{i,j}(r)\right) - Exp\left(-\tau^-_{i,j}(r)\right)\right)$.

$$P_{i\to i} = \frac{1}{\Sigma_{t,i} V_i} \sum_{k=1}^{I} \int_{R_{k-1}}^{R_k} S_i(r) dr, \tag{4.8}$$

where $S_i(r) = 2\pi r \left\{\left(1 - Exp\left(-\tau_i(r)\right)\right)^2 Exp\left(-\tau^+_{i-1,i-1}(r)\right) + 2\left(\tau_i(r) + Exp\left(-\tau_i(r)\right) - 1\right)\right\}$. Integration over each sub-interval of Eq. (4.7) and (4.8) were done using the Gauss-Jacobi quadrature in this implementation.

In the Hebert CPM [69], the shell-to-shell within-particle collision probabilities $P^p_{n,j\to n,i}$ and particle escape probabilities from individual shells $E^p_{n,i}$ are calculated for each type of stochastic region. *n* and *i, j* are indices for a particle type and a shell and the superscript *p* means the particle quantity. Subscript 0 indicates the matrix. Then, the homogenized XSs are calculated for each type of stochastic region as follow.

$$\tilde{\Sigma} = v_0 \Sigma_{t,0} + \sum_{n=1}^{N} \sum_{i=1}^{I_n} v_{n,i} \Sigma_{t,n,i} E^p_{n,i}, \tag{4.9}$$

Using existing procedures to compute collision probability for non-stochastic regions, these homogenized XSs are utilized to determine macro-region-to-macro-region collision probabilities.

By assuming the spatial self-shielding factor of $\frac{E_{n,i}^{p,\alpha}}{E_{n,i}^{p,\alpha}(\Sigma_{t,0}^{\alpha})}$, where $E_{n,i}^{p,\alpha}(\Sigma_{t,0}^{\alpha})$ is the particle escape probability from *i*'th layer of particle type *n* with the replacement of actual particle XSs with the matrix XS, a homogenized XS for each macro region is calculated as

$$\Sigma_h^{\alpha} = v_0^{\alpha}\Sigma_{t,0}^{\alpha} + \sum_{n=1}^{N_{\alpha}}\sum_{i=1}^{I_n^{\alpha}} v_{n,i}^{\alpha}\frac{E_{n,i}^{p,\alpha}}{E_{n,i}^{p,\alpha}(\Sigma_{t,0}^{\alpha})}\Sigma_{t,n,i}^{\alpha}. \tag{4.10}$$

Macro to macro region collision probabilities $P_h^{\alpha\to\beta}$ are calculated using these homogenized XSs. Within the same macro region, the matrix-to-matrix collision probability is calculated using the self-collision probability $P_h^{\alpha\to\alpha}$ as

$$P_{0\to 0}^{\alpha\to\alpha} = \frac{v_0^{\alpha}\Sigma_{t,0}^{\alpha}}{\tilde{\Sigma}^{\alpha}}\left(1-\frac{\Sigma_h^{\alpha}}{\tilde{\Sigma}^{\alpha}}(1-P_h^{\alpha\to\alpha})\right). \tag{4.11}$$

Once this matrix-to-matrix collision probability between different macro regions are calculated, the other collision probabilities can be obtained as

$$P_{n,i\to 0}^{\alpha\to\beta} = E_{n,i}^{p,\alpha}P_{0\to 0}^{\alpha\to\beta}, \tag{4.12}$$

$$P_{n,i\to 0}^{\alpha\to\beta} = E_{n,i}^{p,\alpha}P_{0\to 0}^{\alpha\to\beta}, \tag{4.13}$$

$$P_{n,i\to m,l}^{\alpha\to\beta} = E_{n,i}^{p,\alpha}P_{0\to m,l}^{\alpha\to\beta}. \tag{4.14}$$

Using all collision probabilities obtained, the following non-linear coupled system of equations are iteratively solved.

$$\begin{aligned} V_{n,i}^{\alpha}\Sigma_{t,n,i}^{\alpha}X_{m,l\to n,i}^{\beta\to\alpha} &= \sum_{\gamma}\sum_{q=0}^{N_{\gamma}}\sum_{j=1}^{I_q^{\gamma}} V_{q,j}^{\gamma}\Sigma_{s,q,j}^{\gamma}X_{m,l\to q,j}^{\beta\to\gamma}P_{q,j\to n,i}^{\gamma\to\alpha} + V_{m,l}^{\beta}P_{m,l\to n,i}^{\beta\to\alpha}, \\ V_{n,i}^{\alpha}\Sigma_{t,n,i}^{\alpha}Y_{n,i}^{\alpha} &= \sum_{\gamma}\sum_{q=0}^{N_{\gamma}}\sum_{j=1}^{I_q^{\gamma}} V_{q,j}^{\gamma}\Sigma_{s,q,j}^{\gamma}Y_{q,j}^{\gamma}P_{q,j\to n,i}^{\gamma\to\alpha} + \gamma_{n,i}^{\alpha}, \end{aligned} \tag{4.15}$$

where $\Sigma_{s,q,j}^{\gamma}$ is the self-scattering XS in a shell j of particle q or a matrix (q=0, j=1) in macro-region γ, $X_{m,l\to n,i}^{\beta\to\alpha}$ is the flux in micro-region n, i of macro-region α due to a unit source density in micro-region m, l of macro-region β and $Y_{n,i}^{\alpha}$ is the flux in micro-region n, i of macro-region α due to a unit external incoming neutron current from the system boundary surface. $\gamma_{n,i}^{\alpha}$ is the first flight blackness of micro-region n, i of macro-region α defined by

$$\gamma_{n,i}^{\alpha}=\frac{4V_{n,i}^{\alpha}}{S_B}\Sigma_{t,n,i}^{\alpha}\left(1-\sum_{\beta}\sum_{m=0}^{N_\beta}\sum_{l=1}^{I_m^\beta}P_{n,i\to m,l}^{\alpha\to\beta}\right), \tag{4.16}$$

where S_B is the surface area of the system boundary. An albedo boundary condition is applied to $Y_{n,i}^{\alpha}$ and $X_{m,l\to n,i}^{\beta\to\alpha}$ as

$$Y_{n,i}^{\alpha}(a)=\frac{Y_{n,i}^{\alpha}}{1-(1-\Gamma)a},\ \text{where}\ \Gamma=\sum_{\beta}\sum_{m=0}^{N_\beta}\sum_{l=1}^{I_m^\beta}\Sigma_{r,m,l}^{\beta}V_{m,l}^{\beta}Y_{m,l}^{\beta}, \tag{4.17}$$

$$X_{m,l\to n,i}^{\beta\to\alpha}(a)=X_{m,l\to n,i}^{\beta\to\alpha}+ax_{m,l}^{\beta}Y_{n,i}^{\alpha}(a),\ \text{where}\ x_{m,l}^{\beta}=\frac{S_B}{4}V_{m,l}^{\beta}Y_{m,l}^{\beta}. \tag{4.18}$$

Here, a is the albedo, Γ is the total absorption blackness of the problem domain and $x_{m,l}^{\beta}$ is the number of neutrons to reach the problem domain boundary without any collision from a unit source density in micro-region m, l of macro-region β. Then, flux solutions are obtained by Eq. (4.19) without any inner iteration in the transport calculation as

$$\phi_{n,i}^{\alpha}=Y_{n,i}^{\alpha}(a)j_{ext}^{-}+\sum_{\beta}\sum_{m=0}^{N_\beta}\sum_{l=1}^{I_m^\beta}X_{m,l\to n,i}^{\beta\to\alpha}(a)Q_{m,l}^{\beta}, \tag{4.19}$$

where j_{ext}^{-} is the external incoming current from the system boundary and $Q_{m,l}^{\beta}$ is the density of neutron sources excluding the self-scattering source in micro-region m, l of macro-region β.

4.1.2 Cell ESSM with the Hebert CPM

Despite multiple attempts to model the double heterogeneous fuel in transport solvers, none has extended its usage to the XS library generation using the heterogeneous model and the subsequent resonance treatment of the high-fidelity simulation. As mentioned in the section 1.2.2, the background XSs need to be estimated consistently in the heterogenous table generation and the resonance calculation. The most straightforward approach to treat the DH is an incorporation of the 2D DH treatment method into transport calculations in both library generation and resonance treatment procedure. However, the resonance calculation with DH treatment requires additional computing time, which limits the practical design applications of large and complex geometries in a fuel assembly. To achieve highly accurate resonance calculations for a double heterogenous fuel with relatively short computation time, a novel resonance treatment method is developed by coupling the Hebert CPM with the existing Cell ESSM capability of Polaris.

While the heterogeneous model in the XS library generation procedure provides an accurate resonance treatment in high-fidelity simulation, solving the fixed source problem in Eq. (3.1) over the whole spatial domain at each group is time-consuming. To reduce the computational time in the fixed source calculation, the equivalent Dancoff factor cell (EDC) model was initially proposed for the subgroup method [19]. The key idea of EDC model is to generate a set of analogous 1D cylindrical problems for each fuel pin cell by keeping the Dancoff correction factor same. The Dancoff factor and equivalent cell were determined by solving a one group fixed source problem. Since solving a 1D cylindrical problem using the CPM solver is easier than solving a 2D lattice problem using the MOC solver, the computational time reduces significantly in the resonance treatment of high-fidelity simulation. This approach was extended to produce the heterogeneous RI table for the ESSM by incorporating the EDC model [71]. Recently, the EDC

model is also applied to the ESSM (Cell ESSM) in Polaris and being verified using multiple LWR benchmark problems [72]. Since Cell ESSM is designed to solve the 1D cylindrical problem using the standard CPM solver, the double heterogeneity in cylindrical fuel can be easily incorporated by replacing the existing CPM routine with the Hebert CPM.

The main objective of the Cell ESSM method for double heterogeneous fuel (Cell ESSM-DH, hereafter) is to provide homogenized self-shielded fuel compact XSs for subsequent lattice calculations. In the Cell-ESSM-DH stage, the lattice geometry is converted into the equivalent cell geometry using the Dancoff factor estimated by the fixed source calculation. Then, the background XSs of each micro-region (individual layers of particles and graphite matrices) are determined by solving the 1D Hebert CPM fixed source calculation. Since the background XS is prepared for each micro-region, the corresponding XSs should be homogenized by considering the spatial flux distribution within fuel compact. For that, the homogenization factor (disadvantage factor) is defined as

$$d^{i}_{X,g} = \frac{\sum_{n'=1}^{N}\sum_{k=0}^{N}\sum_{i\in k} N^{i[k]}_{n'}\sigma^{i}_{X,g,n'}\phi^{[k]}_{g,n'}}{\tilde{N}^{i}_{\mathrm{hom}}\tilde{\sigma}^{i}_{X,g}\tilde{\phi}_{g}} \cong \frac{\phi^{[k]}_{g,n'}}{\tilde{\phi}_{g}} \tag{4.20}$$

where k is a particle or matrix index, i is an isotope index, $\phi^{[k]}_{g,n}$ and $\tilde{\phi}^{[k]}_{g}$ are the particle or matrix flux and the flux averaged over the particle and the matrix, respectively.

After the Cell ESSM-DH step, the flux of each micro and macro region is determined through the Hebert CPM slowing down calculation. Note that the fixed source calculation in the Cell-ESSM-DH stage is the ESSM calculation in Eq. (3.1), while the slowing down calculation in the second step is the transport calculation in Eq. (1.1). Calculated fluxes are used to obtain the disadvantage factor. Then finally, the effective homogenized the XS for fuel matrix is obtained using the background XSs and the disadvantage factors. Figure 4.2 shows the pseudocode for the

Cell ESSM-DH, which follows the original Cell ESSM calculation procedure with the additional routines with the Hebert CPM.

```
Fixed source calculation (Cell ESSM-DH)
! Purpose : 1) Obtain converged background cross section
!           2) Obtain disadvantage factor to homogenize doubly heterogeneous fuel
Prepare variables for Hebert CPM
for each cell
    for each material region
        Prepare geometry and collision probability variables
        for each ESSM iteration
            calculate XSs using background XS
            calculate Collision probability, X and Y with the white boundary condition
            perform fixed source Hebert CPM calculation
            calculate escape XS using the CPM solution
        endfor
  endfor
endfor
save background XS for the MOC lattice calculation
perform Hebert CPM slowing down calculation
calculate disadvantage factor using the CPM solution for the lattice calculation
```

Figure 4.2 Pseudocode of Cell ESSM for double heterogeneous fuel

4.1.3 Library generation for double heterogeneous fuel

The new heterogeneous RI table and graphite scattering matrices are generated using MC^2-3. MC^2-3 has recently been updated to treat the particulate fuel based on three methods [56]: iterative local spatial self-shielding approach, Sanchez-Pomraning [22], and Hebert methods. Since the Hebert CPM in MC^2-3 was implemented only for the spherical geometry, related routines are extended to the cylindrical geometry for the consistency between the Hebert CPM calculations in MC^2-3 and Polaris. Polaris uses the same simplified AMPX library of MPACT prepared for the LWR application. Its application to a graphite-moderated reactor is limited because of the different base weighting spectrum, pin cell geometry, and the approximations used in the library generation.

Different weighting spectrum induces a non-negligible bias not only in the RI table, but also in the scattering transfer matrix, and thus the current XS library is no longer adequate for the analysis of HTGR and HTR. Therefore, the RI table and graphite scattering matrices of the current AMPX XS library are adjusted using the ultrafine group Hebert CPM solution of MC^2-3 in the same manner as the MPACT library generation procedure in section 3.1.2 to save time.

To adequately account for the DH effect, the background XSs can be varied by adjusting various design parameters. However, it is unclear to determine the functionalization parameter to change the background XS for double heterogeneous fuel due to the different physics applied to micro- and macro-regions. Since the graphite density does not change noticeably, the previous functionalization parameter, moderator density, is no longer a proper choice in the XS library generation. Thus, further investigation is needed to examine the effect of various design parameters (e.g., packing fraction, particle size, compact radius, graphite layer size, and fuel to moderator ratio etc.). Although it is possible to generate multiple problem-dependent library, a preliminary XS library is generated by changing the packing fraction in order to test a new fuel self-shielding capability of double heterogeneous fuel for the high-fidelity simulation. MC^2-3 is modified to allow the users to choose the parameters for the variation of background cross sections.

While the MPACT code is modified to handle the scattering matrices as a function of background XS, the Polaris code remains unchanged with the original simplified AMPX library format. As a result, the fixed scattering transfer matrix at certain background XS are used in the analysis. Figure 4.3 illustrates above MG XS lbirary generation procedure of doubly heterogeneous fuel for high-fidelity simulation using MC^2-3. Note that the generalized condensed scheme was not used to generate new library because only pin cell benchmarks were solved in the verification tests. Fifteen different packing fractions as well as the infinite dilute case are used in

the new library generation with the explicit cylindrical compact and spherical pebble reference geometries. Graphite matrix is also generated using the 37.8% packing fraction of each problem.

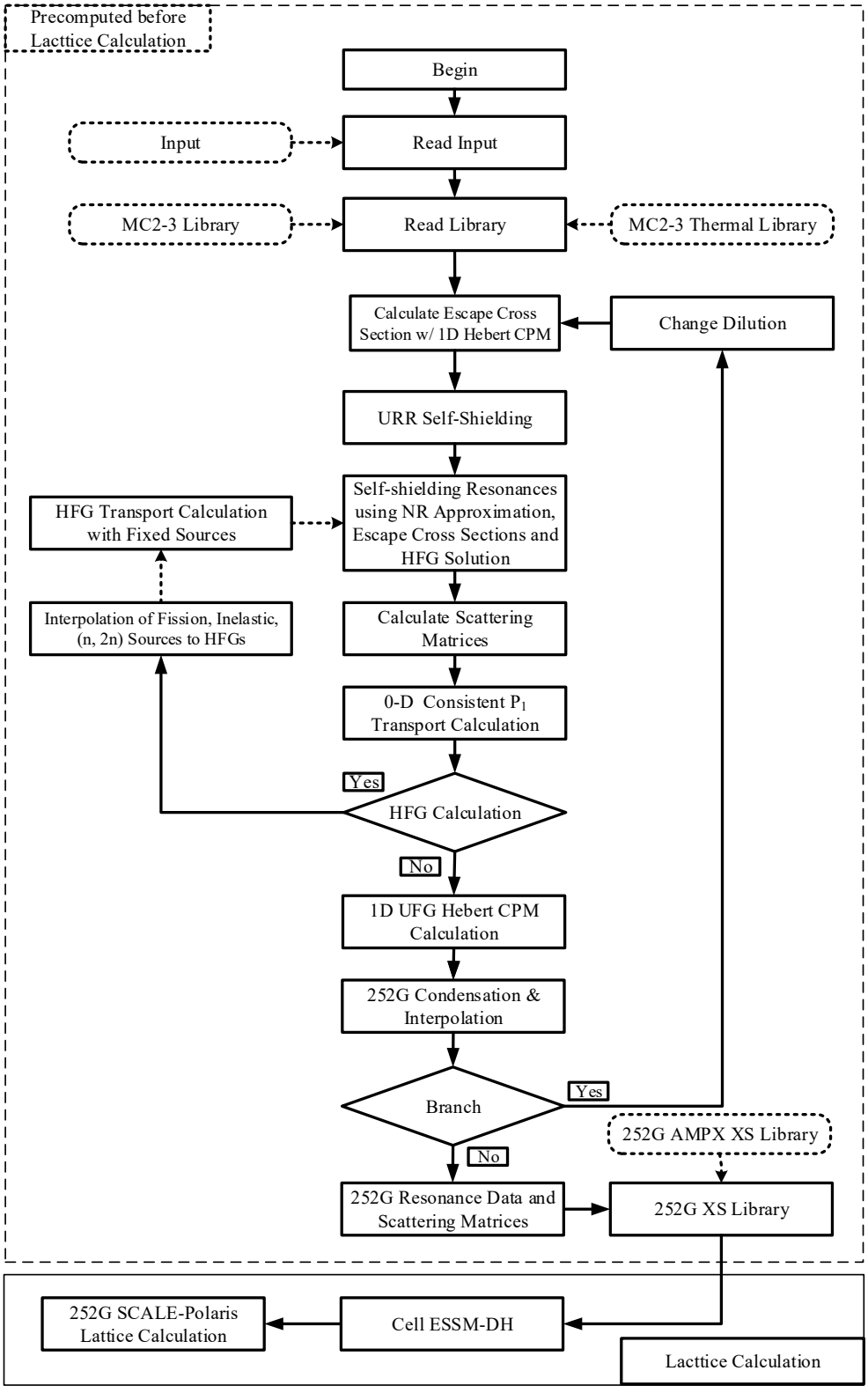

Figure 4.3 MG XS lbirary generation procedure of doubly heterogeneous fuel for high-fidelity simulation using MC^2-3

4.2 Numerical Tests with New Double Heterogeneous Cross Section Library

Benchmark calculations were performed by Polaris with the simplified AMPX 252-group library based on ENDF/B-VII.1 for the infinite fuel compact problem and pebble problem. Infinite fuel compact benchmark problems were developed based on the TRISO particle data of the NGNP design that uses 10.36 wt.% UCO fuel. Fuel compact design parameters are determined by referring the typical prismatic HTGR hexagonal pin cell with the compact radius of 0.6225 cm and the flat-to-flat distance of 1.8796 cm. A single pebble design was derived from the HTR-10 [73] design that uses 17 wt.% UO_2 fuel TRISO surrounded by a graphite layer and helium coolant. The pebble is composed of a fuel zone of 2.5 cm radius that has fuel particles dispersed in a graphite matrix and an outer graphite layer of 0.5 cm thickness. Since Polaris does not support the hexagonal or cylindrical model with the white boundary condition, the square outer boundary of fuel compact or pebbles is assumed with the reflective boundary condition at the cube surfaces. Table 4.1 provides the brief TRISO data used in the verification tests and the detailed information can be found in [54]. Since Polaris MOC lattice solver does not have a capability to handle the random distribution of pebbles, only a single pebble is solved using the 1D Hebert CPM for the benchmark test. Figure 4.4 illustrates the TRISO and cylindrical fuel compact or spherical pebble designs used in the verification tests.

Table 4.1. TRISO data obtained from the typical HTGR design

Region	Radius (cm)	Material	Density (g/cm3)
Fuel Kernel	0.0175	UCO (10.36 wt.%)	10.5
Buffer	0.0275	Carbon	1.00
Inner PyC	0.0310	Pyrolytic carbon	1.90
SiC	0.0345	Silicon carbide	3.20
Outer PyC	0.0385	Pyrolytic carbon	1.90
Fuel Compact	0.6225	Graphite	1.20
Gap	0.6350	He	0.0032
Block	0.8746 (cube)	Graphite	1.74

Table 4.2 Pebble data obtained from the HTR-10 design

Region	Radius (cm)	Material	Density (g/cm3)
Fuel Kernel	0.0250	UO_2 (17 wt.%)	10.4
Buffer	0.0340	Carbon	1.00
Inner PyC	0.0380	Pyrolytic carbon	1.90
SiC	0.0415	Silicon carbide	3.20
Outer PyC	0.0455	Pyrolytic carbon	1.90
Fuel Zone	2.5	Graphite	1.73
Graphite Layer	3.0	Graphite	1.84
Coolant	4.0	Helium	0.0032

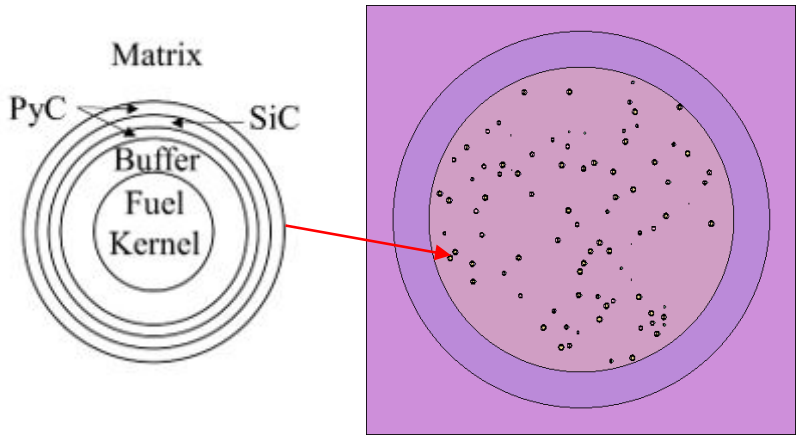

Figure 4.4 NGNP TRISO design (left) and fuel compact/pebbel models (right)

4.2.1 Library examination for double heterogeneous fuel

Before testing the new feature of Polaris, it is worthwhile to examine the accuracy of the new XS libraries. The homogenized fuel compact problem in Figure 4.4 with the 37.8% packing fraction was solved using the original simplified 252-group AMPX library. The reactivity difference against the Serpent-2 is 479 pcm, and detailed reaction rate comparison in each group reveals that the main error sources of reactivity discrepancies are due to the errors of ^{235}U, ^{238}U resonance XSs and graphite scattering matrices. To resolve the bias, a new XS library is generated

by replacing the resonance XSs of ^{235}U and ^{238}U and the graphite scattering matrix are replaced with the one from MC^2-3 (NGNP library). Figure 4.5 compares the 252-group neutron spectra obtained from Polaris with the new NGNP library and the Serpent-2 code. The NGNP library generated from the MC^2-3 can accurately reproduce the reference Serpent-2 solution. Figure 4.6 shows the comparison of self-shielded ^{238}U absorption XS with different background XSs for the group including 6.67 eV resonance between the current and new NGNP libraries. As shown in the figure, the magnitude of self-shielding effect of graphite moderated system are totally different from the one in PWR system at most background compositions. This indicates that the current AMPX library generation procedure is not adequate for the graphite moderated system analysis, and the NGNP library generated from the MC^2-3 can reproduce the reference Serpent-2 solution accurately.

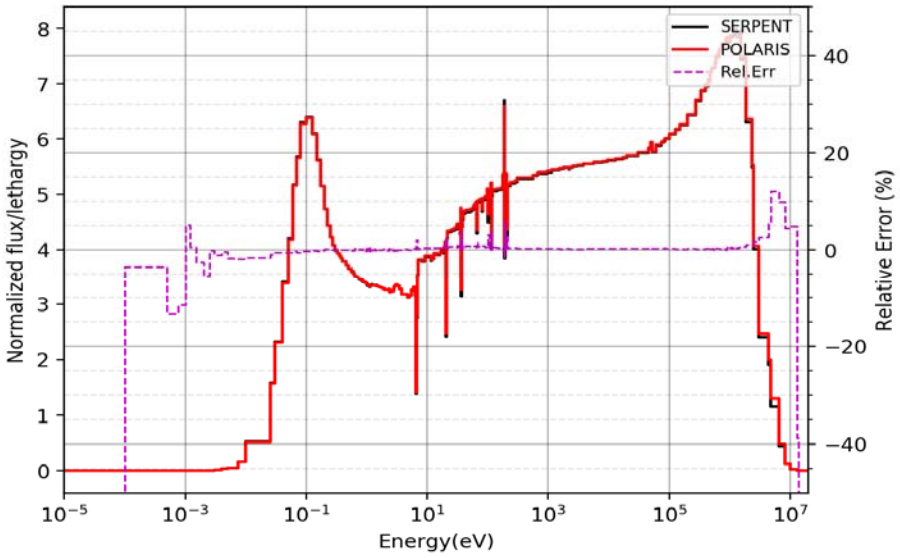

Figure 4.5 Comparison of flux spectrum in fuel between Polaris with the new library and Serpent-2

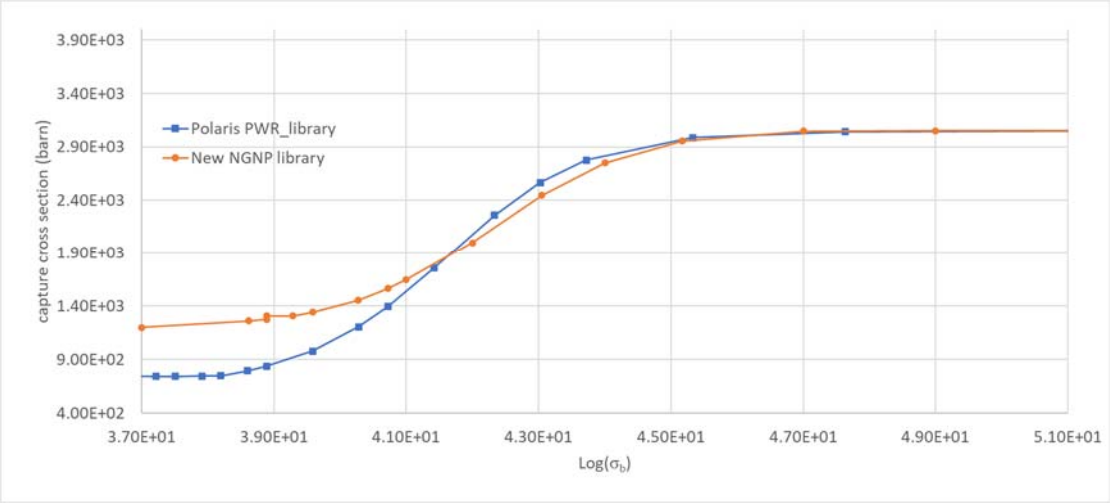

Figure 4.6 Comparison of self-shielded absorption cross section with different background cross sections for the 6.67 eV resonance of ^{238}U between original and NGNP libraries

4.2.2 Fuel compact cell and pebble benchmark results

With the new 252-group NGNP library, the infinite compact and pebble problems were solved again by varying packing fractions, particle size and graphite layer (moderator) size for the verification of Cell ESSM-DH performance. In the parametric test, the infinite compact problem of a 0.0385 cm particle size, 37.8% packing fraction, 0.8746 cm graphite matrix, and the single pebble problem of a 0.0455 cm particle size, 37.8% packing fraction, 3.0 cm graphite layer are used as initial parameters for comparison. The internal dimensions of particles were determined to preserve volume ratios of micro-regions in a particle. Reference Serpent-2 MC calculations were performed with 1,000 active cycles and 100,000 histories per cycle to yield relative errors of reaction rates less than 0.3% for each case. As Serpent-2 does not support the spherical surface as the outer boundary, the rectangular array was used by preserving the volume of helium coolant. Table 4.3 shows the different design parameters used for the verification tests. Table 4.4 shows

the number of particles in the fuel zone used in the Serpent-2 simulations for each case to achieve a desired packing fraction.

Table 4.3 Different parameters for parametric study

Parameter (Controlled parameters)	Abbreviation	Compact	Pebble
Particle radius (cm) (PF4, CS2)	PR1	0.0200	0.0200
	PR2	0.0385	0.0455
	PR3	0.0770	0.0770
Packing fraction (%) (PR2, CS2)	PF1	2.0	2.0
	PF2	10.0	10.0
	PF3	19.9	19.9
	PF4	37.8	37.8
	PF5	57.8	50
Graphite layer size (cm) (PR2, PF4)	CS_1	0.70	2.7
	CS_2	0.87	3.0
	CS_3	1.20	3.5

Table 4.4. The number of TRISO particles used in Serpent-2 calculation for eight cases

Case	PR1	PR2	PR3	PF1	PF2	PF3	PF4	PF5
Compact	24020	3367	421	178	891	1773	3367	5149
Pebble	218750	62701	12937	3318	16588	33009	62701	82938

Table 4.5 shows the calculated reactivities and DH effects of Polaris for the HTGR fuel compact, compared to those of Sepent-2 in a unit of pcm. The Cell ESSM-DH approach catches the DH effect accurately through PF1 to PF5. The reactivity difference can be up to 366 pcm for lower packing fractions, while it shows the best accuracy with higher packing fractions. As the packing fraction decrease, eigenvalue increases due to increasing neutron moderation to thermal energy even though the amount of fuel decreases. This results in a softened spectrum, which indicates that the target flux spectrum deviates significantly from the original weighting spectrum. As already noted from the results of Figure 4.5, the weighting spectrum significantly affects the accuracy of graphite scattering matrix. The similar phenomenon is observed in the CS3 case with

the increased moderator amount. On the other hand, it turned out that the modeling difference in particle radius causes the reactivity bias easily about 458 pcm for the PR1 case. Pebble cases in Table 4.6 show similar, but better results compared to the HTGR compact problems overall, except for the CS1 case that has the small amount of graphite layer for moderation.

As the particle size increases, the eigenvalue increases due to large spatial self-shielding in particles and resonance escape probability through the matrix. Since the resonance XSs in the NGNP library are tabulated only with the different packing fractions, these effects are not well captured in the self-shielding curve of Figure 4.6. In addition, the XS and scattering matrix errors of other nuclides, and assumptions made in the library generation should be addressed in the further investigation to demonstrate the remaining bias in the results. However, despite of the incompleteness of the new NGNP library, this numerical result supports that the Cell ESSM-DH predicts the heterogeneity effect similarly compared to the Serpent-2 solutions.

Table 4.5 Reactivity and double heterogeneity effects between two calculations for HTGR fuel compact

Case	Serpent-2			Polaris			DH effect Error (2)-(1)
	Reactivity[b]		DH effect (1)	k- Reactivity		DH effect (2)	
	Hom	Het		Hom	Het		
PR1	1.29209	1.32561	1957	1.29243	1.33407	2415	458
PR2[a]	1.29209	1.34924	3278	1.29243	1.34747	3161	-117
PR3	1.29209	1.39931	5930	1.29243	1.39522	5700	-230
PF1	1.51704	1.55650	1671	1.52045	1.55155	1318	-353
PF2	1.54350	1.63518	3632	1.54212	1.62391	3266	-366
PF3	1.43086	1.51262	3778	1.43337	1.50897	3495	-282
PF4[a]	1.29209	1.34924	3278	1.29243	1.34747	3161	-117
PF5	1.20146	1.23728	2410	1.20511	1.23986	2326	-84
CS1	1.13001	1.16984	3013	1.13174	1.16941	2846	-167
CS2[a]	1.29209	1.34924	3278	1.29243	1.34747	3161	-117
CS3	1.61913	1.69680	2827	1.62842	1.69364	2365	-462

a) this indicates the reference problem
b) standard deviation of Serpent-2 calculation is less than 8 pcm

Table 4.6 Reactivity and double heterogeneity effects between two calculations for HTR-10 pebble problem

Case	Serpent-2			Polaris			DH effect Error (2)-(1)
	Reactivity		DH effect (1)	k- Reactivity		DH effect (2)	
	Hom	Het		Hom	Het		
PR1	1.16766	1.19899	2238	1.16814	1.20446	2582	344
PR2[a]	1.16766	1.21111	3072	1.16814	1.21199	3097	25
PR3	1.16766	1.23592	4730	1.16814	1.23503	4636	-94
PF1	1.68970	1.77949	2986	1.69034	1.77209	2729	-257
PF2	1.43038	1.56095	5848	1.43109	1.55509	5572	-276
PF3	1.27923	1.37117	5242	1.28084	1.37583	5390	149
PF4[a]	1.16766	1.21111	3072	1.16814	1.21199	3097	25
PF5	1.13917	1.16614	2030	1.14026	1.17102	2304	273
CS1	1.09334	1.13013	2977	1.09520	1.13841	3466	488
CS2[a]	1.16766	1.21111	3072	1.16814	1.21199	3097	25
CS3	1.34248	1.38056	2055	1.34545	1.38010	1866	-189

a) this indicates the reference problem
b) standard deviation of Serpent-2 calculation is less than 8 pcm

Chapter 5 Development of Multigroup Gamma Data Generation Scheme for Heat Generation Rate Calculation

In reactor analysis, generating consistent XS sets for coupled neutron and gamma transport calculation is an important objective in addressing the issue of gamma heating in non-fuel components. To meet the target accuracies for Generation-IV (Gen-IV) neutronics characteristics, the assumption that all fission energy is locally deposited is no longer valid, with the target uncertainty for gamma heating set at 16 % for viability design studies and 10 % for performance design studies [74]. The impact of global gamma transport is well known to cause the distribution of energy deposition in a reactor to diverge considerably from the fission rate distribution. Most recent neutronic simulators use combined neutron and gamma heating computations to evaluate an accurate distribution of neutron and gamma heating rates. For example, the 2D and 2D/1D gamma transport calculation capabilities are recently implemented in MPACT for the gamma heating estimation [75]. For fast reactor applications, a new coupled neutron and gamma heating calculation procedure [76] has been developed based on VARIANT transport calculations by improving the existing ANL coupled neutron and gamma heating procedure [23]. In these calculations, the gamma source distribution is first calculated using precomputed neutron flux distribution and gamma production XSs, and then the gamma flux distribution is determined by solving a fixed-source gamma transport problem with this gamma source distribution. Consistently, a capability to generate gamma production data and interaction XS was implemented to the MG XS generation procedure. As mentioned in Chapter 3, the MPACT 51 group XS libraries

have been developed including the 19 group gamma data [77]. MC^2-3 code included a 21-group gamma library generated by the NJOY code [26].

However, those gamma data are restricted to the coarse group generated by the XS processing code, which does not account for the self-shielding effect of KERMA (Kinetic Energy Released in Material) factor, and does not include the delayed gamma production data. In addition, the gamma transport effect was approximated by using an arbitrary spectrum in MG processing. As a result, the relative errors in power density are particularly large in structural material where the gamma heating is dominant. In order to address these shortcomings of the existing gamma heating calculation, a new procedure to generate general gamma XS libraries with refined gamma energy structure was developed as part of this dissertation work to that include the delayed gamma production and kinetic energy release per reaction data. The self-shielding effect on the KERMA factor is considered by combining kinetic energy release per reaction data with the self-shielded XS of MC^2-3. This chapter covers the new gamma data generation procedure, which was built to produce a new MC^2-3 gamma library and to calculate the heating in the subsequent transport calculation.

5.1 Generation of Intermediate Group Gamma Data

5.1.1 Generation of gamma interaction cross section

The utility program PreMCS and GenMCS to developed to generate the MC^2-3 libraries in the thermal energy range were modified for gamma library generation. The PreMCS code developed to prepare an input file of NJOY for the multigroup neutron XS, the neutron heating factor, the photon production matrix was modified to prepare the multigroup gamma interaction XS, and the gamma heating factor. PreMCS also calculates the delayed components that include the kinetic energy from beta particles and the delayed gamma production XS. GenMCS reads

NJOY outputs for the prompt components and writes them into the MC^2-3 library format. The new gamma libraries are based on 2,082 neutron and 94 gamma groups. The group structures were selected based on the MC^2-3 neutron ultrafine group structure and the 94 gamma group structure of the Cross Section Evaluation Working Group (CSEWG) [25]. The 94-group structure covers the energy range from 5 keV to 20 MeV, and it is considered sufficiently fine since gamma XSs are smooth in most energy range important for gamma heating calculation. The overall procedure is described in Figure 5.1.

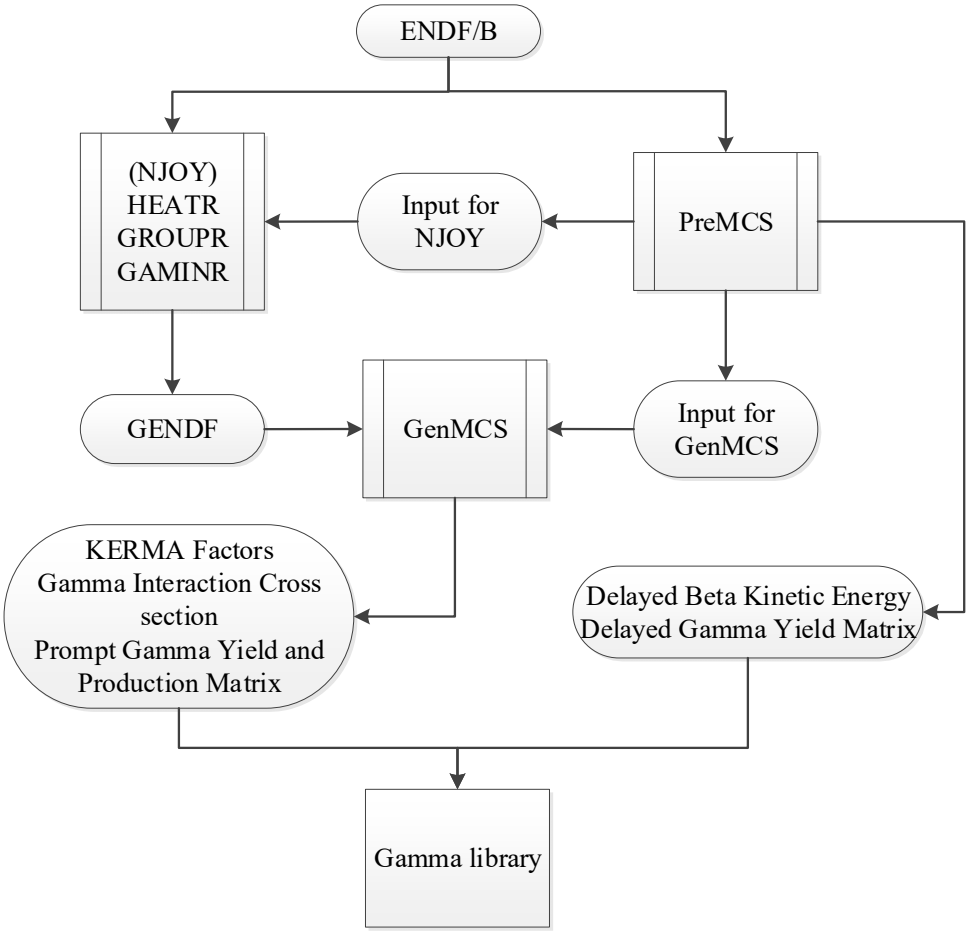

Figure 5.1 Procedure to prepare the gamma libraries of MC^2-3

5.1.2 Generation of self-shielded production yield matrix and KERMA factor

In the new gamma library generation procedure, the GROUPR module of NJOY generates neutron-photon production matrix by combining the data in the ENDF files. The PreMCS code first checks the availabilities of these file numbers for each isotope, and then prepares the input files for the NJOY runs in such a way that those files are properly coordinated in the production matrix generation. The photon production XSs generated in the 2,082 neutron group structure through the NJOY calculations are not self-shielded because the XSs are condensed at the infinite dilute condition. The use of unshielded photon production XSs in the gamma source calculation would yield over-estimated gamma production rates for capture and fission reactions. In addition, these production rates are inconsistent with the actual reaction rates obtained from a neutron transport calculation because the self-shielded capture and fission XSs prepared by MC^2-3 are used in the neutron transport calculation. In order to resolve this inconsistency problem, the gamma production XSs for capture and fission reactions are converted into a yield matrix by dividing the production XS by the infinite dilute neutron XS. Later, the self-shielded production XSs for capture and fission reactions are calculated in MC^2-3 by multiplying the yield matrices with self-shielded XSs. For non-elastic neutron reactions, the production matrices are directly provided in the gamma library and utilized without the intermediate process.

A KERMA factor is defined as an averaged kinetic energy release per reaction times a XS [25]:

$$k_{ij}(E) = \sum_{l} \bar{E}_{ijl}(E)\sigma_{ij}(E) \tag{5.1}$$

where $\overline{E_{ijl}}$ is the total kinetic energy carried away by the l^{th} species of secondary particles, and σ_{ij} is the XS for material i and reaction j. The neutron KERMA factors are calculated in the HEATR

module of NJOY as a PW XS. However, since only a few materials have the exact total kinetic energy data carried away by the secondary particles in their library, NJOY computes KERMA factors by the energy-balance method [25]:

$$k_{ij}(E) = (E + Q_{ij} - \overline{E}_{ijn} - \overline{E}_{ijr})\sigma_{ij}(E) \tag{2}$$

where $\overline{E}_{ijn}$ and $\overline{E}_{ij\gamma}$ are the total energy of secondary neutron including multiplicity and that of photon including multiplicity, respectively. In the energy-balance method, the negative neutron heating may appear in some cases due to the inconsistent data set of neutron and photon. Even though the energy-balance method could induce unphysical negative values in the process, it is applicable to the heat calculation since the negative KERMA factors cancel the excess heating by photons and guarantee the conservation of total energy in large homogeneous system. Those PW KERMA factors are collapsed in the module GROUPR. It is noted that the module GROUPR produces the neutron KERMA factors at infinite dilute condition. If these neutron KERMA factors were directly used in the heating calculation, the heat generation rate would be over-estimated because of unshielded XSs. For the example of ABTR fuel pin cell problem, 2,082 group KERMA factors were calculated with the infinite dilute and self-shielded XSs. Figure 5.2 compares these KERMA factors for ^{235}U and ^{56}Fe. The relative error indicates that the absolute value of relative error between two XSs. As shown in the figure, the relative errors of two KERMA factors become larger than 100% in the resonance energy range. The neglect of self-shielding effect on KERMA factor results in over-estimated heating rates in the resonance region.

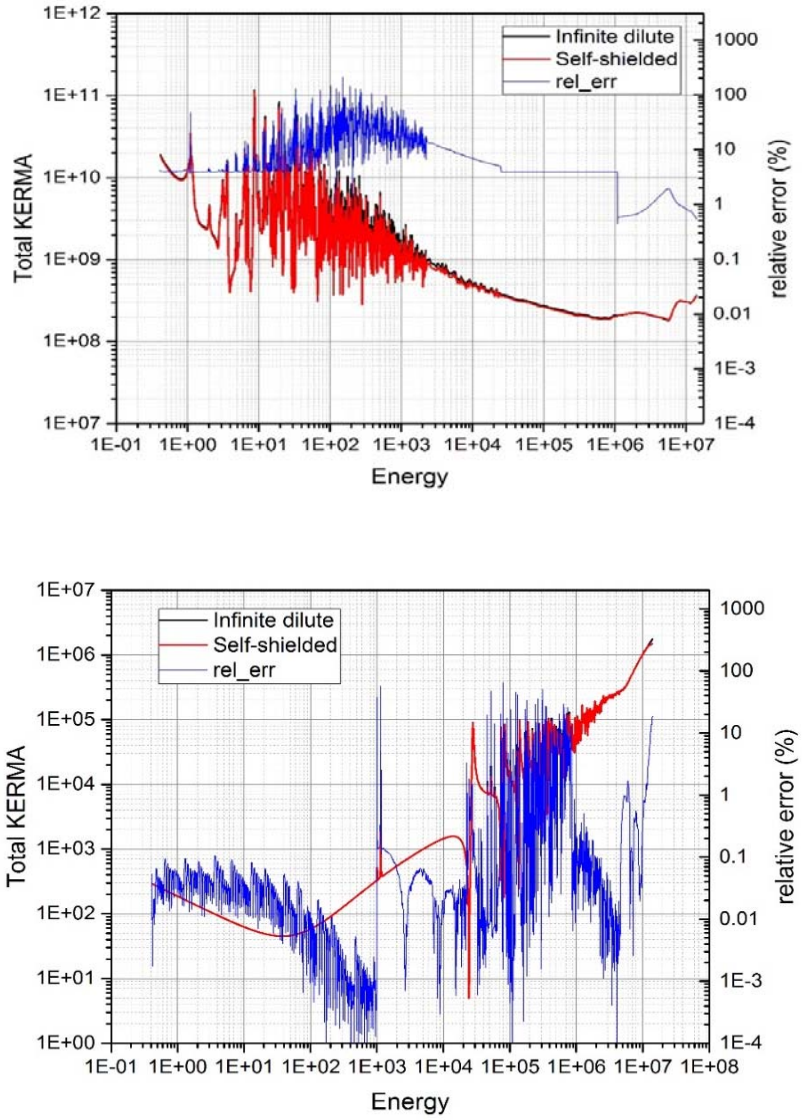

Figure 5.2 Self-shielded and infinite dilute total neutron KERMA factor of ^{235}U (above) and ^{56}Fe (below)

In order to account for the self-shielding in the neutron KERMA factor, the partial kinetic energy release per reaction is determined by dividing the partial KERMA factor by the neutron XS and it is stored in the MC^2-3 library. In a MC^2-3 calculation, the neutron KERMA factors for a given composition are computed by multiplying the energy releases per reaction and self-shielded

XSs. Since the partial neutron KERMA factors are required to facilitate the self-shielding of neutron KERMA factors, the PreMCS code prepares an additional input of the HEATR module of NJOY. In GenMCS, the obtained partial neutron KERMA factors are converted into the partial kinetic energy release per reaction. For the non-elastic reactions, the neutron KERMA factors computed by NJOY are directly given in the gamma library. The GAMINR module of NJOY provides XSs for four different reactions from the ENDF photo-atomic sub-library. Coherent, incoherent, pair production, and photoelectric XSs and gamma KERMA factors are determined using the user-specified group structure and weighting spectrum. The module GAMINR provides a constant spectrum, 1/E spectrum and user-specified spectrum options to collapse the gamma interaction XSs. The PreMCS code prepares an input file of NJOY with a 1/E weighting spectrum with roll-offs since the 1/E weighting spectrum may represent the characteristics of gamma flux distribution in the core except for the low energy region below 0.1 MeV where the photoelectric absorption is dominant. In order to verify the adequacy of the 1/E weighting spectrum, 21-group gamma interaction XSs of uranium were computed for the ABTR fuel pin mixture using NJOY with 1/E and constant spectra and were compared with the MCNP6 reference results. Since MCNP6.2 only deals with prompt heating, it was verified by comparing the gamma cross sections of NJOY with that of MCNP without the addition of delayed components in gamma reaction rate estimation. As shown in Figure 5.3, the XSs computed with the 1/E spectrum agree well with the MCNP6 results except for the intermediate energy range where the relative errors show sharp peaks due to the gamma source from uranium and iron. Thus, it is judged that the 1/E spectrum is adequate to generate the base 94-group gamma library. Since the mass of photon is negligible, the scattering of gamma ray is highly anisotropic. The Legendre scattering matrices were generated up to P_3 for the new 94-group gamma interaction XS library.

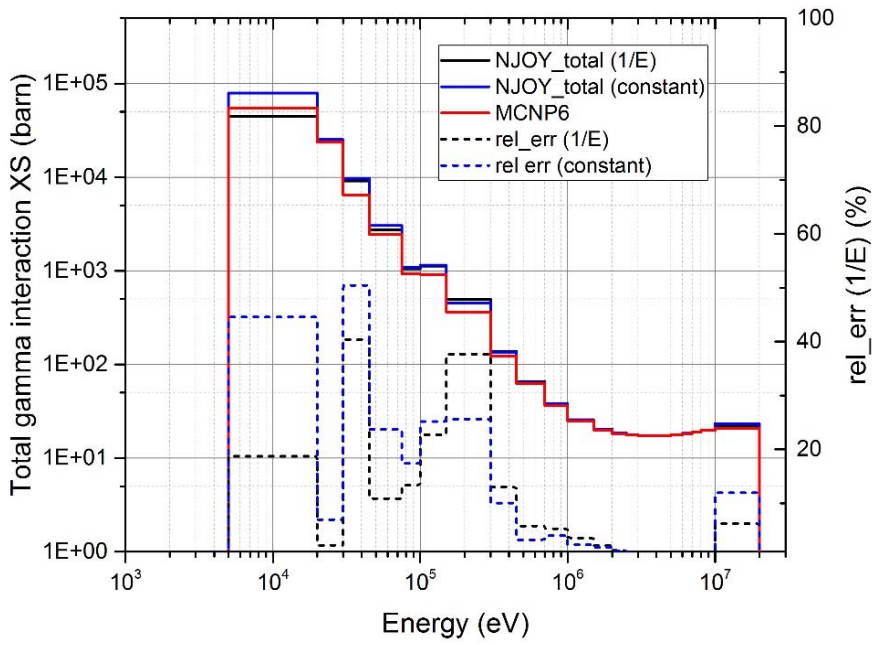

Figure 5.3 Total gamma interaction cross sections of uranium in ABTR fuel pin mixture

5.1.3 Generation of delayed photon yield

In the HEATR module of NJOY [25], the effective Q-value is determined by subtracting the portion of delayed photons and neutrinos from the mass difference Q-value. In order to obtain the exact KERMA factors and photon production matrix, the contribution of delayed photons should be considered after the process of NJOY. Main sources of delayed photons are the decays of fission products and their daughter isotopes. The contribution of delayed photons and betas resulting from the decay of fission products can be easily obtained from the ENDF data File 1, MT 458 that is based on the Sher's evaluation [78]. Under the assumption that beta particle energies are deposited locally at the site of which fission occurred, the contribution of delayed betas to heat generation rates can be considered by adding the delayed beta KERMA factor to the total KERMA

factor. The delayed beta KERMA factor can be determined by multiplying the total energy released by delayed betas with the self-shielded fission XS.

For coupled neutron-gamma transport calculations, however, delayed gammas should be added to gamma production matrices. In the MC^2-2 code [4], the delayed gamma data were given in the DLYFIS file based on the ENDF/IV and those data were stored in the MCCF9 file, which is one of the MC^2-2 base libraries. The delayed gamma data in MCCF9 were no longer available in the MC^2-3 code, since the MC^2-3 library for those data has been replaced with the chi matrix and infinite-dilute UFG XSs. In the ENDF/B VII.1 library, the delayed gamma source functions can be determined using the time constants in MT 460 of File 1 and the photon multiplicities in MT 460 of File 12. The delayed gamma source function is defined as the number of gammas emitted per unit time after the fission event, per unit energy for a fixed incident energy. Unfortunately, the yield data for delayed gamma are only given for ^{235}U and ^{239}Pu in the latest ENDF/B VII.1 library. Even though it reproduces the gamma ray spectra resulting from neutron-induced fission using 1,000 decay nuclides and 20,000 discrete-emission energies from England and Rider [79] and the NNDC NuDat nuclear database, the results are limited by the lack of experimental data and the uncertainties of fission product yields [80]. For these reasons, the PreMCS code calculates the delayed photon yield data using the latest decay and fission yield sub-libraries. The delayed photon production option activates the calculation of delayed beta and delayed gamma yield from the ENDF-6 format library.

As mentioned above, the kinetic energies of delayed betas and gammas are retrieved from the ENDF/B File 1, MT 458. The energy components resulting from fission event in MT 458 can be expressed as [27]:

$$\begin{aligned} E_i(E_{inc}) &= E_i(0) - \delta E_i(E_{inc}) \qquad \text{if NPLY=0 , } \delta E_i(E_{inc}) = 0.075 E_{inc} \\ E_i(E_{inc}) &= c_0 + \mathrm{c}_1 \mathrm{E}_{inc} + \mathrm{c}_2 \mathrm{E}_{inc}^2 \cdots \qquad \text{if NPLY} \neq 0 \end{aligned} \tag{5.3}$$

where NPLY denotes the order of polynomial expansion of the energy component, i is the index of energy component, E_{inc} is the incident neutron energy, $E_i(0)$ is a constant for delayed beta and gamma components of fission energy release, and $\delta E_i(E_{inc})$ is the function that defines the energy dependence of delayed beta and gamma energy components. The code reads these data form the delayed photon library. In the MC^2-3 code, the contribution of delayed betas is determined by multiplying the energy component of delayed betas with the self-shielded fission XS.

To calculate the delayed gamma production matrix, PreMCS constructs the decay chains of fission products by reading the fission yield and radioactive decay sub-libraries. The gamma production matrix is then constructed by aggregating all the decay gamma spectra. The ENDF-6 format sub-libraries of decay and fission yield provide the important information for decay heat analysis and fission products. The accuracy of delayed gamma yield calculation highly depends on the data in these libraries. The ENDF.B VII.1 and JENDL decay libraries are primarily based on the ENSDF (Evaluated Nuclear Structure Data File) [81], which includes evaluated nuclear structure and decay information obtained by international cooperation. Although the ENDF/B VII.1 sub-libraries provide the decay data for all fission products, the accuracy of decay data cannot be guaranteed due to the incompleteness of experimental data for short-lived nuclides and complex decay scheme. Moreover, when the Q-value of a fission product increases, the gamma rays with weak energy are not observed in the gamma ray measurement. In order to overcome these inaccuracies in the decay heat analysis, the JENDL decay data was compiled in 2011 to maintain consistency between the average beta and gamma decay energies with their spectra data [82,83]. Therefore, the JENDL decay and fission yield data files were used to generate the delayed gamma yield matrices in this work. In the PreMCS code, the summation of delayed gammas for each activation product is normalized to the average decay value using the theoretical spectrum.

Table 5.1 compares the delayed gamma energy per fission estimated by PreMCS using the fission yield and decay data of various libraries with the delayed gamma energy per fission in the File 1, MT 458 data of ENDF/B-VII.1. MCNP6-CINDER indicates the calculated delayed gamma energy using the decay data file (CINDERGL.DAT) of MCNP6 and ENDF/B VII.1 fission yield library. It can be seen that the delayed gamma energies estimated with the JENDL libraries agree with the MT 458 data better than the other libraries. In the PreMCS calculation, the delayed gamma production matrices are renormalized so that the total delayed gamma energy is equal to the reference value of MT 458 data.

Table 5.1 Comparison of delayed gamma energy per fission (MeV) estimated from fission product decays with MT 458 data for major actinides.

Fission Yield and Decay Libraries	^{235}U	^{238}U	^{239}Pu	^{240}Pu	^{241}Pu	^{242}Pu	^{241}Am
Reference (MT 458 of File 1)	6.33	8.25	5.17	6.49	6.40	6.82	5.51
ENDF/B VII.1	5.62	6.87	4.56	5.00	5.43	5.81	4.32
JENDL	6.22	7.72	5.25	5.77	6.27	6.65	5.02
Delayed Gamma Source Function (MT 460 of File 1)	2.90	-	2.99	-	-	-	-
MCNP6-CINDER	5.07	5.47	4.10	4.34	4.51	4.63	3.87

* Incident neutron energy = 0.0253 (eV)

5.2 Coupled Neutron and Gamma Heating Calculation

To perform the gamma transport calculation for group collapsing, the 0D and 1D gamma transport solvers were implemented into the MC^2-3 code. The transport solver was developed by extending the existing driver routines for 0D and 1D transport calculations. In the gamma transport calculation of MC^2-3, the photoelectric absorption was treated as an absorption reaction in the gamma group constant. Note that the fluorescent effect, which is the emission of the portion of

absorbed photon and electron from the photoelectric absorption, is not considered in the MC^2-3 code yet. Incoherent (Compton) and coherent (Thompson) scatterings are treated as a simple scattering reaction, while the pair production reaction is treated as (n,2n) reaction in the gamma transport calculation. If the gamma XSs for individual regions are prepared, the transport calculation is performed with a fixed gamma source distribution. The fixed gamma source is calculated by multiplying the neutron flux with the gamma production matrices obtained from the neutron transport calculation. The following fixed-source gamma transport equation is solved using the 0D and 1D transport solver:

$$\Omega \cdot \nabla \phi_{\gamma}^{g} + \Sigma_{t}^{g} \phi_{\gamma}^{g} = \sum_{g'} \Sigma_{\gamma\gamma}^{g' \to g} \phi_{\gamma}^{g'} + \sum_{n} \Sigma_{\gamma n}^{n \to g} \phi_{n}^{n} + S_{\gamma}^{g} \tag{5.4}$$

where the subscripts n and γ denote the neutron and gamma quantities, respectively, and the superscripts n and g represent the neutron and gamma groups, respectively. That is, ϕ_n^n is the n-th group neutron flux determined from the neutron transport calculation and ϕ_γ^g is the g-th group gamma flux. Σ_t^g is the macroscopic total XS of gamma group g, $\Sigma_{\gamma\gamma}^{g' \to g}$ is the macroscopic scattering XS from gamma group g' to g, $\Sigma_{\gamma n}^{n \to g}$ is the macroscopic production XS from neutron group n to gamma group g, and S_γ^g represents the external gamma source.

To consider the global leakage effect of gamma, MC^2-3 incorporates TWODANT for the 2D neutron and gamma transport calculation. MC^2-3 code prepares 94-group macroscopic gamma XS as well as the region-dependent gamma source for TWODANT fixed source calculation. 2D neutron transport calculation should precede gamma transport calculation to obtain the gamma source distribution from neutron interactions. After the TWODANT execution for neutron transport calculation, MC^2-3 reads TWODANT solution to generate gamma source distribution by multiplying with gamma production matrices:

$$S_{\gamma}^{g} = \sum_{n} \Sigma_{\gamma n}^{n \to g} \phi_{n}^{n} \tag{5.5}$$

where the subscript n and γ denotes the neutron and gamma quantities, respectively, and the superscript n and g represent the neutron and gamma groups, respectively. That is, ϕ_n^n is the n-th group neutron flux determined from the TWODANT neutron transport calculation and $\Sigma_{\gamma n}^{n \to g}$ is the macroscopic production XS from neutron group n to gamma group g, and S_{γ}^{g} represents the fixed gamma source to be used in TWODANT gamma transport calculation. Figure 5.4 compares the 94-group gamma spectra for a 45-pin driver fuel assembly and a control assembly. For the fuel assembly, the flux spectrum determined by the TWODANT calculation agrees very well with that obtained from the homogeneous medium calculation since the gamma rays in the fuel are mainly produced in the assembly. On the other hand, the two gamma flux spectra of the control assembly are notably different from each other since the control assembly spectrum in the core is mainly determined by the gamma rays transported from the neighboring fuel assemblies. It can be seen that the spectrum determined from the homogeneous medium calculation is significantly softer than that obtained from TWODANT calculation. MC^2-3 writes the TWODANT input file for gamma transport calculation as well as the gamma source distribution and run TWODANT.

The second job of MC^2-3 performs group condensation using both TWODANT solutions. The calculated gamma group flux is used in generating the BG gamma interaction XSs and heating factors. Figure 5.5 shows the comparison of 21 group total gamma XSs of uranium and boron condensed by homogeneous and TWODANT spectrum. It can be seen that the total gamma XSs of uranium determined with a homogeneous medium calculation of MC^2-3 and TWODANT spectrum agree well with a maximum error less than 0.25% in group 15 (150 keV – 300 keV), except for the group 21 (5 keV – 20 keV). Note the large difference in group 21 result from the

abrupt changes in photoelectric absorption XSs. Even though the flux is almost zero below 100 keV, the small difference in spectrum induces a large difference in the XS of last group. As can be seen in the figure, the differences between two XSs for boron are larger than the uranium case, due to the differences in gamma spectrum. Though there are significant difference in flux spectrum in non-fuel region, the difference of boron total XS is less than 1.2% since gamma XSs are smooth in most energy range except for low energy range where photoelectric absorption reaction is dominant. The calculated gamma group flux is used in generating the broad-group gamma interaction XSs and heating factors. For each broad group, the heating factor and interaction XSs are determined by collapsing the 94-group XSs in the library as

$$\sigma_x^G = \frac{\sum_{g\in G} \sigma_x^g \phi_\gamma^g}{\sum_{g\in G} \phi_\gamma^g} \tag{5.6}$$

$$\sigma_x^{G'\to G} = \frac{\sum_{g\in G} \sum_{g'\in G'} \sigma_x^{g'\to g} \phi_\gamma^{g'}}{\sum_{g'\in G'} \phi_\gamma^{g'}} \tag{5.7}$$

$$K_x^G = \frac{\sum_{g\in G} K_x^g \phi_\gamma^g}{\sum_{g\in G} \phi_\gamma^g} \tag{5.8}$$

where σ and K represent the interaction XS and gamma KERMA factor, respectively. The subscript x denotes the reaction type, and the superscript g and G denoting the fine and broad gamma group indices, respectively.

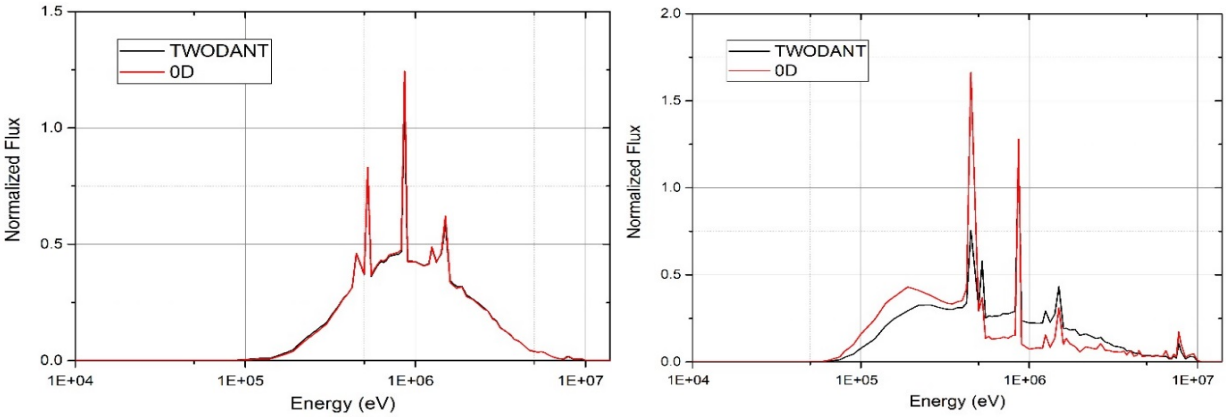

Figure 5.4 Comparison of gamma spectra determined from 0D mixture and TWODANT calculations for fuel (left) and control assembly (right)

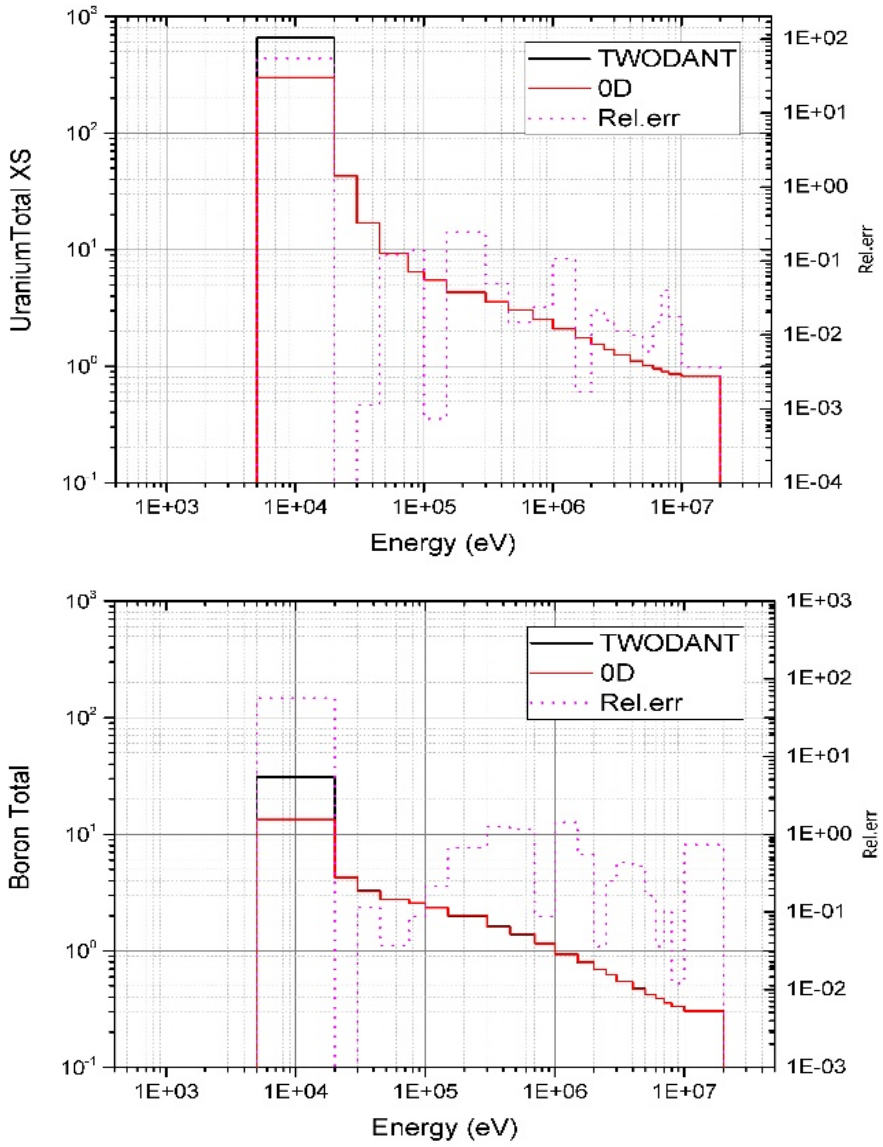

Figure 5.5 Comparison of 21 group total gamma cross sections for uranium in driver fuel assembly (top) and boron in control assembly (bottom)

5.3 Numerical Tests with New Gamma Library

5.3.1 ABTR fuel pin cell problem

As the first step to test the newly implemented gamma transport capabilities and libraries of MC^2-3, the gamma flux distribution and the gamma interaction XSs were calculated for a cylindrical fuel pin problem of ABTR in section 2.3 and were compared with the reference MCNP6 solution. Both calculations were performed with the XS libraries based on the ENDF/B VII.0 data. The MCNP6 calculation was performed with 1,000 active cycles and 10,000 histories per cycle. The delayed fission gammas were not considered since the MCNP6 XS library lacks the corresponding data. For the consistent comparison between MC^2-3 and MCNP6, simple photon physics treatments were selected, which does not simulate fluorescent photons, bremsstrahlung and photon Doppler broadening. The relative statistical errors of MCNP6 results were less than 0.3% except for the high energy region above 10 MeV. The reflective boundary condition is imposed on the fuel pin boundary. Figure 5.6 shows the 94 group gamma flux distributions in the fuel region obtained from MC^2-3 calculations with and without delayed gammas and that from MCNP6 calculation without delayed gammas. It is clearly seen that the gamma flux distribution of MC^2-3 without delayed gammas agrees very well with the MCNP6 solution. Note that the sharp peak at 0.5 MeV is mainly due to the gamma rays from the neutron capture and fission reactions of ^{235}U and the pair production reactions in the high-energy range. The peak at 0.8 MeV is mainly due to the inelastic scattering reactions of ^{56}Fe.

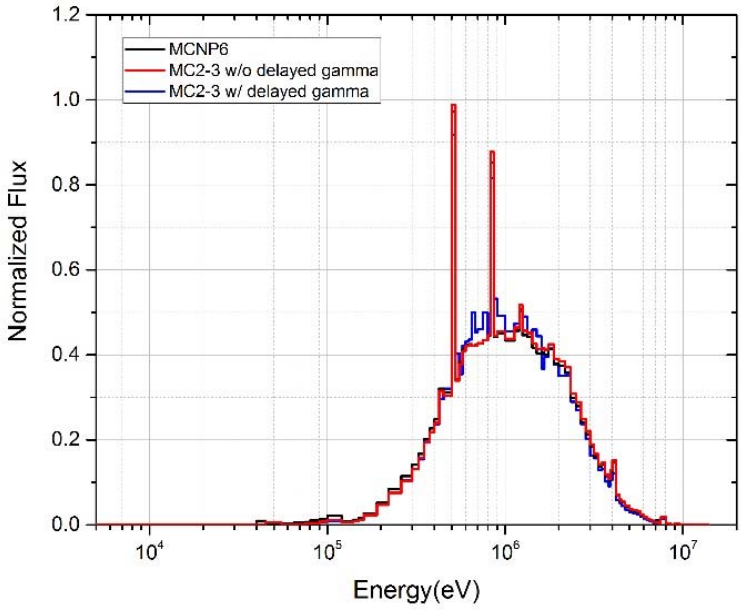

Figure 5.6 94-group gamma flux distributions in ABTR fuel

Figure 5.7 compares the 94 and 21 group total gamma interaction XSs calculated with MC^2-3 and MCNP6 for uranium and iron, respectively. It can be seen that the 21-group gamma interaction XSs determined with MC^2-3 agree well with those determined with MCNP6 except for the groups 17 to 19 (30 keV - 100 keV) and group 21 (5 keV – 20 keV). These differences in low-energy XSs result from the differences in the 94-group gamma libraries themselves, which are caused by the abrupt changes in photoelectric absorption XSs due to the absorption edges of different electron shells. These results indicate that the 94-group structure of CSEWG is not sufficiently fine to represent the photoelectric absorption edges accurately. However, as can be seen in Figure 5.6, the flux level is very low in the energy range below 100 keV, where the photoelectric absorption XSs are important. Therefore, it is judged that the 94-group structure is adequate for the coupled neutron and gamma heating calculations.

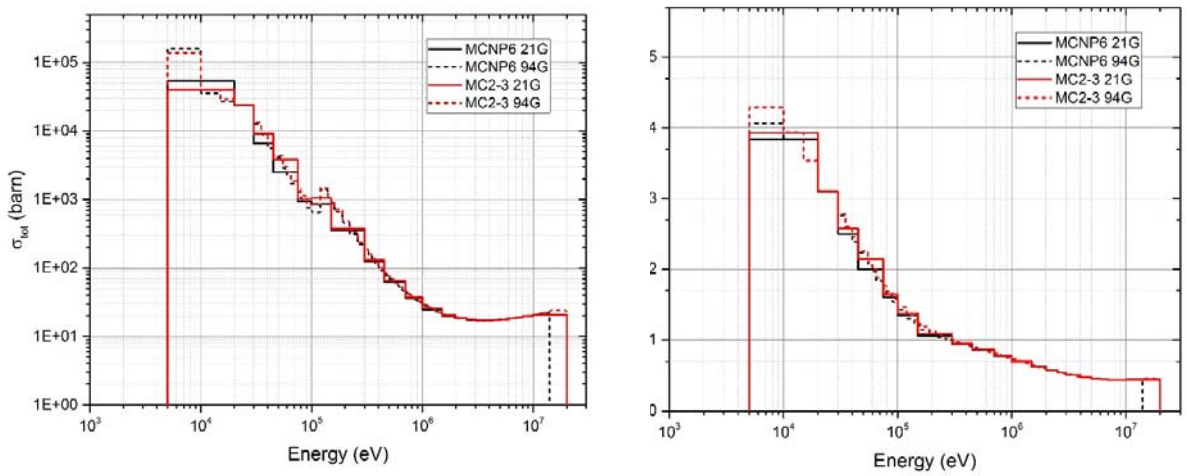

Figure 5.7 Total gamma XS of uranium (above) and iron (below) in ABTR fuel pin

5.3.2 EBR-II Run 138B problem

In order to examine the new gamma data generation procedure in total heat estimation, coupled neutron and gamma heating calculations were performed for the EBR-II benchmark problem [26] using the VARIANT with the XSs prepared with the new gamma data generation scheme of MC^2-3. The EBR-II benchmark problem is based on the core configuration of Run 138B, which consists of 71 regular driver fuel assemblies, 13 half-worth fuel driver assemblies, 10 control and safety assemblies, six structural assemblies, and six instrumented assemblies. The detailed core specifications can be found in [84]. For comparison, the MCNP6 calculation was performed with 180 active cycles with 100,000 histories per cycle. The delayed fission gammas were not considered in both MC^2-3/VARIANT and MCNP6 calculations for a consistent comparison. Figure 5.8 shows the relative differences in assembly power of the MC^2-3/VARIANT solution from the MCNP6 solution. The results of MCNP6 have relative statistical errors less than 0.2%. The assembly powers of the VARIANT results obtained with the current 21-group gamma

library of MC^2-3 agreed with the MCNP solutions within 4%. It is noted that the MC^2-3/VARIANT solution underestimates the power densities in structural assemblies but overestimates those in the control and safety assemblies. With the new library, the differences in assembly power from the MCNP6 solution are reduced to less than 2.6% by employing the new gamma library, gamma transport solution and TWODANT core calculation. It is noted that further verification and validation of the new 94G gamma library has been performed as well as the extension of gamma transport solver to 2D MOC, which can be found in [85].

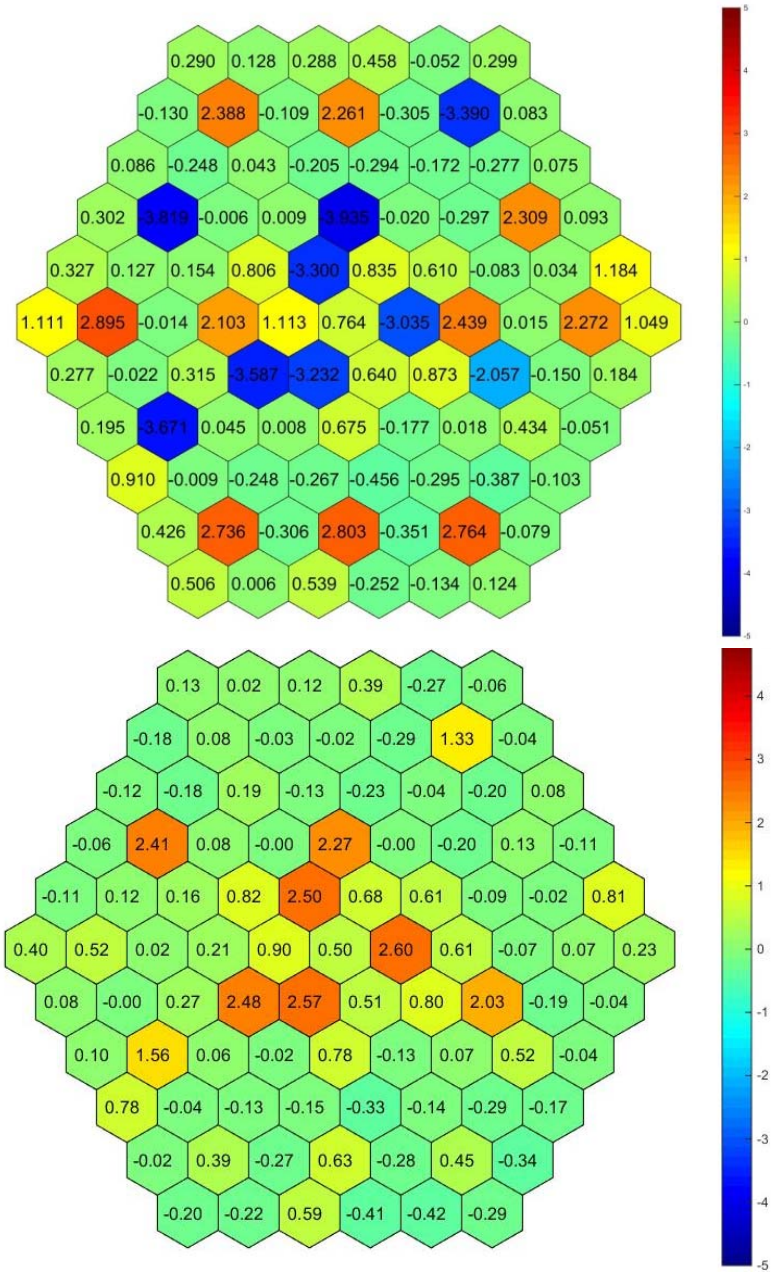

Figure 5.8 Relative difference (%) in assembly power density between MCNP6 and MC2-3/VARIANT with the old (above) and new (below) gamma libraries

Chapter 6 Conclusion

A new multigroup cross section library generation procedure was established for high-fidelity simulation of advanced reactors by developing a generalized cross section generation method applicable to different reactor types from thermal to fast energy spectrum systems. To eliminate the approximations of the current procedures tailored to each targeted reactor type, the detailed slowing down approach of MC^2-3 was selected as a starting point. The MC^2-3 capabilities limited to fast spectrum applications were extended to thermal systems. 2,082 ultrafine group structure was extended to 3,483 energy groups ranging from 10^{-5} eV to 20 MeV. 2D MOC transport solver as well as the homogeneous and 1D CPM solvers of MC^2-3 has been extended to comply with the thermal XS library and upscattering iteration. The extended UFG calculation capabilities were tested using ten heterogeneous pin cell benchmarks including PWR, BWR, ABTR, HTGR and MSR problems. The modified MC^2-3 successfully reproduced the benchmark results compared to the reference MCNP solutions with a maximum difference of -132 pcm in reactivity and less than 30 pcm errors in group-wise reactivity.

To accurately represent the local heterogeneity effects of thermal systems, the detailed slowing-down calculations need to be performed for larger problem domains such as fuel assemblies or fractions of the core. However, a UFG lattice calculation for a larger problem domain requires substantial computational time. To reduce the computational burden of ultrafine group lattice calculation without losing accuracy, the generalized condensation scheme was introduced. This is a key contribution of this research, as it quantifies higher-order scattering, local heterogeneity, global transition effects in terms of reactivity change due to reaction rate differences

during the cross-section generation process. The ultrafine group weighting spectrum is approximately, but accurately obtained by solving three sequential transport solutions. Eight assembly cases, including PWR, BWR and moderated target in LEUFBR, were solved using the generalized condensation scheme. The intermediate group lattice calculation with the generalized condensation scheme yields similar results for both eigenvalue and pin power compared to the ultrafine group calculation, although the neglect of angle dependency in total cross section slightly underestimates the eigenvalues of intermediate group calculations results with the reduced number of groups. Intermediate group solutions were used to generate broad group self-shielded cross sections and scattering matrices

A new cross section library generation procedure was developed for the high-fidelity neutronic code, MPACT. To minimize efforts and time required for the cross section library generation, the new library was generated by replacing the existing multigroup library data with the MC^2-3 results. An ultrafine group MC^2-3 lattice calculation with the generalized condensation scheme is repeated to retrieve various background cross sections, and corresponding self-shielded cross sections and scattering matrices to form a problem-dependent resonance data table. The library format and subsequent code structure have been changed accordingly. To verify the new library, PWR and two BWR assembly problems were solved with two libraries generated using the current and the new library generation procedure. The new library provided a good agreement with the current library for the PWR problem, and it showed great improvements in eigenvalue and pin power for the highly voided BWR problems, compared to the reference MCNP solutions.

The next step was to improve the resonance self-shielding calculation in high-fidelity simulation. Azimuthally dependent self-shielded cross section generation scheme and the resonance self-shielding treatment for particulate fuel were implemented in the fixed source

calculation in MPACT and SCALE-Polaris, respectively. The azimuthal discretization scheme does not show a noticeable difference in steady state, while it gives a meaningful impact in the burnup calculation of a typical gadolinium-bearing assembly of a BWR. The azimuthal discretization scheme burns gadolinium isotopes faster than the current cross section generation scheme in the initial burnup time steps and slower in the later burnup time steps. The new method for particulate fuel modeling was developed and implemented in the framework of cell Dancoff based ESSM with the Hebert collision probability method. A new cross section library was generated using MC^2-3 for the graphite-moderated system by changing the packing fraction of fuel grains instead of moderator density. MC^2-3 allows users to choose the parameter for the variation of background cross sections. The new resonance treatment capability for double heterogeneous fuel was verified for the prismatic-type HTGR unit-cell problem and HTR pebble bed reactor problem. The new method demonstrated good accuracy with the reference Serpent-2 solutions.

For the accurate assessment of the heat generation rate in advanced reactors, a new computational scheme for gamma data generation was implemented in MC^2-3. Gamma yield and interaction cross section libraries were developed in the 94-group structure. Self-shielding effects of production and KERMA factors are properly considered, and delayed gamma data was also calculated. Gamma transport calculation was implemented in MC^2-3 in order to calculate the 94-group gamma flux distribution used as the weighting spectrum for the generation of broad group gamma cross sections. The spectral transition effect was considered using the TWODANT transport solver. The new capabilities of MC^2-3 for gamma cross section generation were tested using an ABTR pin cell problem and the EBR-II benchmark problem. Detailed comparison of gamma spectra and gamma interaction cross sections for the ABTR pin cell problem with the one tallied from MCNP showed that MC^2-3 results agree very well with the corresponding MCNP6

results. From the coupled neutron and gamma heating calculation with VARIANT for the EBR-II benchmark problem, the assembly powers obtained with the new gamma cross sections agree well with the MCNP6 results within 2.6% for the structural assembly.

Bibliography

1. C. S. Lin and W. S. Yang, "An assessment of the applicability of multigroup cross sections generated with Monte Carlo method for fast reactor analysis," *Nucl. Eng. Technol.* **52** (12), pp. 2733, Korean Nuclear Society (2020); https://doi.org/10.1016/j.net.2020.05.029.
2. Alvin M. Weinberg and Eugene P. Wigner, *The Physical Theory of Neutron Chain Reactors*, University of Chicago Press, Chicago (1958).
3. P.H. Kier and A. A. Robba, "RABBLE, A program for Computation of Resonance Absorption in Multiregion Reactor Cells," ANL-7326, Argonne National Laboratory (1967); https://doi.org/10.2172/4245065.
4. H. Henryson, B. J. Toppel, and C. G. Stenberg, "MC2-2: A Code to Calculate Fast Neutron Spectra and Multigroup Cross Sections," Argonne National Laboratory, ANL-8144 (1976); https://doi.org/doi.org/10.2172/7143331.
5. Changho Lee, Yeon Sang Jung, and Won Sik Yang, "MC2-3: Multigroup Cross Section Generation Code for Fast Reactor Analysis," ANL/NE-11/41 Rev.4, Argonne National Laboratory (2018); https://doi.org/doi.org/10.2172/1483949.
6. B. T. Rearden and M. A. Jessee, "SCALE Code System, Version 6.2," ORNL/TM-2005/39, Oak Ridge National Laboratory (2016).
7. K. S. Kim et al., "The SCALE/AMPX multigroup cross section processing for fast reactor analysis," *Ann. Nucl. Energy* **132**, pp. 161 (2019); https://doi.org/10.1016/j.anucene.2019.04.034.

8. I. I. Bondarenko, *Group Constants for Nuclear Reactor calculation*, Consultants Bureau Enterprises, Inc., New York (1964).

9. R. J. J. Stamm'ler and M. J. Abbate, *Methods of Steady-State Reactor Physics in Nuclear Design*, Academic Press, London (1983).

10. Changho Lee and Yeon Sang Jung, "Generation of the Cross Section Library for PROTEUS," ANL/NE-18/2, Argonne National Laboratory (2018).

11. R. J. J. Stamm'ler, "HELIOS Methods," Studsvik Scandpower (2003).

12. L. B. Levitt, "The Probability Table Method for Treating Unresolved Neutron Resonances in Monte Carlo Calculations," *Nucl. Sci. Eng.* **49** (4), pp. 450 (1972); https://doi.org/10.13182/NSE72-3.

13. C. H. Lee and W. S. Yang, "Status Report on Multigroup Cross Section Generation Code Development for High-Fidelity Deterministic Neutronics Simulation System," ANL-AFCI-207, Argonne National Laboratory (2007).

14. Kang Seog Kim, "SUBGR: A Program to Generate Subgroup Data for the Subgroup Resonance Self-Shielding Calculation," CASL-X-2016-1070-000, Oak Ridge National Laboratory (2016).

15. S. G. Hong and K. S. Kim, "Iterative resonance self-shielding methods using resonance integral table in heterogeneous transport lattice calculations," *Ann. nucl. Energy* **38** (1), pp. 32 (2011); https://doi.org/10.1016/j.anucene.2010.08.022.

16. M. L. Williams et al., "Multigroup Data Processing for the Embedded Self-Shielding Method in SCALE," *PHYSOR 2016*, Sun Valley, Idaho, May 1-5 (2016).

17. K. S. Kim and M. L. Williams, "Spatially dependent embedded self-shielding method for nonuniform temperature distribution," *Ann. Nucl. Energy* **132**, pp. 563 (2019); https://doi.org/10.1016/j.anucene.2019.06.043.

18. Y. Liu et al., "A full-core resonance self-shielding method using a continuous-energy quasi-one-dimensional slowing-down solution that accounts for temperature-dependent fuel subregions and resonance interference," *Nucl. Sci. Eng.* **180** (3), pp. 247 (2015); https://doi.org/10.13182/NSE14-65.

19. K. Yamaji et al., "Ultra-fine-group resonance treatment using equivalent Dancoff-factor cell model in lattice physics code GALAXY," *J. Nucl. Sci. Techol.* **55** (7), pp. 756 (2018); https://doi.org/10.1080/00223131.2018.1439416.

20. G. Rimpault, "Algorithmic features of the ECCO cell code for treating heterogeneous fast reactor subassemblies," *International conference on mathematics and computations, reactor physics, and environmental analyses*, Portland, Oregon (1995).

21. A. Hebert, "Collision probability analysis of the double-heterogeneity problem," *Nucl. Sci. Eng.* **115** (2), pp. 177 (1993); https://doi.org/10.13182/NSE115-177.

22. R. Sanchez and G. C. Pomraning, "A statistical analysis of the double heterogeneity problem," *Ann. Nucl. Energy* **18** (7), pp. 371 (1991).

23. R. N. Hill, "Argonne National Laboratory, Coupled Neutron-Gamma Heating Calculations," Personal communication (1988).

24. K. L. DERSTINE, "DIF3D: A Code to Solve One-, Two-, and Three-Dimensional Finite-Difference Diffusion Theory Problems," ANL-82-64, Argonne National Laboratory (1984).

25. R. E. Macfarlane, "The NJOY Nuclear Data Processing System, Version 2012," LA-UR-12-2, Los Alamos National Laboratory (2012).

26. T. Fei et al., “Calculation of Photon Heat Generation for EBR-II Using DIF3D/MC2 -3,” *Transactions of the American Nuclear Society* ***111***, pp. 1271–1273, Anaheim, California (2014); https://doi.org/doi.org/10.2172/1483949.

27. A. TRKOV, M. HERMAN, and D. BROWN, “"ENDF-6 Formats Manual: Data Formats and Procedures for the Evaluated Nuclear Data Files ENDF/B-VI and ENDF/B-VII,” BNL-90365-2009 Rev.2, Brookhaven National Laboratory (2012).

28. J. R. Askew and M. J. Roth, “WIMS-E,” AEEW-R--1315, UKAEA Atomic Energy Establishment (1982).

29. J. Rhodes, K. Smith, and D. Lee, “CASMO-5 Development and Applications,” *PHYSOR-2006, ANS Topical Meeting on Reactor Physics*, Vancouver, BC, Canada (2006).

30. G. Marleau, A. Hebert, and R. Roy, “A User Guide for DRAGON,” IGE-174 Rev. 4, Ecole Polytechnique de Montréal (1998).

31. Hebert Alain, *Applied Reactor Physics*, Montréal : Presses internationales Polytechnique (2009).

32. M. Gamarino et al., “Rehomogenization of nodal cross sections via modal synthesis of neutron spectrum changes,” *Nucl. Sci. Eng.* **190** (1), pp. 1, American Nuclear Society (2018); https://doi.org/10.1080/00295639.2017.1417214.

33. Ray E. Alcouffe et al., “User’s Guide for TWODANT: A Code Package for Two-Dimensional, Diffusion-Accelerated, Neutral-Particle Transport,” LA--10049-M-Rev.l, Los Alamos National Laboratory (1984).

34. Won Sik Yang, “Lecture 4: Implications on Core Design and Computational Methods,” NERS 590: Fast Reactor Physics and Computational Methods, University of Michigan (2017).

35. H. G. Joo et al., “Dynamic implementation of the equivalence theory in the heterogeneous whole core transport calculation,” *PHYSOR 2002*, Seoul, Korea (2002).

36. A. Galia, R. Sanchez, and I. Zmijarevic, “A method of dynamic homogenization: application to 2D core calculation,” *Ann. Nucl. Energy* **151**, Elsevier Ltd (2021); https://doi.org/10.1016/j.anucene.2020.107774.

37. R. Sanchez, “Assembly homogenization techniques for core calculations,” *Progress in Nuclear Energy* **51** (1), pp. 14, Elsevier Ltd (2009); https://doi.org/10.1016/j.pnucene.2008.01.009.

38. K. S. Smith, “Assembly homogenization techniques for light water reactor analysis,” *Progress in Nuclear Energy* **17** (3), pp. 303 (1986).

39. A. Kavenoky, “The SPH homogenization method,” IAEA-TECDOC--231, International Atomic Energy Agency (IAEA) (1980).

40. A. Hebert and G. Mathonniere, “Development of a third-generation superhomogeneization method for the homogenization of a pressurized water reactor assembly,” *Nucl. Sci. Eng.* **115** (2), pp. 129 (1993); https://doi.org/10.13182/NSE115-129.

41. M. A. Pope, J. Ortensi, and A. M. Ougouag, “Investigation of Supercells for Preparation of Homogenized Cross Sections for Prismatic Deep Burn VHTR Calculations,” *Proceedings of HTR 2010*, Prague, Czech Republic, October 18-20 (2010).

42. J. Ortensi et al., “A Newton solution for the Superhomogenization method: The PJFNK-SPH,” *Ann. Nucl. Energy* **111**, pp. 579 (2018); https://doi.org/10.1016/j.anucene.2017.09.027.

43. S. Jang and Y. Kim, “A study of leakage-corrected two-step method based on the nodal equivalence theory for fast reactor analysis,” *PHYSOR 2020 : International Conference on*

Physics of Reactors: Transition to a Scalable Nuclear Future ***247***, pp. 318–325, EDP Sciences - Web of Conferences (2020); https://doi.org/10.1051/epjconf/202124702026.

44. A. Yamamoto et al., "Improvement of the SPH Method for Multi-assembly Calculations," *PHYSOR 2004 -The Physics of Fuel Cycles and Advanced Nuclear Systems: Global Developments*, American Nuclear Society (2004).

45. P. Mondot, R. Sanchez Commissariat À L', and E. Atomique, "An iterative homogenization technique that preserves assembly core exchanges," *International conference on supercomputing in nuclear applications, SNA2003*, France (2003).

46. A. Dall'osso, "A spatial rehomogenization method in nodal calculations," *Ann. Nucl. Energy* **33** (10), pp. 869 (2006).

47. M. Gamarino et al., "Investigation of rehomogenization in the framework of nodal cross-section corrections," *PHYSOR 2016*, Sun Valley, ID, USA.

48. D. Shepard, "A two-dimensional interpolation function for irregularly-spaced data," *Proceedings of the 1968 ACM National Conference*, pp. 517–524 (1968).

49. G. Palmiotti, E. E. Lewis, and C. B. Carrico, "VARIANT: VARIational Anisotropic Nodal Transport for Multidimensional Cartesian and Hexagonal Geometry Calculation," ANL-95/40, Argonne National Laboratory, Argonne National Laboratory, ANL-95/40 (1995).

50. A. T. Godfrey, "VERA Core Physics Benchmark Progression Problem Specifications Oak Ridge National Laboratory," CASL-U-2012-0131-002, Oak Ridge National Laboratory (2013).

51. A. Yamamoto et al., "Benchmark Problem Suite for Reactor Physics Study of LWR Next Generation Fuels," *J. Nucl. Sci. Techol.* **39** (8), pp. 900 (2002).

52. Y.I. Chang, P. J. Finck, and C. Grandy, “Advanced Burner Test Reactor Preconceptual Design Report,” ANL-ABR-1, Argonne National Laboratory (2006).

53. M. Taube and W. Heer, “Reactor with very low fission product inventory,” EIR-Bericht Nr. 411, Swiss Federal Institute of Reactor Technology (1980).

54. P. E. MacDonald, “NGNP Point Design – Hydraulic Assessments Neutronics and Thermal-Results of the Initial During FY-03,” INEEL/EXT-03-00870, Idaho National Engineering and Environmental Laboratory (2003).

55. H. S. Park, “Resonance Treatment Innovations for Efficiency and Accuracy Enhancement in Direct Whole Core Calculations of Water-Cooled Power Reactors,” Ph.D. Thesis, Nuclear Engineering, Seoul National University (2018).

56. H. Park and W. S. Yang, “Implementation of Particulate Fuel Modeling Capabilities in MC 2-3,” UM/NRDSL-20/03, University of Michigan (2020).

57. X.-5 M. C. Team, “MCNP – A General Monte Carlo N-Particle Transport Code, Version 5, Volume 1: Overview and Theory,” LA-UR-03-1987, Los Alamos National Laboratory (2003).

58. C. Lin, “Design and Analysis of Sodium-cooled Fast Reactor Systems for Nuclear Waste Minimization,” Ph.D. Thesis, School of Nuclear Engineering, Purdue University (2018).

59. T. Park, C. S. Lin, and W. S. Yang, “A moderated target design for minor actinide transmutation in sodium-cooled fast reactor,” *Ann. Nucl. Energy* **98**, pp. 178 (2016); https://doi.org/10.1016/j.anucene.2016.08.003.

60. H. Park and H. G. Joo, “Practical resolution of angle dependency of multigroup resonance cross sections using parametrized spectral superhomogenization factors,” *Nuclear*

Engineering and Technology **49** (6), pp. 1287 (2017); https://doi.org/10.1016/j.net.2017.07.015.

61. W. M. B. Kochunas, B. Collins, T. Downar, "MPACT: Michigan Parallel Advanced Characteristics Transport," *M&C 2013*, Sun Valley, ID, USA, May 5-9 (2013).

62. K. S. Kim, "Procedure to Generate the MPACT Multigroup Library," CASL-X-2015-1013-000, Oak Ridge National Laboratory (2015).

63. Y. S. Jung et al., "Practical numerical reactor employing direct whole core neutron transport and subchannel thermal/hydraulic solvers," *Ann. Nucl. Energy* **62**, pp. 357 (2013); https://doi.org/10.1016/j.anucene.2013.06.031.

64. H. J. Shim et al., "McCARD: Monte Carlo code for advanced reactor design and analysis," *Nucl. Eng. Technol.* **44** (2), pp. 161 (2012).

65. Y. Kim, K. S.; Gentry, C. A.; Clarno, K. T.; Liu, "Simplified AMPX library capability of the CASL neutronics simulator MPACT," *PHYSOR 2018: reactor physics paving the way towards more efficient systems*, Cancun, Mexico, April 22-26 (2018).

66. D. G. Cacuci, *Handbook of Nuclear Engineering*, Vol 2, Springer (2010).

67. K. S. Kim, B. J. Ade, and N. P. Luciano, "Development of the MPACT 69-group Library for MAGNOX Reactor Analysis using CASL VERA," *PHYSOR 2020:International Conference on Physics of Reactors: Transition to a Scalable Nuclear Future*, Cambridge, United Kingdom, March 29 -April 2 (2020); https://doi.org/10.1051/epjconf/202124710016.

68. T. Downar et al., "User Manual for the PARCS v3.0 U.S. NRC Core Neutronics Simulator," UM-NERS-09-0001, University of Michigan (2010).

69. A. Hebert, “Collision probability analysis of the double-heterogeneity problem,” *Nucl. Sci. Eng.* **115** (2), pp. 177 (1993); https://doi.org/10.13182/NSE115-177.

70. Hansol Park et al., “Preliminary Study on TRISO Fuel Cross Section Generation,” ANL/NSE-20/54, Argonne National Laboratory (2020).

71. Q. Zhang et al., “A Comparison Between the Embedded Self-Shielding Method and the Enhanced Neutron Current Method Based on the Equivalent Pin Cell Model on the Irregular Fuel Lattice Problem,” *Nucl. Sci. Eng.* **194** (3), pp. 232 (2020); https://doi.org/10.1080/00295639.2019.1664146.

72. Kang Seog Kim, “Cell Dancoff Based Embedded Self-Shielding Method in Polaris,” *Private communication* (2021).

73. W. K. Terry et al., “Evaluation of the Initial Critical Configuration of the Htr-10 Pebble-Bed Reactor,” NEA/NSC/DOC(2006)1, Idaho National Laboratory (2007).

74. G. Rimpault, “Nuclear Data Needs for Generation IV Nuclear Energy Systems,” *Proc. Int. Workshop*, pp. 18–31, World Scientific Publishing Co. Pte. Ltd.Antwerp, Belgium, April 5-7 (2006); https://doi.org/10.1142/9789812773401_0003.

75. S. Wang, Xinyan ; Liu, Yuxuan ; Martin, William ; Stimpson, “Implementation of 2D/1D Gamma Transport and Gamma Heating Capability in MPACT,” *PHYSOR2020 - International Conference on Physics of Reactors: Transition to a Scalable Nuclear Future, Cambridge*, Cambridge, UK, Mar 29-April 4 (2021).

76. P. Deng et al., “Coupled Neutron and Gamma Heating Calculation Based on VARIANT Transport Solutions,” *Nucl. Sci. Eng.* **193** (12), pp. 1310, Taylor & Francis (2019); https://doi.org/10.1080/00295639.2019.1621617.

77. K. S. Kim, “Generation of the V4.2m5 AMPX and MPACT 51 and 252-Group Libraries with ENDF/B-VII.0 and VII.1,” CASL-U-2016-1177-000, Oak Ridge National Laboratory (2016).

78. R. Sher, “Fission Energy Release for 16 Fissioning Nuclides,” EPRI-NP-1771, Proc Specialist Mtg. on Nucl. Data Evaluation and Procedures (1983).

79. T. England and B. Rider, “Evaluation and Compilation of Fission Product Yields,” LA-UR-94-3106, ENDF-349, Lawrence Livermore National Laboratory (1994).

80. J. M. Hall et al., “Modeling the Production of Beta-Delayed Gamma Rays for the Detection of Special Nuclear Materials,” UCRL-TR-209738, Lawrence Livermore National Laboratory (2005).

81. J. K. Tuli, “Evaluated Nuclear Structure Data File, A Manual for Preparation of Data Sets,” BNL-NCS-51655-01/02, Brookhaven National Laboratory (2001).

82. J. Katakura, “JENDL FP Decay Data File 2011 and Fission Yields Data File 2011” (2012).

83. J. I. Katakura et al., “Estimation of beta- and gamma-ray spectra for JENDL FP decay data file,” *J. Nucl. Sci. Techol.* **38** (7), pp. 470 (2001); https://doi.org/10.1080/18811248.2001.9715056.

84. L. L. Briggs et al., “EBR-II Passive Safety Demonstration Tests Benchmark Analyses – Phase 1,” *Trans. Am. Nucl. Soc.* **111** (February 2014), pp. 1263 (2014).

85. H. Park et al., “Verification and validation tests of gamma library of MC2-3 for coupled neutron and gamma heating calculation,” *Ann. Nucl. Energy* **146**, pp. 107609 (2020); https://doi.org/10.1016/j.anucene.2020.107609.